Phase Change Material Slurry for Medium Temperature Heat Storage

Numerical comparison between a slurry model and a shell and tube packed bed model.

F. Fortman

Technische Universiteit Delft

TU Delft
Delft
University of
Technology

Challenge the future

Phase Change Material Slurry for Medium Temperature Heat Storage

Numerical comparison between a slurry model and a shell and tube packed bed model.

by

F. Fortman

to obtain the degree of Master of Science
at the Delft University of Technology,
to be defended publicly on Tuesday May 29, 2018 at 15.00.

Student number:	4127919	
Project duration:	March 1, 2017 – May 29, 2018	
Thesis committee:	Dr. W. G. Haije,	TU Delft
	Dr. Ir. C. A. Infante Ferreira,	TU Delft
	Prof. Dr. Ir. T. J. H. Vlugt,	TU Delft

Abstract

Concentrated solar technologies have been successfully used to collect solar irradiance and transform it into useful heat for electricity generation. A problem in these systems is often that a mismatch between input and output is present due to variable solar irradiance and energy demand. To compensate for this mismatch storage is utilized to store heat during times when excess heat is present, which is subsequently released when the energy demand exceeds the solar irradiance input. Phase change materials are a novel concept used to store heat by utilizing the energy required for a phase change and can be added to a heat transfer fluid to create a slurry with enhanced heat storage capabilities.

A study has been conducted to identify characteristics of materials that are suitable for heat storage in a phase change material slurry and selected materials accordingly. This has been done for the specific operating temperature range between 200 °C to 300 °C. Using these materials a numerical model of a phase change material slurry has been developed to determine which parameters influence the performance of such a system and to establish a system that shows optimal thermal performance. To check if such a system is a good option for heat storage a comparison is made with a heat storage system where the phase change material is stored in a shell and tube packed bed.

A numerical model has been developed using the apparent heat capacity method to model the phase change. An analysis is performed to find the optimal sizing of the phase change slurry system. With use of a test case, a day with variable solar irradiance input and a fixed energy demand, the transient behaviour of the systems has been tested. A second comparison has been made for scaled up systems to limit the costs of the systems.

$LiNO_3$ has been selected for the phase change material, encapsulated with engraved natural graphite, suspended in MarloTherm A. For the test case 91 643 units, a combination of a collector and heat exchanger to the organic Rankine cycle, are required when these are designed for optimal thermal performance. The total mass of phase change material required equals 6575 kg, including storage. When applying the same sizing to the shell and tube packed bed model it has been found that it can not meet the energy demand at all times throughout the day. Scaling up this system to more practical dimensions results in less units, 145, but the phase change material mass that is required increases to 99 061 kg.

With the parameters from the test case the transient behaviour of both systems has been analyzed. It was found that a smaller mass of phase change material is required for the phase change slurry system due to the possibility to cycle the phase change material faster between solid and liquid phase. Next to that the heat transfer fluid in the shell and tube packed bed system only contains sensible heat. Therefore less energy can be transferred when the heat transfer fluid is at the same temperature as the phase change slurry model.

Contents

List of Figures

List of Tables

Acknowledgments

First of all I would like to thank Dr. ir. C.A. Infante Ferreira from Delft University of Technology for giving me the opportunity to research this topic and his supervision during my Master's thesis. I would also like to thank Dr. ir. R Pecnik from Delft University of Technology for his advice on numerical modeling. Next to that my thanks goes out to Dr. W. G. Haje from Delft University of Technology for his knowledge regarding phase change materials. They steered me into the right direction when needed and was always there to answer my questions.

My gratitude also goes out to my friends, family and girlfriend for giving me support whenever I was stuck and encouraging me. I could not have done this without you.

Delft, Delft University of Technology
May 29 ,2018

Frits Fortman

Nomenclature

List of Abbreviations

BC	boundary condition
CBS	Centraal Bureau voor de Statistiek
CSP	concentrated solar power
CST	concentrated solar technologies
ENG	expanded natural graphite
HEX	heat exchanger
HTF	heat transfer fluid
KNMI	Koninklijk Nederlands Meteorologisch Instituut
LHTES	latent heat thermal energy storage
ORC	organic Rankine cycle
PCM	phase change material
PCS	phase change slurry
PTC	parabolic through collector
PTFE	polytetrafluorethylene
RHS	right hand side
S&T	shell and tube
TDMA	tridiagonal matrix algorithm
TES	thermal energy storage

Roman Symbols

Symbol	**Description**	**Unit**
A	Area	m^2
B	Constant to determine Peclet number	–
Bi	Biot number	–
Fo	Fourier number	–
H	Enthalpy	J/m^3
H_f	Heat of fusion	J/m^3
N	Quantity	–
Nu	Nusselt number	–
Pe	Peclet number	–
Pr	Prandtl number	–
$\dot{Q}$	Heat transfer rate	W
R	Radius	m
Re	Reynolds number	–
S	Dimensionless source term	–
Ste	Stefan number	–
T	Temperature	$^\circ C$
U	Overall heat transfer coefficient	$W/m^{2\circ}C$
V	Volume	m^3
X	Mass fraction	–

Symbol	Description	Unit
Z	Dimensionless axial coordinate	$-$
cp	Specific heat capacity	$J/m^{3\circ}C$
h	Heat transfer coefficient	$W/m^{2\circ}C$
m	Constant to determine Peclet number	$-$
$\dot{m}$	Mass flow	kg/s
n	Time step number	$-$
q	Heat flux	W/m^2
r	Radial coordinate	m
s	Source term	J/m^3s
t	Time	s
u	Flow velocity	m/s
z	Axial coordinate	m

Greek symbols

Symbol	Description	Unit
Γ	Dimensionless thermal conductivity	$-$
Λ	Dimensionless particle thermal conductivity	$-$
α	Thermal diffusivity	m^2/s
α_T	Thermal expansion coefficient	$^\circ C^{-1}$
ΔFo	Dimensionless time step	$-$
ΔT	Phase change temperature range	$^\circ C$
ΔZ	Dimensionless axial distance step	$-$
$\Delta\eta$	Dimensionless radial distance step	$-$
Δt	Time step	s
ϵ	Dimensionless phase change temperature range	$-$
η	Dimensionless radial coordinate	$-$
γ	Surface tension	N/m
λ	Thermal conductivity	$W/m^\circ C$
μ	Dynamic viscosity	Pas
ν	Kinematic viscosity	mm^2/s
Φ	Volumetric concentration	$-$
ρ	Density	kg/m^3
τ	Shear modulus	Pa
θ	Dimensionless temperature	$-$

Subscripts

Symbol	Description	Unit
a	Ambient	$-$
app	Apparent	$-$
c	Crystallization	$-$
e	Effective	$-$
i	Internal	$-$
in	Inlet	$-$
l	Liquid phase	$-$
$mean$	Mean	$-$
m	Melting	$-$

Symbol	**Description**	**Unit**
out	Outlet	–
p	Particle	–
par	Parallel direction	–
$perp$	Perpendicular direction	–
s	Solid phase	–
*	Dimensionless	–
$tube$	Tube	–
w	Wall	–

1

Introduction

In recent years the quest to cut greenhouse gases has lead to an increase in the use of renewable energy sources. Solar energy, one of the earliest sources of energy for humanity is playing a role in reduction of CO_2 emissions with solar thermal power. Concentrated solar power (CSP) is one of the promising and mature options as it has a better ability to dispatch power to match the energy demand than photovoltaic systems [61]. Concentrated solar technologies (CST) exists in five forms: parabolic through collector, enclosed through, parabolic dish collector, concentrating linear Fresnel reflector and solar power tower [23]. To date, Spain (~60%) and the United States (~40%) are the two largest markets for CSP technologies. The world's largest CSP plant was commissioned in the USA in 2014 and is capable of producing 392 MW_e (Ivanpah Dry Lake, CA) [58].

Averaging the total solar irradiance, 3.828×10^{26} W, over the surface of the Earth results in a energy flux density of $1361\,W/m^2$ [31]. CST is based on concentrating this solar irradiation, using mirrors, onto a receiver to heat a heat transfer fluid (HTF) [58] which then carries the heat to a thermal power plant for power generation [61]. To provide optimal performance these mirrors can be programmed to track the path of the sun. This allows the projected area of irradiance collection to be increased and the HTF to be heated by a significant amount.

A problem that often occurs in CSP systems is the occurrence of a mismatch between the the solar irradiance that is available as input and the energy demand at the output of the system. To reduce this mismatch storage is often utilized. The CSP system is designed to have excess solar heat input during peaks, which subsequently is stored to be released at times when the energy demand is larger than the available solar irradiance.

The system that is analyzed in this study consists of a parabolic through collector (PTC) that collects solar radiation to heat a PCS, a combination of a phase change material (PCM) and a HTF. A PCS has the advantage of having a higher energy density compared to a regular HTF. This medium is pumped to a heat exchanger to transfer the collected heat to an organic Rankine cycle (ORC) to generate electricity. A storage vessel might be desirable to enhance the performance of the system, therefore it is included with the option to by-pass it. A schematic overview of the system is found in Figure 1.1.

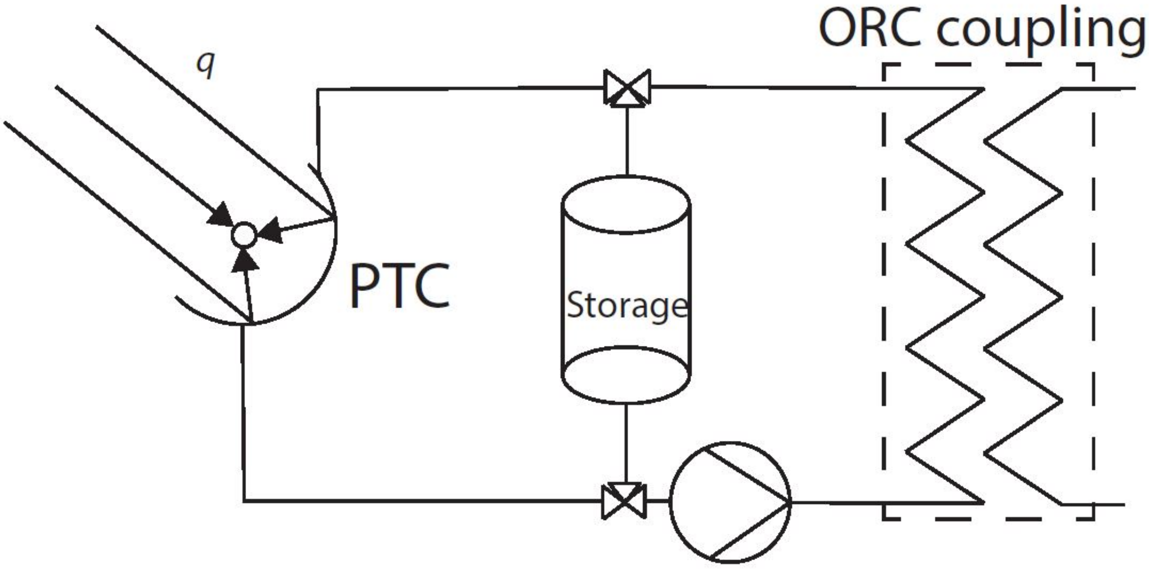

Figure 1.1: Process flow diagram of a PCM suspension system with a parabolic trough PTC coupled to an ORC. Storage is considered as an optional feature.

This system is compared to a system in which the PCM and the HTF are separated. Heat is stored by letting the HTF flow through a shell and tube (S&T) packed bed in which the PCM is stored in the shell. Excess heat that is collected by the HTF in the PTC is stored in the PCM and released once the heat in the HTF is not sufficient to meet the energy demand. An overview of this system is provided in Figure 1.2.

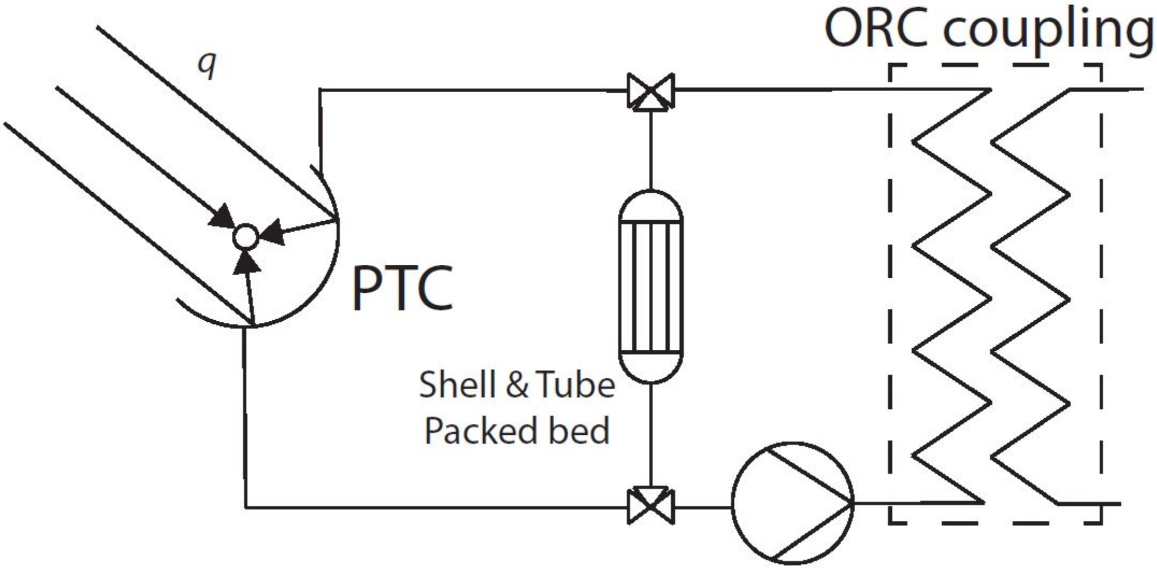

Figure 1.2: Process flow diagram of a shell and tube packed bed storage system with a PTC coupled to an ORC.

The PTC is the most common CST, making up more than 95% of the global CSP installations [61]. Mirrors focus the direct solar radiation on an absorber pipe which is surrounded by an evacuated glass tube with anti-reflective coating on both surfaces [42].

ORCs are a promising technology to convert low grade heat into electricity [55] which makes it ideal to couple them with a PTC. The advantage of an ORC over a steam cycle is that it is able to operate at a lower temperature due to the use of a working fluid with a lower boiling point and lower entropy of vaporization. Next to that, the machinery can be more compact due to a higher fluid density and no water-treatment system or deareator is required. An ORC has however a lower efficiency than a steam cycle and a more costly working fluid [46]. A typical ORC for solar applications consists of an evaporator, a condenser, a turbine and a feed pump.

Because of the discrepancy between the available energy supply from solar thermal and energy demand thermal energy storage (TES) has to be implemented. There are three main techniques for TES: sensible, latent and thermochemical [18]. Sensible heat storage is linked to the rising of temperature without phase change to store heat, thereby increasing the internal energy of storage material. In latent heat thermal energy storage (LHTES) the thermal energy is stored when the material undergoes a phase change. LHTES has a higher storage density than sensible heat storage because the phase-transition enthalpy is usually 50-100 times higher [18]. This process takes place nearly isothermal, around the melting temperature of the transfer medium. The difference in heat stored per temperature increment for sensible heat storage and latent heat storage is found in Figure 1.3. In thermochemical heat storage the energy is stored after a chemical reaction takes place between two substances [18].

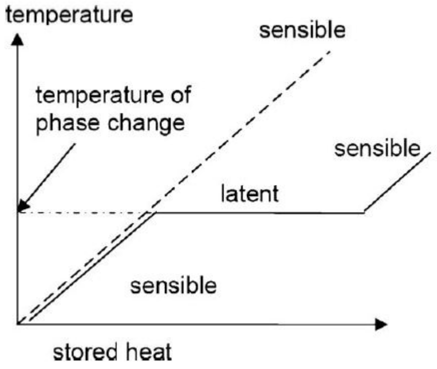

Figure 1.3: Difference in temperature elevation between sensible heat storage and latent heat storage [36].

The large advantage of LHTES is the ability to store a large amount of energy in a relatively small volume [15]. LHTES can be obtained in the following forms: solid-solid, solid-liquid, solid-gas and liquid-gas. In solid-solid phase-transition heat is stored by transforming a solid from one crystalline form to another, the latent heat is low for this kind of phase transition compared to the other phase transitions. Though solid-gas and liquid-gas have a higher latent heat of phase transition than solid-liquid these are unfavourable due to their large volume changes [53]. Therefore the focus of this study is on solid-liquid PCMs.

Current research regarding PCSs is lacking on four topics. The first shortfall lies in the temperature ranges that have been researched. Because the major fields of application of TES in solar applications are present in recovery of waste heat and solar power towers, current research focuses on a melting temperature in the temperature range up to 150 °C or a temperature range higher than 400 °C [20, 38, 59, 61]. Studied LHTES materials and their melting temperatures are present in Figure 1.4, as is seen very few materials with a melting temperature between 200 °C and 300 °C are present in this figure. Next to that no research on PCSs has been performed in this temperature range at all [6].

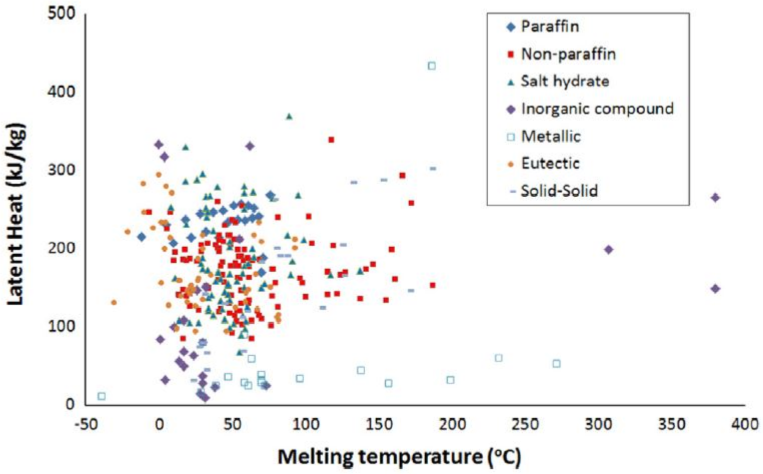

Figure 1.4: Studied latent heat thermal energy storage materials and their corresponding melting temperature and latent heat [54].

Another problem is present in supercooling, also sometimes called subcooling. Supercooling is defined as ”the delay in the start of solidification” and takes place when a PCM transitions from a liquid to a solid phase. Supercooling leads to reduced crystallization temperature and thus the latent heat is released at a lower temperature than the melting temperature [49]. Few research is available on the suppression of supercooling. Next to that little research is known on the influence of supercooling on the performance of PCS for heat storage.

Low thermal conductivity is present in many PCMs. Especially for salts this is a problem, which have a thermal conductivity of around 1 W/m °C. Two concepts that are available to solve this problem are based on the extension of the heat transfer area and on the use of a composite material with high thermal conductivity to increase the overall thermal conductivity of a particle [39]. Research on these topics is however not in an advanced stage.

Convective heat transfer is the last topic that needs to be addressed. The convective heat transfer varies significantly between the solid and liquid heat transfer and in many studies this fact is ignored or dismissed as a minor influence on the heat transfer in a suspension. Evaluation of the convective heat transfer should point out whether this is indeed of minor importance in the studied system.

1.1. Research objective

The main objective of this study is to predict and optimize the transient behavior of a pumpable PCM system which is coupled to an ORC. The numerical model should account for the fluctuating characteristics of production and utilization rates. Further objectives are to indicate PCMs, suitable for this process, with an operating temperature range between 200 °C and 300 °C and to make a comparison between the efficiency of the shell- and tube system investigated by Fan [17] and the designed pumpable PCM system. To be able to make a meaningful comparison a sensitivity analysis regarding the sizing of the pumpable PCS system is to be executed.

1.2. Thesis outline

The thesis has been structured in the following way. Chapter 2 contains the analysis of the selected materials for the system and a literature study regarding thermal and kinetic modeling of the PCS. Chapter 3 contains design choices and elaboration of the working of the numerical model designed to represent the pumpable PCM system. In Chapter 4 the model of Fan is elaborated on and compared to the pumpable PCS system. Chapter 5 provides a comparison of these systems when scaled up to workable dimensions. The conclusion is presented in Chapter 6 and recommendations for further research are found in Chapter 7.

2

Background on phase change slurry modeling

The efficiency of a system for LHTES based on a PCS is dependent on the use of the correct PCM and HTF for the operating temperature range. Therefore care should be put into the selection of materials. This chapter presents background information and recent developments in the research performed on PCMs in Section 2.1. The requirements for the components of the PCS in the studied process are introduced in Section 2.2 and a selection of compatible materials is made in Section 2.3. Thermal and kinetic modeling of PCSs is discussed in Section 2.4. Previous research that has been performed regarding solid-liquid interfaces and phase change modeling, as present in the PCM particles, is discussed in Section 2.5 and a conclusion is provided in Section 2.6.

2.1. Background on phase change material slurries

PCMs are classified in three categories: organic, inorganic and eutectic [61]. A more extensive classification of latent heat storage materials, including their melting temperature and latent heat, is found in Figure 2.1.

Organic PCMs are split between paraffins and non-paraffins (fatty acids, alcohols and glycols). Organic PCMs have a stable phase change temperature without segregation, no supercooling and are usually not corrosive. These materials have a wide range of latent heat of fusion but a low melting temperature (<100 °C) and low density [54].

In general, inorganic PCMs have double the heat storage capacity per unit volume as compared with organic materials. Next to that inorganic materials have a higher thermal conductivity and a higher melting temperature than organic PCMs. A negative effect of inorganic PCMs is the presence of phase segregation and supercooling, which have a negative impact on the energy storage capacity. Metals and alloys are also considered in this group but are generally not considered for use in LHTES due to their low heat of fusion per unit mass [39].

An eutectic mixture means a combination of two or more substances having a minimum-melting composition [39]. Eutectics show no segregation during melting and crystallization due to their sharp melting point, resulting in a very small phase change temperature range. Eutectics can be composed of either organic or inorganic materials.

A temperature operating range of 200 to 300 °C requires an inorganic material and therefore the focus of the other literature deals with inorganic materials only.

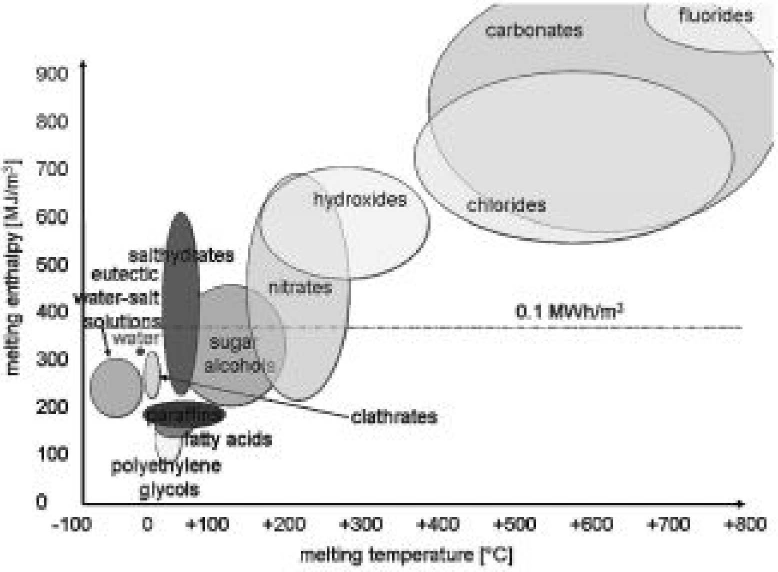

Figure 2.1: Break down of the classification of solid-liquid phase change materials and their respective melting temperatures and latent heat [36].

2.1.1. Encapsulation

Encapsulation of PCMs is present in two forms, core-shell and shape-stabilized, depending on the shape of the capsule. Core-shell encapsulation is the term for covering a material (core) with another material (shell), while shape-stabilized encapsulation are composites of PCMs with other materials that retain molten PCMs by capillarity [38].

Encapsulation acts as a protection against the environment and as a heat transfer surface [39]. Encapsulation comes in two sizes: macroencapsulation and microencapsulation. Macroencapsulation is implemented by putting the PCM in a container of magnitude centimeters and larger and is applicable to storage vessels.

Microencapsulation of PCMs comes in an order of magnitude of 2 µm to 2000 µm. It is useful in reducing supercooling as it reduces the reactivity of the PCM to the outside environment. On the other hand supercooling can be enhanced most likely due to the absense of nuclei. The degree of supercooling becomes worse as the size of the particles decreases [49]. Due to the small size of the PCM particles when stored in a HTF to form a PCS it can be treated as a homogenous fluid that can be used as both a thermal storage material and a HTF [9]. Furthermore, as it is possible to pump the slurry, the same medium can be used to both transport and to store energy, reducing the irreversibility of the system [52].

Not all encapsulation methods are suitable for use on inorganic materials, mainly because of solubility and stability issues. A summary of encapsulation methodologies that have been proven to be succesful on inorganic materials include [38]:

- **Emulsion polymerization** - PCMs are dissolved in the minor medium and a polymer or monomers are added to create the shell to emulsify the material. Polymerization is applied by either: monomers propagation by addition of a free radical entering the monomer-swollen emulsifier micelle, precipitation of the free radical chain length or the free radical growing in the medium induces propagation after entering the monomer droplets.
- **In situ polymerization** - Formation of the capsules occurs in micelles formed in an oil-water system, formation of PCMs emulsion in water is required after which pre-polymers are added into the continuously agitated emulsion to encapsulate the PCM and finally

the encapsulated PCM is washed and dried.

- **Interfacial polymerization** - Solvent evaporation-precipitation is used for the encapsulation of inorganic materials and consists of four steps. The active substance is dispersed in an organic solvent containing the polymeric wall. This phase is then emulsified in an immiscible non-solvent polymer continuous phase. Polymer coating around the active substance particles occurs as a result of portioning of the polymer solvent from the dispersed phase to the continuous phase, accompanied by solvent evaporation. In the last step the solid particles are recovered after washing, filtration and drying.
- **Electroplating** - The PCM is first washed in order to remove the oxide film and is then loaded in electroplating equipment to electrodeposit. After electroplating the PCM is washed again and put in barrel-plating equipment. After washing with water and drying the encapsulated PCM is obtained.
- **Sol-gel process** - Encapsulation is obtained by an oxide association of a molecular predecessor in a solution. A polymer is coated and cured into the PCM pellets, becoming insoluble in water and in several organic solvents. The pellets are then saturated in a solution to turn the PCM hydrophobic.
- **Mechanical packaging** - Encapsulation is obtained by pressing the PCM in the shape of a pellet and packing it into a prefabricated capsule.

2.1.2. Supercooling

Supercooling is a phenomenom mostly present in inorganic PCMs that leads to a lower crystallization temperature than the melting temperature of a material thus the latent heat will be released at a lower temperature as seen in Figure 2.2. Factors that influence the degree of supercooling include [49]:

- Heterogeneous nucleation
- Homogeneous nucleation
- Rate of cooling
- Container surface roughness

To lower the degree of supercooling a nucleation agent can be added. This has however a negative effect on the latent heat of the PCM and therefore a trade off between the different degrees of supercooling has to be made to justify adding a nucleating agent. Nucleating agents are solid particles or crystals in structure or lattice parameters, which initiate crystallization but do not dissolve at operational temperature [49].

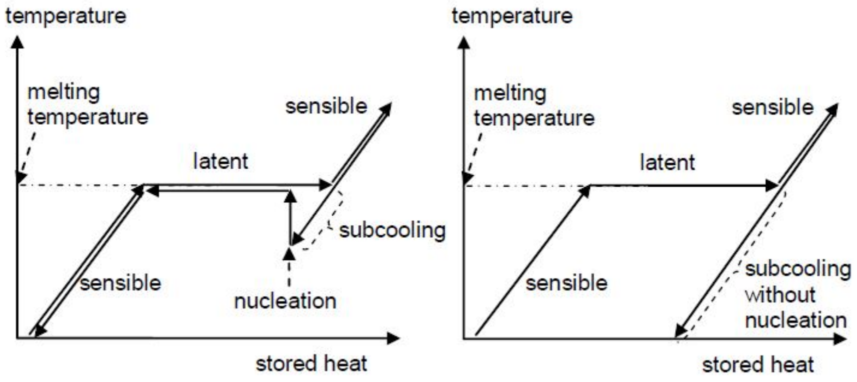

Figure 2.2: Influence of supercooling in phase change materials on the ability to store heat [36].

2.1.3. Stability of phase change slurries

Stability in PCS is an issue as the PCM particles interact with each other not only on a microscopic scale but also on a macroscopic scale. Problems like sedimentation, creaming and agglomeration occur. These occurences lead to a non-uniform distribution of the PCM particles resulting in a non-homogeneous fluid. The main problem for microencapsulated PCM however is rupture due to stresses exerted by the system and therefore the strength of the capsulation material is an important property [9].

2.2. Requirements of materials

A PCS consists of a maximum of three components, a PCM, a capsule and a HTF. A capsule is optionally introduced to a PCS if it is beneficial to the properties of the total system. Each component has a function within the PCS and should be carefully selected such that it fulfills its function to its best capability. Next to that a component should not negatively affect another component.

The requirements for the PCM are most elaborate as the performance of the PCS is largely dependent on this component. A suitable PCM has favourable properties regarding chemical, kinetic, physical and thermal behaviour. Based on the requirements specified in Table 2.1 PCMs have been selected for this study. Economical, environmental and technological requirements for PCMs are important but have been omitted from this study since these lie outside of the scope of the study.

Table 2.1: Main requirements for the selection of suitable phase change material in systems focused on high temperature LHTES [20]. In brackets is the property noted that can be used to quantify a requirement.

Requirements		**Reasons**
Chemical	Long-term chemical stability	Keeping the initial thermochemical properties along the cycling periods
	No chemical decomposition	
	Compatibility with container materials and low reactivity to HTFs	Ensuring long lifetime of the container and the surrounding materials in case of leakage
	No fire and explosion hazard	Ensuring workplace safety
	No toxicity	Ensuring handling safety
	No phase separation/ Incongruent melting	Avoid changes on stoichiometric composition of melt
Kinetic	Little or no subcooling [T_m-T_c]	Having the same melting/solidification temperature and avoiding heat release problems
	Sufficient crystallization rate	Meeting the recovery system heat transfer demands
Physical	High density [ρ_s]	Minimizing the volume occupied by the LHTES material
	Low vapour pressure/ Low density variation [ρ_l/ρ_s]	Diminishing the mechanical and chemical stability requirements of the container or vessel
	Favourable phase equilibrium	Possibility of using eutectic mixtures
Thermal	High specific heat [cp_s,cp_l]	Providing significant sensible heat storage
	High thermal conductivity in both solid and liquid states [λ_s,λ_l]	Enhancing the heat transfer within the LHTES material by providing minimal temperature gradients
	Melting/solidification temperature in the desired operating temperature range [T_m]	Ensuring the success of the charging and discharging processes within the operation conditions
	High latent heat of transition per unit volume near temperature of use [H_f/V]	Providing significant latent heat storage in small volumes
	Congruent melting	Ensuring the complete melting of the LHTES material and their homogeneity

The HTF should remain in a liquid phase when the system is not in operating mode to avoid clogging at atmospheric conditions. It should also show thermal stability at the upper range of the operating temperature, a large working temperature range is thus required. Favorable thermal and kinetic behaviour is desirable: a high thermal conductivity is desired to enhance the heat transfer coefficient and a low viscosity is preferable to get a low pressure drop. A large specific heat capacity allows for a better heat storage in the HTF. Low working pressure is desirable to keep stress on the containers to a minimum. Last but not least, safety and corrosion aspects are important [2].

Encapsulation of the PCM is an option to improve the thermal or kinetic behaviour of the PCS and to prevent a reaction between the PCM and the HTF. The material used for encapsulation should have high thermal conductivity and a low permeability to obtain good thermal and kinetic behaviour. Next to this the material should sustain thermal reliability and chemical stability throughout the operational period. This requires the capsule to withstand the stresses of operation, to be non-flammable and to show no reactance with either the PCM or the HTF [21]. Viscosity of the encapsulation material is not an issue as it has been proven that the encapsulation material has no influence on the viscosity of the system [63].

2.3. Selection of material for phase change slurry

Table 2.2 presents ten materials, and their properties applicable to LHTES, that can be used in the operating range between 200 °C and 300 °C . More materials than the limited number presented in Table 2.2 are applicable to use in a LHTES system at this operating temperature range [30] but have been deemed either comparable or worse options than the materials present. For the chosen materials the relevant thermophysical properties have been obtained to allow for an assessment of the capabilities of a material to fulfill the requirements presented in Section 2.2.

Table 2.2: Phase change materials with a melting temperature in the range of 200 to 300 °C suited for the discussed LHTES system. The thermophysical properties of a material are given at the melting point of the material.

Material	T_m [°C]	H_f [kJ/kg]	ρ_s [kg/m^3]	ρ_l [kg/m^3]	cp_s [kJ/kg°C]	cp_l [kJ/kg°C]	λ_s [W/m°C]	λ_l [W/m°C]	μ [mPas]
$NaNO_3/KNO_3$ (50/50) [28]	222	100	2044	1950	1.42	1.46-1.53	-	0.46-0.51	4.48
Sn [8, 19]	232	60.5	-	-	0.257	0.268	46.1	32.6	
$NaNO_3/NaNO_2$ (50/50)[28]	235	-	2067	1879	-	-	-	-	-
$LiNO_3$ [28]	254	360	2163	1780	1.78	1.62-2.03	1.37	0.58-0.61	5.76
$LiCl/LiOH$ [3] (37/63)	262	485	1550	-	2.4	-	1.18	0.70	-
$NaNO_2$ [29]	270	180	2027	1810	-	1.65-1.77	0.67-1.25	0.53-0.67	3.10
Bi [8, 19]	271	53.3	-	1007	0.285	0.304	-	-	-
$ZnCl_2$ [44]	280	75	2907	-	-	0.74	0.5	-	-
$NaOH/NaCO_3$ (92.8/7.2) [29]	283	-	2126	1860	-	-	-	-	3.50
Na_2S_4 [28]	294	-	-	1912	-	-	-	-	48.02

The PCMs with a known heat of fusion that have been discussed in Table 2.2 have been indicated in Figure 1.4 as provided in Figure 2.3. It is seen that tin and bismuth correlate with the two data points for metallic PCM that lie within the operating temperature range. The other materials have not been used previously in experimental studies as they do not appear to match a data point in the plot.

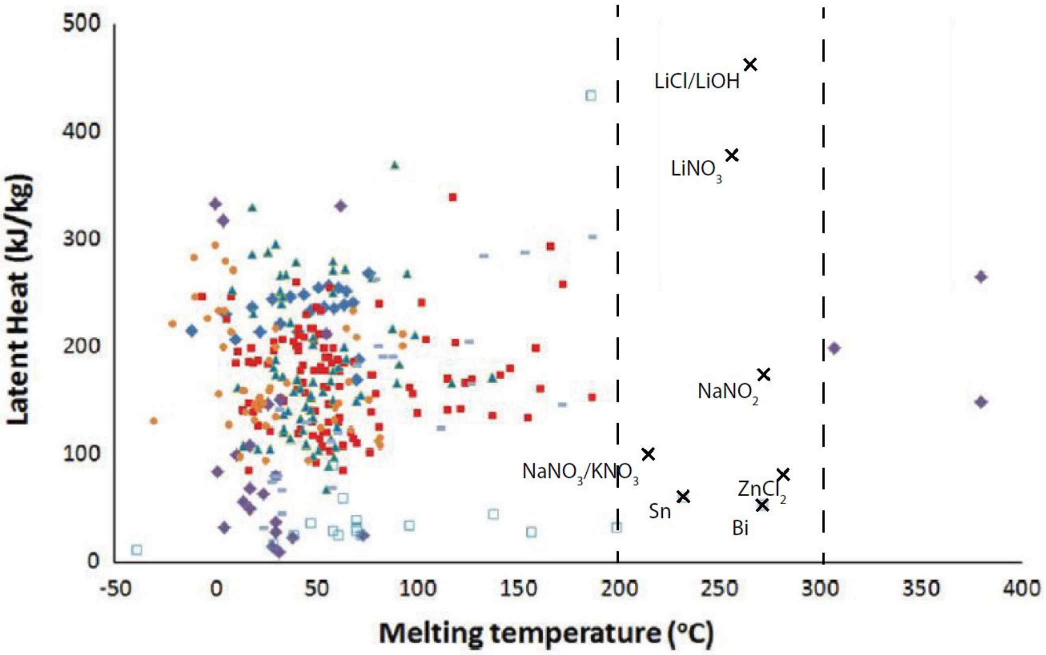

Figure 2.3: Studied latent heat thermal energy storage materials and their corresponding melting temperature and latent heat. The materials that have been discussed in Table 2.2 have been added.

As stated before, limited data is available regarding materials with a melting point in the operating temperature range. Several materials with a suitable melting point have been identified but not all properties have been found for the operating range and are therefore excluded. While LiCl/LiOH has a promising heat of fusion, volume changes far exceeding 20 percent have been reported [3]. Large volume changes are also present in the metals, Sn and Bi, and are therefore not considered. Sulfides have not been examined as these materials have a similar high viscosity as Na_2S_4 presented in Table 2.2.

Most promising are $NaNO_3/KNO_3$, $NaNO_2$ and $LiNO_3$. $NaNO_2$ has however a small temperature range in which it is liquid, with a boiling point at 320 °C, resulting in a large variation in specific heat and thermal conductivity in the operating temperature range. Therefore $NaNO_2$ has not been considered. Although $LiNO_3$ has a large volume change of 21.5% the alternatives show similar changes of volume while the heat of fusion is superior to its alternatives. Furthermore it has the advantages of being non-flammable and nontoxic and having chemical stability and no phase segregation [32]. For these reasons it has been selected for implementation. The supercooling range has been taken to be 2.5 °C as the range of melting temperatures is reported to lie between 252 and 254.5 °C as reported by four separate studies [35].

The thermophysical properties of commercial HTFs, which are in liquid phase from atmospheric conditions up till the upper limit of the operating temperature range, from five different companies have been obtained for comparison. These HTFs have all been demonstrated to work with CST and are therefore good candidates. Their properties have been obtained in the median of the operating temperature range to be able to make a comparison. The properties of these HTFs are publicly available and are presented in Table 2.3.

Table 2.3: Selection of heat transfer fluids that are applicable to the studied system. The properties of the heat transfer fluids have been analyzed at 250 °C, the median of the operating temperature range.

Heat transfer fluid	**Temperature range** $[^{\circ}C]$	ρ_l $[kg/m^3]$	λ_l $[W/m^{\circ}C]$	cp_l $[kJ/kg^{\circ}C]$	μ $[mPas]$
DowTherm Q	-35 - 330	792	0.0889	2.356	0.23
MarloTherm SH	-5 - 350	880	0.1005	2.405	0.50
ParaTherm HR	-10 - 370	785	0.0988	2.5	0.43
Therminol 66	-32 - 345	848	0.100	2.379	0.57
XceTherm XTE	-57 - 329	738	0.1193	2.201	0.46

The Dowtherm Q and XceTherm XTE HTFs have an operating range that exceeds the operating conditions of the system by 29-30 °C which may lead to problems when no circulation is present in the system and the HTF in the PTC can become very hot. Therminol 66 has a lower heat capacity and thermal conductivity and a higher viscosity than MarloTherm SH so this HTF is not the best option. ParaTherm HR and MarloTherm SH do not differentiate much from each other, whereas MarloTherm SH has better thermal properties ParaTherm HR has a lower viscosity. At this stage of the study it is not possible to identify whether thermal or kinetic behavior will be the bottleneck in the system and a decision based hereupon is not possible. MarloTherm SH has been selected for this study as a previous study has proven that it is compatible with all possible encapsulation materials [50]. The thermophysical properties of MarloTherm SH are present in Table A.1.

Materials that have been used multiple times in encapsulation of inorganic materials in previous studies include expanded natural graphite (ENG), polytetrafluorethylene (PTFE), better known as Teflon, and $\mathrm{SiO_2}$ xerogel [38]. The properties of these materials have been obtained and are presented in Table 2.4. The density and thermal conductivity of PTFE have been extrapolated from the available data to find values for 250 °C. The properties of SiO_2 have only been found at 45 °C and these properties have therefore been provided.

Table 2.4: Selection of encapsulation materials that are applicable to the studied system. The properties of the materials have been analyzed at 250 °C, the median of the operating temperature range.

Material	ρ_s $[kg/m^3]$	λ_s $[W/m^{\circ}C]$	cp_s $[kJ/kg^{\circ}C]$	τ $[MPa]$
ENG [60]	831	337	1.0	140
PTFE[4, 12]	1960	0.31	1.5	<2.7
SiO_2 [14]	420	47	1.0	-

PTFE has not been considered for encapsulation as the melting point is as low as 327 °C [4]. When no circulation is present the capsules can melt due to no transfer of heat and mixture of the HTF and the PCM can occur. The thermal properties of ENG are better than the properties of $\mathrm{SiO_2}$ and therefore ENG has been selected for possible encapsulation. A shape-stabilized encapsulation is required with this material [60]. Figure 2.4 pictures an exaggerated version of the function of a shape-stabilized encapsulation during the density change between phases.

(a) PCM in solid phase in the shape-stabilized encapsulation.

(b) PCM in liquid phase in the shape-stabilized encapsulation.

Figure 2.4: An exaggerated depiction that explains how the shape-stabilized encapsulation acts as a buffer for the expansion of the PCM when it melts. The volume of the PCM increases but the size of the particle remains constant.

Although encapsulation is not required to prevent mixing or a chemical reaction between the PCM and the HTF it is employed to increase the heat transfer properties of the PCM. To allow for even better thermal conductivity the ENG has been treated with sulfuric acid, which increases the thermal conductivity of ENG [60].

2.4. Modeling of thermal and kinetic behavior of slurry

As the individual materials have been selected for the composition of the slurry the thermal properties of this PCS are to be determined. Mesoscopic multi-phase fluid flows can be analyzed using the Lattice-Boltzmann method, while macroscopic multi-phase flows can be analyzed using Eulerian or Lagrangian methods. As stated in [47], a slurry can be considered homogeneous when the PCM particles are manufactured in a range of 0.3 to 400 µm, putting it in the microscopic scale.

2.4.1. Unification to a homogeneous fluid

Using the stated assumptions the properties of the PCS have been calculated. The density of the PCS is given by the sum of the products of the mass fraction X and the density ρ of each component as described in Equation (2.1). No relation between temperature and density has been found but the linear thermal expansion coefficients of graphite have been applied to account for the change in density due to temperature variation. The mass of the ENG is kept constant while the volume of the sphere varies by temperature. The thermal expansion coefficients differ parallel and perpendicular to the fibers and therefore the average thermal expansion coefficient has been taken to model the volume change. The difference between the parallel and perpendicular radii is 0.04 % at the maximum operating temperature of the HTF and therefore treating the particles as spherical is justified.

$$\rho_{PCS} = \frac{1}{\sum \frac{X_i}{\rho_i}} \tag{2.1}$$

In a similar way the specific heat capacity is calculated by multiplying the specific heat capacity of the PCM, HTF and the capsule by their respective mass fraction X as depicted by Equation (2.2).

$$cp_{PCS} = \sum X_i cp_i \tag{2.2}$$

Maxwell's relation given in Equation (2.4) is used to describe dispersed particles in a homogeneous matrix for micro scale fluidics. This relation has been established usign a network of thermal resistances in a PCS containing encapsulated microparticles. This relation is valid up to a particle volume concentration fraction of 0.25 [48]. The thermal conductivity for a particle has been determined first and is given in Equation (2.3) [14]. The thermal conductivity of the PCS is largely dependent on the volume fraction of the particles.

$$\lambda_p = \lambda_{capsule} \frac{\lambda_{PCM} + 2\lambda_{capsule} - 2\Phi_{PCM}(\lambda_{capsule} - \lambda_{PCM})}{\lambda_{PCM} + 2\lambda_{capsule} + \Phi_{PCM}(\lambda_{capsule} - \lambda_{PCM})} \tag{2.3}$$

$$\lambda_{PCS} = \lambda_{HTF} \frac{2 + \frac{\lambda_p}{\lambda_{HTF}} + 2\Phi_p(\frac{\lambda_p}{\lambda_{HTF}} - 1)}{2 + \frac{\lambda_p}{\lambda_{HTF}} - \Phi_p(\frac{\lambda_p}{\lambda_{HTF}} - 1)} \tag{2.4}$$

The thermal conductivity of the capsule is dependent on the orientation of the heat transfer as the thermal conductivity of ENG depends on the direction of the fibers. Whereas the thermal conductivity of ENG is promising in the direction of the fibers, the thermal conductivity perpendicular to the fibers is up to a factor ten lower. To account for this occurrence the average thermal conductivity of the ENG has been used for the capsule to be able to model the particle as isotropic. It has been assumed that the orientation of the fibers is evenly distributed in a particle, therefore the average thermal conductivity of the encapsulation material has been determined by taking the average thermal conductivity of the parallel and perpendicular fibers.

Starting from Einstein's calculation for the viscosity of dilute suspension of spheres given in Equation (2.5) a relation has been obtained that can be used to calculate the viscosity of fluids with a larger volume concentration of particles. To come to this relation the fluid has been described as hard, impenetrable spheres that cannot overlap in space, in a colloidal suspension, a substance made up of a system of particles with linear dimensions in the range of 10^{-7} to 10^{-5} m dispersed in a continuous medium. A relation for the specific case mentioned has been found and is given in Equation (2.6) [37]. The effect of the concentration on the dynamic viscosity of a PCS is presented in Figure 2.5. It is seen that the dynamic viscosity increases with an increase in volumetric particle concentration, almost double at a volumetric particle concentration of 0.25 compared to regular HTFs.

$$\mu_{PCS} = \mu_{HTF}(1 + 2.5\Phi_p) \tag{2.5}$$

$$\mu_{PCS} = \mu_{HTF}(1 + 2.5\Phi_p + 5.00\Phi_p^2) \tag{2.6}$$

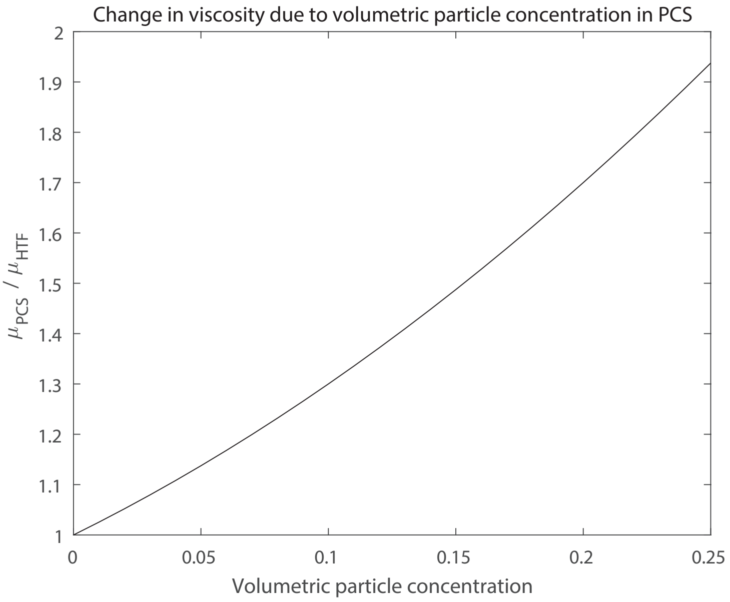

Figure 2.5: The effect of the volumetric particle concentration on the dynamic viscosity of a PCS.

Using the stated equations thermophysical properties of the homogeneous fluid with the selected materials have been determined at six different volumetric particle concentrations and are tabulated in Table 2.5. A particle is assumed to consist of 70vol% PCM with the remaining part being encapsulation material. Increasing the volumetric particle concentration leads to an increase in density, thermal conductivity and viscosity, while leading to a lower specific heat capacity. Due to the increase in density when the volumetric particle concentration increases the volumetric specific heat capacity declines even more. The capacity to store sensible heat decreases but is compensated by the ability to store latent heat by addition of the PCM particles. The thermal conductivity increases, doubling almost for a volumetric concentration of 0.25, resulting in better conduction in the PCS. The viscosity also almost doubles in value but the effect to the kinetic behaviour of the PCS due to this increase is negligible.

Table 2.5: Thermophysical properties of the homogeneous fluid at 254.5 °C at six volumetric particle concentrations. A PCM particle consists of 70 vol% PCM and 30 vol% encapsulation.

Parameter	**Unit**	**HTF**	**PCS** Φ_p**=0.05**	**PCS** Φ_p**=0.10**	**PCS** Φ_p**=0.15**	**PCS** Φ_p**=0.20**	**PCS** Φ_p**=0.25**
ρ	$[kg/m^3]$	876.5	943	1003	1060	1111.8	1160
cp	$[J/kg°C]$	2423	2359	2300	2246	2195	2148
λ	$[W/m°C]$	0.010	0.115	0.133	0.152	0.174	0.198
μ	$[mPas]$	0.89	1.01	1.16	1.32	1.51	1.72

2.4.2. Mesh

Three types of mesh grids that are commonly used to analyze three-dimensional flow of slurries have been identified in the literature study. The first mesh grid that has been identified among studies is a near wall-mesh as depicted in Figure 2.6 [41]. It incorporates a decrease in grid interval size near the wall of the circular pipe to allow for a more accurate solution at the wall of the pipe, where melting occurs first, while containing a square grid at the center of the pipe as a less accurate solution is required there. As the velocity of a fully developed fluid flow in a circular pipe is lower at the wall than at the center it is expected that the interaction between particles is larger close to the wall and it can be opted to use a near-wall mesh if these interactions are of significant importance.

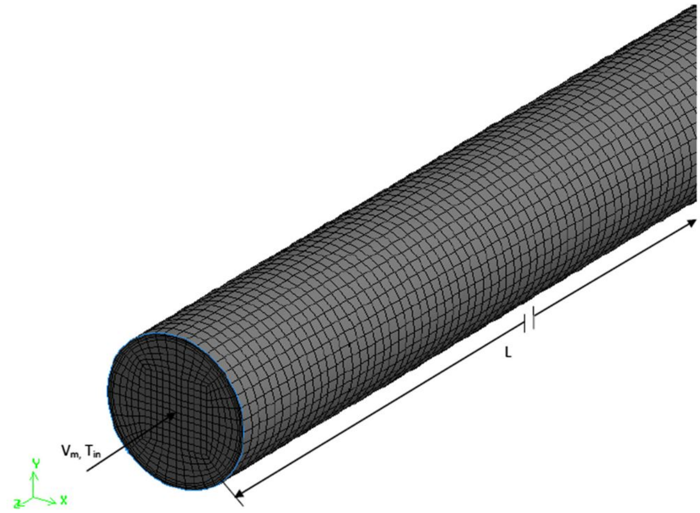

Figure 2.6: Schematical design of a near wall mesh grid [41].

A second mesh grid that is commonly used in computation fluid modeling is the hexahedral based mesh, commonly found in computational fluid dynamics software like Ansys Fluent [34]. Comparable to a tetrahedral mesh grid this mesh grid follows the fluid flow in axial direction. Next to that this grid is less error-prone compared to tetrahedral or axisymmetric mesh grids due to the angle between the cells. A disadvantage of implementing a hexahedral mesh grid is that the problem could become unnecessary complex to solve compared to a axisymmetric grid and using meshing software is advised.

To allow for an equal number of particles per control volume each control volume has to comprise of equal volume. This is achieved by using equal area intervals in the radial direction [57]. The spatial interval in radial direction is defined in Equation (2.7), where R_{HEX} is the radius of the circular pipe, r_i is the radial coordinate of the spatial interval i and N is the number of spatial intervals in radial direction. A difficulty arises using this mesh as the spatial interval in radial direction varies. This grid is divided equally in axial direction, making it the least complicated of the three.

$$r_i = R_{HEX}\sqrt{\frac{i}{N}} \tag{2.7}$$

2.5. Modeling phase change material behavior

To be able to make a numerical analysis of a PCM particle in a PCS the phase change has to be modeled. Several methods to solve solidification and melting of solid-liquid problems have been investigated. Previous research regarding the numerical analysis of microscopic multi-phase phase change suspensions has been considered and is briefly presented in this section. For a more detailed description of a specific method it is advised to read the referenced material.

2.5.1. Analytical methods

Analytical methods are used to get an approximation of simplified problems and are expanded upon when using a numerical model. Using an analytical approach can be beneficial to gain insight in the behaviour of a system.

Neumanns method

The most simple phase change problem is the one-phase problem first solved by Stefan. This problem dictates that one phase varies in temperature while the other phase remains at melting temperature. It has been discovered that the rate of melting or solidifying in a semi-finite region is governed by the dimensionless Stefan number, presented in Equation (2.8). Neumann extended this to a two-phase problem, by stating that the initial temperature is not that of the phase change temperature and is not kept constant [56]. Neumanns method is only available for moving boundary problems in a rectangular coordinate system. Paterson has extended this solution to a cylindrical coordinate system [43].

$$Ste = \frac{cp(T - T_m)}{H_f} \tag{2.8}$$

Heat balance integral method

Exact analytical solutions can not be used for problems in which a constant heat flux is present. An approximate solution has to be found for these type of problems. These problems can be solved analytically by assuming a temperature distribution depending on the spatial variable in a particular form which is consistent with the boundary conditions. This temperature distribution is then integrated with respect to the spatial variable over the indicated interval to obtain the heat balance integral. To obtain the solution the obtained integral equation has to be solved to obtain the time dependence of the temperature distribution and boundaries.

2.5.2. Numerical analysis

Numerically analyzing solidification and melting is possible using either the strong or the weak method. The strong numerical solution is based on moving boundaries to ensure that a finite difference encompasses a material in a single state whereas the weak numerical solution has a fixed boundary and approaches a single state averaging the properties of the material in a finite difference to approximate a single state.

Fixed grid method

Using finite difference techniques the heat flow equation is replaced by finite difference approximations in order to compute the temperature at a point in a fixed grid in the (x,t) plane. At any time the phase change boundary will usually be located in between two neighboring grid points. Various finite difference schemes have been proposed to approximate the partial differential equation and the boundary conditions at the neighboring grid points. Murray introduces two fictitious temperatures at the neighboring grid points, one obtained by quadratic extrapolation from temperatures in the solid region while the other is extrapolated from temperatures in the liquid region [40]. Together with the melting temperature and the location of the boundary these are used to calculate the temperature near the interface.

Lazaridis built on this technique, he used explicit finite difference approximation on a fixed grid to solve two-phase problems in both two and three spatial dimensions. He based developed numerical schemes on a characteristic set of differential equations, which state that the moving boundary layer is an isotherm. Close to this boundary equations for unequal intervals have been imposed into the characteristic equations to account for the moving boundary [33].

The major advantage of fixed grid methods is that these methods can solve multidimensional problems efficiently. The numerical approach for the moving boundary layer can be achieved without much modification of existing heat transfer codes. Therefore fixed grid methods are commonly used for modeling a variety of complex moving boundary layers.

Variable grid method

Fixed grid methods sometimes fall short when the boundary moves a distance larger than the specified finite difference in a time step. This requires an extended array to make up for this constraint, which increases the number of computations that have to be performed. This can be avoided by implementing a variable grid method, where the exact location of the boundary is evaluated on a grid every time step. Variable grid methods can be subdivided in variable time step methods and variable space methods.

In variable time step methods a variable time step is implemented such that the moving boundary always coincides with a grid point on a fixed grid, as introduced by Douglas [11]. At each time step the time step is chosen such that the distance that the boundary layer moves is exactly the finite difference used for the chosen fixed grid. Gupta and Kumar used the same set of finite difference equations but they used the interface condition to update the time step, avoiding instability as the depth of the moving boundary increases [25].
For variable space methods the number of spatial intervals is kept constant while the spatial intervals are adjusted so that the moving boundary is located on a grid point.

Enthalpy formulation method

Both the fixed grid method and variable grid method discussed previously are strong numerical solutions. While these methods provide an accurate solution to multi-phase problems it is difficult to obtain a solution in a problem with fluid flow due to a large required processing capacity. To allow for analysis of a three-dimensional multi-phase fluid flow a weak method is required to allow for efficient allocation of processing capacity. In these methods the moving boundary is avoided.

The apparent heat capacity method is a method in which the latent heat is introduced by increasing the heat capacity of the PCM and was first introduced by Hashemi and Sliepcevich [27]. When the latent heat is released uniformly in the phase change temperature range the apparent heat capacity can be described as Equation (2.9), where T is the temperature of the material, T_m is the melting temperature, ΔT is the phase change temperature range, H_f is the latent heat, $T_s = T_m$ - ΔT is the solid phase temperature and T_l is the liquid phase temperature.

$$cp_{app}(T) = \begin{cases} cp_s & \text{if } T < T_s \\ \dfrac{\int_{T_s}^{T_l} cp(T)dT + H_f}{\Delta T} & \text{if } T_s < T < T_l \\ cp_l & \text{if } T > T_l \end{cases} \tag{2.9}$$

Defining the latent heat in this way allows for easy discretization and a numerical solution. The temperature of the material is taken at the grid points. Difficulties arise when the temperature rises from beneath the solid temperature to above the liquid temperature in a single time step. This results in not taking into account the latent heat in that time step. To avoid this constraint small time steps have to be taken, consequential increasing the computational time.

An improvement to this method, proposed by Poirier and Salcudean, is the effective capacity method. With this method a temperature profile between grid points is composed. The apparent heat capacity is then used to calculate the effective specific heat capacity per Equation (2.10), where V indicates the control volume. A drawback to this method is that it is not efficient when temperature gradients are steep [45].

$$cp_e = \frac{\int cp_{app} dV}{V} \tag{2.10}$$

The heat integration method is another weak numerical method, introduced by Dusinberre, to analyze melting. If the temperature in a control volume exceeds the melting temperature it is assumed that the material in the control volume undergoes a phase change. The temperature in the control volume is reset to the melting temperature and the enthalpy that is removed due to this setback is stored for the control volume. Only when the total amount of stored enthalpy in the control volume is equal to the latent heat of the material the temperature of the control volume is allowed to exceed the melting temperature [13]. This method is easily applicable for multidimensional problems, but requires monitoring of the time step to acquire an accurate solution.

Source based methods introduce a source term which allows additional heat from melting or solidification to be introduced in the general form of the equation. Sensible heat and latent heat are separated in the general heat transfer equation by introducing this source term.

When the latent heat is accounted for in the enthalpy by a relationship between enthalpy and temperature as given in Equation (2.11) an enthalpy method is described, introduced by Eyres et al. The enthalpy in a control volume is indicated based on the temperature in the control volume [16]. Enthalpy, H, is defined as presented in Equation (2.12) for an isothermal phase change. An advantage of this method is that this method is independent of the time step size and phase change temperature range. This method however is also known to display oscillations at a grid point.

$$\rho \frac{\partial H}{\partial t} = \frac{\partial}{\partial z}\left(\lambda \frac{\partial T}{\partial z}\right) \tag{2.11}$$

$$H(T) = \begin{cases} cp_s T & \text{if } T \leq T_m \\ cp_l T + H_f & \text{if } T > T_m \end{cases} \tag{2.12}$$

2.6. Conclusion

Previous studies on PCSs have found that supercooling of PCM materials and the stability of particles in a HTF represent the largest problems in constructing a PCS. These issues have been addressed and the materials that compose the PCS have been chosen such that these problems are minimal.

Requirements that a PCM must fulfill to ensure a good performance include having a high specific heat, low density variation, few supercooling, a high melting rate and being safe in combination with the other materials present in the system. A focus has been put on inorganic PCMs as these have a melting temperature that lies within the operating temperature range between 200 °C to 300 °C. From the identified candidates for the PCM $LiNO_3$ has been selected due to its large heat of fusion.

The choice of HTF is not crucial to the performance of the PCS as many HTFs have similar thermophysical properties. MarloThem SH has been picked as it has a wide operating temperature range, good thermal conductivity for a HTF and has shown compatibility with other materials present in the PCS in previous experiments.

Encapsulation is used to enhance the heat transfer to and from the PCM particles. Next to that it can be used to prevent mixing or reacting of the PCM with the HTF by preventing contact between these two. ENG has been chosen for its large thermal conductivity and because it does not react with the other components. Next to that it has been used in combination with $LiNO_3$ in a previous study [32].

The implemented materials are summarized in Table 2.6.

Table 2.6: Selection of implemented materials

Component	Material
PCM	$LiNO_3$
HTF	MarloTherm SH
Encapsulation	Shape-stabilized ENG

Multiple method of phase change modeling have been described, including their strong and weak points. The choice of numerical method and mesh grid are made in Chapter 3.

3

Numerical representation of a pumpable phase change material system

A numerical model has been developed to represent the transient behavior in a pumpable PCM system using MATLAB. The model accounts for a parabolic through collector that absorbs radiation to heat up a slurry, containing PCM particles and a HTF. The model's purpose is given in Section 3.1 and a more detailed description is provided in Section 3.2. The energy is stored, both by sensible and latent heat, and transported to a heat exchanger (HEX) where the energy is released with respect to a fixed wall temperature. This chapter describes the design choices for the model in Section 3.3, the governing equations and the assumptions that have been provided in Section 3.4. The numerical model is explained in detail in Section 3.5. Furthermore Section 3.6 provides a sensitivity analysis and Section 3.7 provides verification and validation of the PCS model to arrive at the optimal design presented in Section 3.8.

3.1. Purpose

The objective of the numerical model of the pumpable PCM system is to analyze the transient behavior of such a system. The behavior depends on the input of solar radiation and the required output of heat delivered to the ORC. The numerical model is used to determine the optimal performance for such a system by identifying the effects of different parameters on the performance of the system. The model should be able to provide a representation of the state of the PCS in the PTC and the HEX based on the solar radiation input and the heat demand from the ORC.

3.2. Description of system

An overview of the modeled system is provided in this section. The first part of this system consists of a pipe that is uniformly heated by solar radiation. Through this pipe flows a PCS with a velocity u, consisting of encapsulated PCM particles and a HTF. This heat is stored in the PCS both by an increase in temperature in the PCS as well as a phase change in the PCM particles. The second part of the system consists of a HEX in which the heat that is stored in the first part of the system is used to heat up the working fluid of the ORC. A numerical model has been made for the combination of the PTC and HEX for one unit. To scale this process it is assumed that multiple units work in parallel, portraying the same properties. An overview of the system, including the location of the PCM in the system is provided in Figure 3.1.

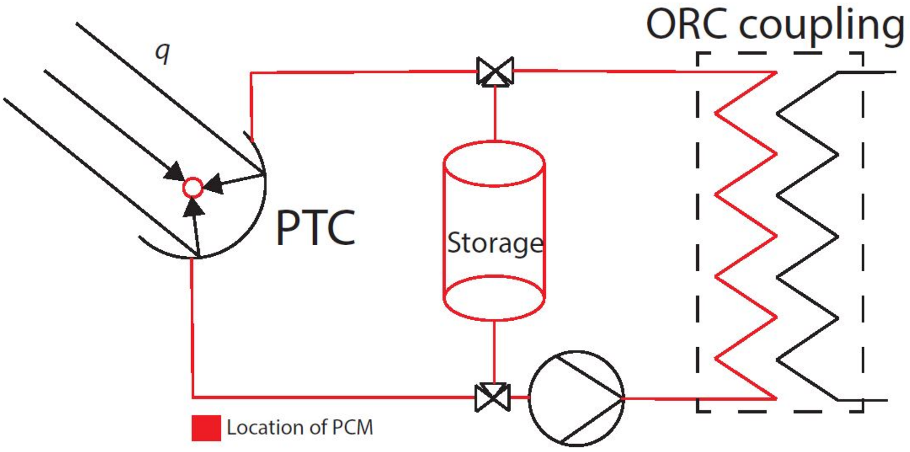

Figure 3.1: Process flow diagram of the PCS system with the location of the PCM indicated in red.

3.3. Design choices

Design choices have been conceived based on the performed literature study. By comparing the advantages and disadvantages of the reviewed methods one of the proposed methods has been selected for use in the study. Methods for formulating the mesh grid, the modeling of the slurry and the modeling of the phase change have been chosen.

Based on the researched mesh grids the mesh grid with equal area radial intervals has been selected. This selection is based on the fact that the mesh grid is simple to use and no external software is required to fabricate the mesh grid. Next to that it allows for the simplification that each control volume contains an equal number of PCM particles and it allows for a finer grid at the wall, where the largest increment in heat transfer is expected.

As provided in Section 2.4 the material properties of the PCM, capsule and the HTF have been unified to a homogeneous fluid. The PCM particles are physically separated from the HTF by the encapsulation and can therefore be treated in a separate model. This allows the PCM particles to be modeled as a source/sink that either takes up heat from the PCS when the PCS is being heated up or emits heat when the PCS is used to heat up the working fluid of the ORC.

Variable grid methods have been eliminated as an option due to the extensive computational power required to model these type of grids. The same applies to variable time methods. A fixed grid method has not been considered due to the fact that modeling a moving boundary layer requires a lot of computational work. Eliminating these methods leaves the weaker numerical methods, which require less computational power but also have a lower accuracy. However, the accuracy is sufficient for this study.
Both the heat integration method and the enthalpy method have been discarded as they require redundant steps for the problem that has to be modeled. Both methods require keeping track of both the temperature and the enthalpy in a control volume while the apparent heat capacity is a function of only the temperature in a control volume. Next to that these methods are known to have problems with stability around a phase change temperature range. Therefore the apparent heat capacity has been selected as method for modeling the phase change in the PCM particles. An advantage of this method is the possibility to implement subcooling and supercooling by implementation of a phase change temperature range over which the respective sub- and supercooling takes place.

3.4. Governing equations

Heat transfer in the PCS is present due to forced convection, natural convection, viscous dissipation and conduction. In the particle the driving force for heat transfer is conduction. In this section the governing equations for the heat transfer in the PCS and in the PCM particle are presented. Assumptions and simplifications have been presented and the effects they have on the governing equations have been documented.

3.4.1. Assumptions

Assumptions have been made for the behaviour of the PCS to be able to make a model that is not overly complicated. The reasoning behind every assumption and the influence on the numerical model have been provided.

- All processes are reversible. - No losses are present in the PCS and viscous dissipation is neglected. Efficiency of the system is defined in the used equipment if required.
- The PCS can be treated as a homogeneous fluid. - The particles are deemed to be sufficiently small and present in such a low concentration that the properties of the PCS can be modeled as a homogeneous material. This allows the three materials to be unified to a homogeneous fluid and its thermophysical and kinetic behaviour to represent the behavior of a homogeneous fluid. This assumption also indicates that the particle free layer at the wall of the pipe is negligible.
- The PCM particles are evenly distributed in the HTF and do not collide. - This assumption means that the fluid is taken to be stable and remains in its initial distribution of particles. The assumption of no collision allows the negligence of Brownian motion of the particles in the PCS. This leads to a lower viscosity of the slurry compared to when collision of particles is present in the PCS.
- The HTF is incompressible and can be modeled as a Newtonian fluid - Previous studies have proven that a suspension can be modeled as a Newtonian fluid up to a volumetric particle concentration of at least 25% [48]. Introducing compressibility and non-Newtonian behavior in the fluid make the governing equations more difficult to assess. Therefore the maximum volumetric particle concentration, Φ_p, is taken to be 0.25.
- All particles have the same size and shape; spherical. - To allow for the application of the viscosity equation the shape of the particles is deemed to be spherical and all particles have equal size. For the slurry to be treated as homogeneous not only do the particles have to be distributed equally but also their size has to be equal. Even though the coefficient of thermal expansion for parallel and perpendicular layered graphite is not equal the difference is so small that it is considered negligible.
- The thermophysical properties of the PCM and capsule are considered isotropic within a control volume. - To simplify calculations it is deemed that a control volume is sufficiently small to have a uniform temperature distribution, thus the particles in a control volume all exhibit the same properties and state.
- The velocity in the radial direction is zero. - Forced convection in the radial direction is non-existent. There is no forced convection term in radial direction in the governing equation for the PCS.
- Conduction in the axial direction is negligible compared to forced convection in the axial direction. - The conduction term in the axial direction is omitted from the heat transfer equation.
- The volume of the encapsulation of the PCM particles is based on the volume in solid phase. - The volumetric concentration of the PCM particles remains constant when changing phase. A fixed volumetric particle concentration is assumed in the start conditions and remains constant through time.

- Axisymmetric flow and heat flux in the tangential direction is present. - The PTC concentrates its received solar irradiance on the back of the pipe. It has been assumed that the concentration factor equals one such that there is no variation in heat flux in the tangential direction. This results in an axissymmetric flow such that there is no heat transfer in the tangential direction in the pipe and the state of the PCS in the top half of the pipe is equal to the state of the PCS in the bottom half of the pipe.
- Heat loss due to radiation from the PTC is considered to have a negligible effect on the steady state of the system - No radiation losses are implemented as boundary condition.

3.4.2. Heat transfer equation for the phase change slurry

Based on the assumptions that have been provided in Section 3.4.1 the governing equation for the heat transfer in the PCS becomes Equation (3.1). All cp parameters in the governing equations have been provided as volumetric specific heat capacity [J/m^3°C] as the volume that is present in the PTC at all times is known, limited by the dimensions of the PTC, while the mass is a function of the temperature. Therefore using the volumetric properties allows for a simpler numerical approach. The source term represents the heat transfer between the PCS and the PCM particles. The source term is negative when the PCM particles absorb heat from the slurry in the PTC and is positive when heat is extracted from the PCM particles in the HEX as defined in Equation (3.7). The source term is defined as the heat transfer rate per PCM particle $\dot{Q}_p$ multiplied with the number of particles per unit volume N_p.

$$cp_{PCS}\frac{\partial T}{\partial t} + cp_{PCS}u\frac{\partial T}{\partial z} = \frac{1}{r}\frac{\partial}{\partial r}\left(\lambda_e r\frac{\partial T}{\partial r}\right) + s \tag{3.1}$$

The axial velocity profile in the pipe is considered to represent laminar flow through a pipe with constant circular cross-section and a length that is significantly larger than its diameter, and is given in Equation (3.2). The flow is considered to be fully developed the moment that the flow enters the pipe. u_{mean} is the mean flow velocity in the pipe, r is the radial coordinate and R_{HEX} is the radius of the pipe. Based on the velocity in the pipe the local Reynolds number has been calculated using Equation (3.3).

$$u_i = 2u_{mean}\left(1 - \left(\frac{r_i}{R_{HEX}^2}\right)\right) \tag{3.2}$$

$$Re_i = \frac{\rho_{PCS}u_i 2r_i}{\mu_{PCS}} \tag{3.3}$$

Because of the enhancement created by the particle/fluid interactions the actual thermal conductivity of the PCS is larger than the combined thermal conductivity calculated using Equation (2.4). The effective thermal conductivity of the slurry is determined by Equation (3.6) and describes the increase in thermal conductivity due to an increase in natural convection because of the addition of particles to the HTF. In this equation B and m are constants dependent on the particle Peclet number as provided in Equation (3.4), based on empirical relations obtained through experiments [5], the ratio between the convective and diffusive heat transport given in Equation (3.5), and Φ is the volumetric concentration of the PCM particles. These constants are a function of the particle Peclet number The particle Peclet number is a function of the pipe radius R_{HEX} and the particle radius R_p, the local radial coordinate r_i, the local velocity u_i and the thermal diffusivity of the heat transfer fluid α_{HTF}.

$$B(Pe_p) = \begin{cases} 3.0 & \text{if } Pe_p \leq 0.67 \\ 1.8 & \text{if } 0.67 \leq Pe_p \leq 250 \\ 3.0 & \text{if } Pe_p \geq 250 \end{cases} \qquad m(Pe_p) = \begin{cases} 1.5 & \text{if } Pe_p \leq 0.67 \\ 1/11 & \text{if } 0.67 \leq Pe_p \leq 250 \\ 0.18 & \text{if } Pe_p \geq 250 \end{cases} \tag{3.4}$$

$$Pe_p = 8\frac{2R_{HEX}u_i}{\alpha_{HTF}}\left(\frac{R_p}{R_{HEX}}\right)^2 \frac{r_i}{R_{HEX}} \tag{3.5}$$

$$\lambda_e = \lambda_{PCS}(1 + B\Phi_p Pe_p^m) \tag{3.6}$$

The source term represents the heat transfer rate per particle multiplied by the number of particles in the PCS. The heat transfer rate per particle is dependent on the contact area, the temperature difference and the heat transfer coefficient between the particle and the HTF. The number of particles depends on the volumetric concentration and the volume of a particle.

$$s = \dot{Q}_p N_p = \left(-4\pi R_p^2 \lambda_p \frac{\partial T_p}{\partial r}|_{r=R_p}\right)\left(\frac{3\Phi_p}{4\pi R_p^3}\right) = \frac{3\Phi_p}{R_p} h_p (T_{p_{r=R_p}} - T_{PCS}) \tag{3.7}$$

According to the equations provided in Equation (3.8) the parameters that are used in the governing equation have been made dimensionless to allow for a better comparison of performance. Next to that it allows for an easy method to verify that the factors that are assumed to be negligible are indeed negligible. Dimensionless variables for temperature in Equation (3.8a), axial and radial distance in Equation (3.8b) and Equation (3.8c), thermal conductivity in Equation (3.8d), time in Equation (3.8e), the ratio of sensible heat to latent heat in the HTF and the PCS in Equation (3.8f) and Equation (3.8g) and a dimensionless variant of the previously introduced source term in Equation (3.8h) have been used for the dimensionless governing equation. T_m has been defined as the upper limit of the phase change temperature range, for $LiNO_3$ it has been taken to be 254.5 °C.

$$\theta = \frac{T - T_m}{(qR_{HEX}/\lambda_{PCS})} \tag{3.8a}$$

$$Z = \frac{z}{R_{HEX}Pe_{PCS}} \tag{3.8b}$$

$$\eta = \frac{r}{R_{HEX}} \tag{3.8c}$$

$$\Gamma = \frac{\lambda_e}{\lambda_{PCS}} \tag{3.8d}$$

$$Fo_{PCS} = \frac{\alpha_{PCS}t}{R_{HEX}^2} \tag{3.8e}$$

$$Pe_{HTF} = \frac{2R_{HEX}u}{\alpha_{HTF}} \tag{3.8f}$$

$$Pe_{PCS} = \frac{2R_{HEX}u}{\alpha_{PCS}} \tag{3.8g}$$

$$S = \frac{sR_{HEX}}{q} \tag{3.8h}$$

Implementing these dimensionless variables into Equation (3.1) results in the dimensionless form as specified by Equation (3.9). The velocity has been nondimensionalized as a function of the dimensionless radial coordinate as provided by Equation (3.2) and dividing by u_{mean}.

$$\frac{\partial\theta}{\partial Fo} + (1 - \eta^2)\frac{\partial\theta}{\partial Z} = \frac{1}{\eta}\frac{\partial}{\partial\eta}\left(\Gamma\eta\frac{\partial\theta}{\partial\eta}\right) + S \tag{3.9}$$

The boundary conditions (BCs) that have been imposed for the PTC are provided as well as the numerical form of these BCs. A graphical representation of the BCs is presented in Figure 3.2

- Inlet temperature, T_{in}, is equal to 250 °C for the first run due to start up of the system. Thereafter the inlet temperature is equal to the outlet temperature of the HEX, provided in Equation (3.10a).
- No heat transfer at the center of the pipe, provided in Equation (3.10b).

- Constant heat flux, q, is present at the wall of the pipe, provided in Equation (3.10c).

$$T = T_{in} \quad at \quad z = 0, r < R_{HEX} \qquad \theta = \theta_{in} \quad at \quad Z = 0, \eta < 1 \tag{3.10a}$$

$$\frac{\partial T}{\partial r} = 0 \quad at \quad r = 0 \qquad \frac{\partial \theta}{\partial \eta} = 0 \quad at \quad \eta = 0 \tag{3.10b}$$

$$\frac{\partial T}{\partial r} = \frac{q}{\lambda_e} \quad at \quad r = R_{HEX} \qquad \frac{\partial \theta}{\partial \eta} = \frac{1}{\Gamma} \quad at \quad \eta = 1 \tag{3.10c}$$

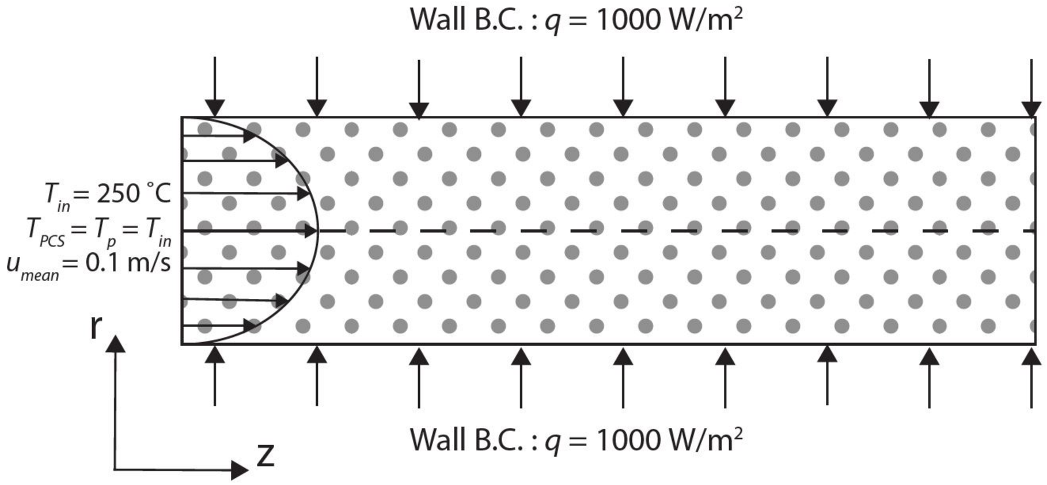

Figure 3.2: A depiction of a PTC pipe with the boundary conditions including: a constant heat flux q at the wall of 1000 W/m^2, inlet temperature of 250 °C and no heat transfer at the center of the pipe.

The HEX is located at the other side of the system and the collected heat at the PTC is released here to the ORC. The BCs that have been imposed for the HEX and the corresponding numerical forms have been provided. A visual representation of the BCs is found in Figure 3.3.

- The inlet temperature, T_{in} is equal to the outlet temperature of the PTC, provided in Equation (3.11a).
- No heat transfer at the center of the pipe, provided in Equation (3.11b).
- Constant wall temperature, T_w, of 245 °C. A constant wall temperature has been assumed as the working fluid of the ORC is present at the other side of the HEX at its boiling temperature, provided in Equation (3.11c).

$$T = T_{in} \quad at \quad z = 0, r < R_{HEX} \qquad \theta = \theta_{in} \quad at \quad Z = 0, \eta < 1 \tag{3.11a}$$

$$\frac{\partial T}{\partial r} = 0 \quad at \quad r = 0 \qquad \frac{\partial \theta}{\partial \eta} = 0 \quad at \quad \eta = 0 \tag{3.11b}$$

$$T = T_w \quad at \quad r = R_{HEX} \qquad \theta = -1 \quad at \quad \eta = 1 \tag{3.11c}$$

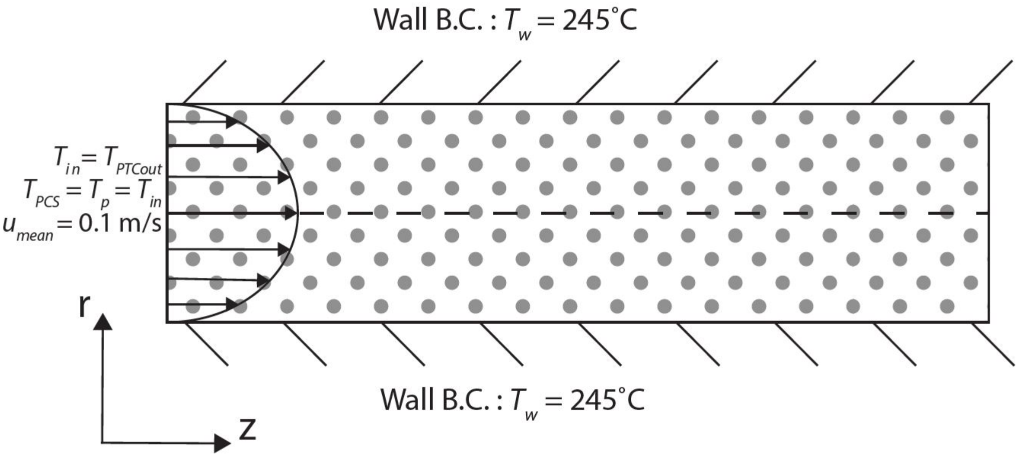

Figure 3.3: A depiction of a HEX pipe with the boundary conditions including: a constant wall temperature T_w of 245 °C, inlet temperature equal to the outlet temperature of the PTC and no heat transfer at the center of the pipe.

A special note has to be made regarding the non-dimensionalization of the temperature in the HEX as it is made dimensionless with respect to a constant wall temperature instead of a constant heat flux. This results in the non-dimensionalization of the temperature as stated in Equation (3.12).

$$\theta = \frac{T - T_m}{T_m - T_w} \tag{3.12}$$

3.4.3. Heat transfer equation for the phase change material particle

The heat transfer in a PCM particle is given by Equation (3.13). The heat transfer inside the particle is dominated by conduction while heat is absorbed from the HTF by convection.

$$cp_p \frac{\partial T_p}{\partial t} = \frac{1}{r_p^2} \frac{\partial}{\partial r_p} \left(\lambda_p r_p^2 \frac{\partial T_p}{\partial r_p} \right) \tag{3.13}$$

The apparent heat capacity method has been employed to model phase change in the PCM particle. When the temperature of the particle is below the melting temperature the specific heat capacity of the solid phase at the respective temperature is used for cp and when the temperature of the particle is above the melting temperature the liquid specific heat capacity is taken for that respective temperature. When the temperature of the particle lies within the phase change temperature range the specific heat ratio is defined as a ratio between the solid phase specific heat capacity and the liquid phase specific heat capacity supplemented by a factor $H_f/\Delta T$. This factor has been supplemented to account for the latent heat, artificially increasing the specific heat capacity to limit the temperature increase of the particle. An even distribution has been chosen, representing equal melting over the entire phase change temperature range as it is unknown how the melting is distributed and this option allows for a minimal error with respect to the actual distribution. Other possible representations are a sine curve or triangles which span the same area and are used when the melting phase peaks at a known temperature within the phase change temperature. The apparent specific heat capacity is defined as provided in Equation (3.14) and a graphical representation in Figure 3.4. The volumetric heat of fusion has been used.

$$cp_p(T_p) = \begin{cases} cp_s(T) & \text{if } T_p < T_m - \Delta T \\ \dfrac{cp_l - cp_s}{\Delta T}(T_p - (T_m - \Delta T)) + cp_s + \dfrac{H_f}{\Delta T} & \text{if } T_m - \Delta T \leq T_p \leq T_m \\ cp_l(T) & \text{if } T_p > T_m \end{cases} \tag{3.14}$$

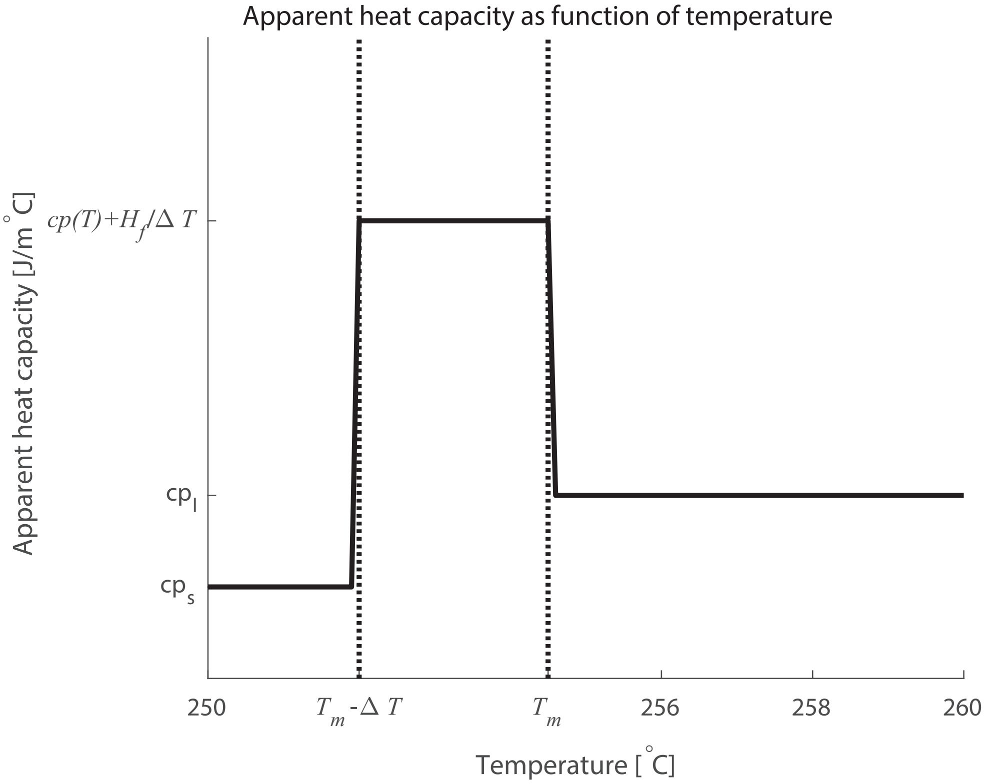

Figure 3.4: The apparent heat capacity as function of temperature as provided in Equation (3.14)

Dimensionless variables have been introduced for the heat transfer equation of the particle and are given in Equation (3.15). Equation (3.15) includes dimensionless variables for temperature of the particle in Equation (3.15a), time in Equation (3.15b), thermal conductivity of the particle in Equation (3.15c), phase change temperature range in Equation (3.15d), the ratio of sensible heat to latent heat in Equation (3.15e), known as the Stefan number, and for the particle radius in Equation (3.15f).

For the nondimensionalization of the governing equation of the PCM particles the thermal conductivity of the particle, λ_p, has been used contrary to the non dimensionalization of the PCS for which the thermal conductivity of the homogeneous slurry has been used. This is required as the temperature of the PCS in a control volume is not necessarily equal to the temperature of the PCM particles in that control volume. When the thermal conductivity of the PCS is used for the nondimensionalization of the temperature of the PCM particles it might result in a false representation of the temperature. An example is given in the fact that when the PCS is heated up while the particles are left out of the system the thermal conductivity of the PCS increases. If this thermal conductivity is then used for nondimensionalization of the temperature of the particles it is noted that the temperature of the particles has increased, despite not having entered the system.

The dimensionless function of the apparent heat capacity is provided in Equation (3.16). The conditions for which these variables take on the specified form have been represented in a dimensionless form too. ϵ is the dimensionless form of the phase change temperature range. As θ_p takes on a negative value when the particle is below the melting temperature the melting condition is met when θ_p is larger than the negative value of ϵ.

$$\theta_p = \frac{T_p - T_m}{(qR_{HEX}/\lambda_p)} \tag{3.15a}$$

$$\epsilon = \frac{\Delta T}{(qR_{HEX}/\lambda_p)} \tag{3.15d}$$

$$Fo_p = \frac{\alpha_p t}{R_p^2} \tag{3.15b}$$

$$Ste = \frac{cp_{PCS}(qR_{HEX}/\lambda_p)}{\Phi_p H_f} \tag{3.15e}$$

$$\Lambda_p = \frac{\lambda_p}{\lambda_{PCS}} \tag{3.15c}$$

$$r^* = \frac{r_p}{R_p} \tag{3.15f}$$

$$cp^*(\theta_p) = \begin{cases} \dfrac{cp_p}{cp_{PCS}} & \text{if } \theta_p < -\epsilon \\ \dfrac{cp_p}{cp_{PCS}} + \dfrac{1}{\Phi_p Ste\epsilon} & \text{if } -\epsilon \leq \theta_p \leq 0 \\ \dfrac{cp_p}{cp_{PCS}} & \text{if } \theta_p > 0 \end{cases} \tag{3.16}$$

Implementing the dimensionless variables defined in Equation (3.15) and Equation (3.16) into the governing equation defined in Equation (3.13) results in Equation (3.17).

$$cp^* \frac{\partial \theta_p}{\partial Fo} = \frac{1}{r^{*2}} \frac{\partial}{\partial r^*} \left(\Lambda_p r^{*^2} \frac{\partial \theta_p}{\partial r^*} \right) \tag{3.17}$$

The BCs that have been imposed for the PCM particle and the numerical form of these BCs include:

- Inlet temperature is equal to 250 °C for the first run due to start up of the system, provided in Equation (3.18a).
- Conductive heat transfer from the HTF to the particle at the edge of the particle, provided in Equation (3.18b) and depicted in Figure 3.5.
- No heat transfer at the center of the particle, provided in Equation (3.18c).

$$T = T_{in} \qquad at \qquad z = 0 \qquad \theta = \theta_{in} \qquad at \qquad Z = 0 \tag{3.18a}$$

$$-\lambda_p \frac{\partial T_p}{\partial r_p} = h_p(T_p - T_{PCS}) at \qquad r_p = R_p {-} \Lambda_p \frac{\partial \theta_p}{\partial r^*} = Nu_p(\theta_p - \theta) at \qquad r^* = 1 \tag{3.18b}$$

$$\frac{\partial T_p}{\partial r_p} = 0 \qquad at \qquad r_p = 0 \qquad \frac{\partial \theta_p}{\partial r^*} = 0 \qquad at \qquad r^* = 0 \tag{3.18c}$$

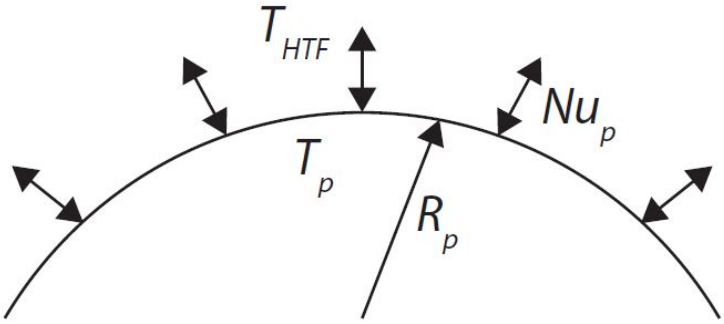

Figure 3.5: Overview of the paramaters that influence the particle conductive heat transfer that takes place until the HTF and the PCM particle have the same temperature.

The heat transfer between the HTF and the PCM particle is governed by the Nusselt number, the ratio between the convective and the conductive heat transfer across the boundary. As the PCM particles move with the HTF through the pipe at the same speed it has been assumed that there is no flow around a PCM particle. With this assumption the Nusselt number has been evaluated using a particle conduction model including eddy convection and molecular diffusion around the particles and the resulting equation is found in Equation (3.19) provided by Charunyakorn et al. [5]. The heat transfer between the PCS and a PCM particle is a function of the mean void fraction between the particles and the Biot number, which indicates the ratio between the heat transfer between the fluid and the particle and the conduction inside the particle [24]. A low Biot number indicates good conduction in a particle, resulting in a uniform temperature distribution in the particle and therewith an uniform temperature around the particle. For this conduction model to be valid the Biot number has to be small. The void fraction can be rewritten to the volumetric particle concentration.

$$Nu_p = \frac{\lambda_p}{\lambda_{PCS}} Bi_p = \frac{\lambda_e}{\lambda_p} \frac{2(1-\Phi_p)}{2-3\Phi_p^{1/3}+\Phi_p} \tag{3.19}$$

For the case of the HEX the non-dimensionalization of the Stefan number and the phase change temperature range have to be arranged according to the constant wall temperature, T_w. The Stefan number is given in Equation (3.20a) and the dimensionless phase change temperature range is provided in Equation (3.20b).

$$Ste = \frac{cp_{PCS}(T_w - T_m)}{\Phi_p H_f} \tag{3.20a}$$

$$\epsilon = \frac{\Delta T}{T_w - T_m} \tag{3.20b}$$

3.5. Numerical model

Based on the heat transfer equations presented in Section 3.4 the numerical model to represent the pumpable PCM system has been constructed. This section addresses the construction of the grid, the discretization of the governing equations and the iterative process required to come to a steady state in the system.

3.5.1. Grid

Two different grids are present in the numerical model. The grid, depicted in Figure 3.6, represents the pipe and the grid provided in Figure 3.7 represents a PCM particle.

The grid for the pipe is constructed using the method proposed in Section 3.3. The size of the control volumes are determined by dividing the size of the pipe by the desired number of control volumes. In the axial direction the size of each of the control volumes is identical while the size of the control volume in radial direction is varied according to Equation (2.7) to allow for each control volume to envelop equal volume. The grid only contains the top half of the pipe due to the presence of axisymmetric flow. The numbering of the cells starts at the inlet of the pipe for the axial direction, z, and at the outer wall for the radial direction, r.

Parameters that are required to construct the numerical mesh grid are the number of cells in radial and axial direction as well as the radial and axial length of the pipe to determine the coordinates of the control volumes.

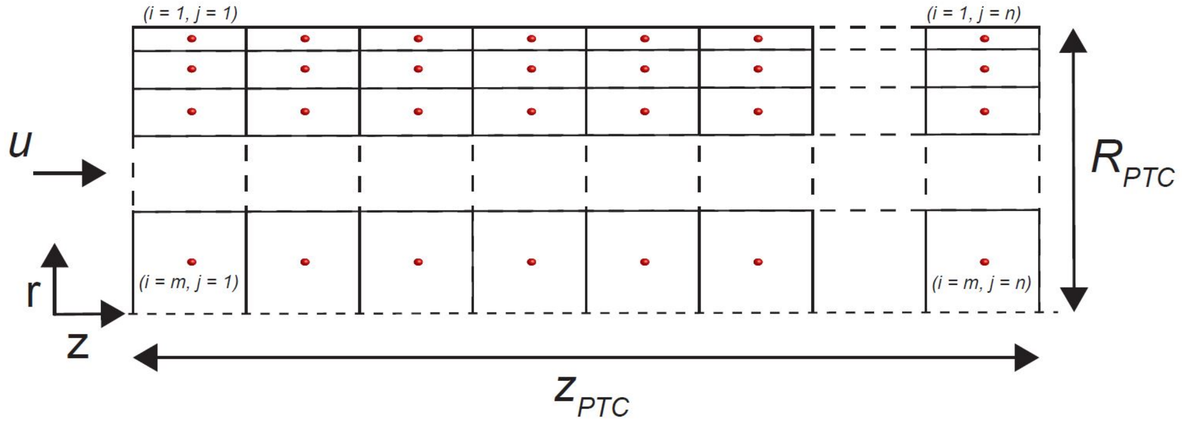

Figure 3.6: Numerical grid for the pipe with size z_{HEX} by $2R_{HEX}$ and m x n number of control volumes.

The grid for a particle is constructed by dividing the radius of the particle, R_p, into a p number of equidistant control volumes as depicted in Figure 3.7. The numbering of the control volumes starts at the outermost control volume. The grid for the particle models one particle per control volume. It has been assumed that all particles in a control volume have the same thermodynamic properties.

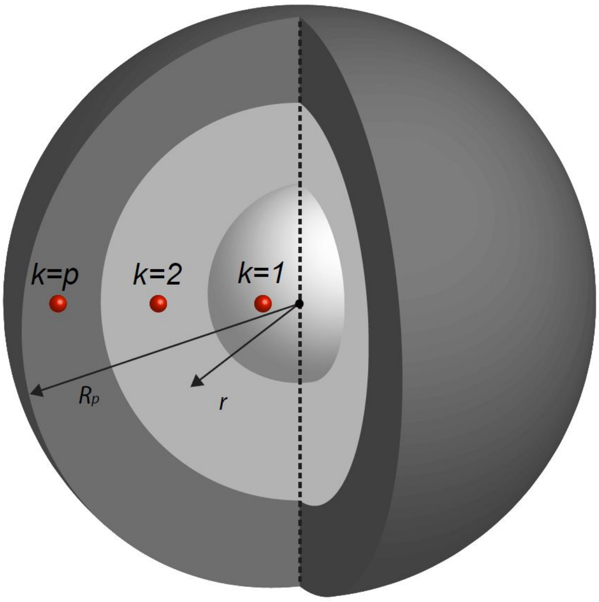

Figure 3.7: Numerical grid for a phase change material particle with radius R_p and p number of control volumes.

3.5.2. Discretization

To allow for a computational analysis of the system the heat transfer equations Equation (3.9) and Equation (3.17) have been discretized to fit the purpose of the model. An implicit finite differential method has been applied and is solved using a tridiagonal matrix algorithm (TDMA). An advantage of using an implicit method is that the stability of this method far exceeds the stability of an explicit method, allowing for a larger time step for the iterative process. The discretization of Equation (3.9) has been treated first. The differentials in this equation have been discretized as given in Equation (3.21), Equation (3.22), Equation (3.23) and Equation (3.24). The differential in axial direction has been discretized using an explicit backwards difference method to allow for faster computation. The discretization of ΔZ has been taken in the backwards axial direction for both the axial coordinate and the thermal diffusivity, α, of the PCS as provided in Equation (3.25). A control volume and the energy balance of a control volume as implied by the discretization is shown in Figure 3.8.

$$\frac{\partial \theta}{\partial Fo} = \frac{\theta^{n+1}(i,j) - \theta^{n}(i,j)}{\Delta Fo} \tag{3.21}$$

$$\frac{\partial \theta}{\partial Z} = \frac{\theta^{n}(i,j) - \theta^{n}(i,j-1)}{\Delta Z} \tag{3.22}$$

$$\frac{\partial \theta}{\partial \eta} = \frac{\theta^{n+1}(i+1,j) - \theta^{n+1}(i,j)}{\Delta \eta} - \frac{\theta^{n+1}(i,j) - \theta^{n+1}(i-1,j)}{\Delta \eta} \tag{3.23}$$

$$\Delta Fo = \frac{\alpha_{PCS}^{n} t^{n}}{R_{HEX}^{2}} - \frac{\alpha_{PCS}^{n-1} t^{n-1}}{R_{HEX}^{2}} \tag{3.24}$$

$$\Delta Z = \frac{z(i,j)}{R_{HEX} Pe_{PCS}(i,j)} - \frac{z(i,j-1)}{R_{HEX} Pe_{PCS}(i,j-1)} \tag{3.25}$$

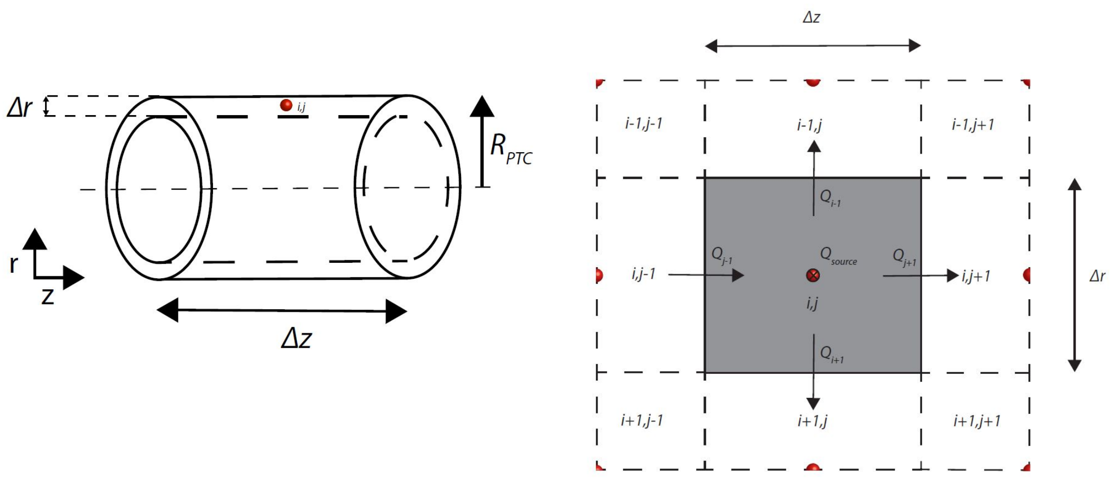

(a) Depiction of a control volume in the pipe containing PCS with size Δz by Δr.

(b) Energy balance of a control volume in the pipe with size Δz by Δr.

Figure 3.8: The location of a control volume with respect to the system and energy balance of a control volume with size Δz by Δr.

The implicit source term is defined as Equation (3.26) and represents the heat transfer between the PCS and the PCM particles in a control volume. It is a function of the convective heat transfer between the PCS and the particle, the volumetric particle concentration Φ_p and the difference in temperature between the PCS and the wall of a particle. The n+1 values for θ_p as well as θ are available to calculate this term.

$$S^{n+1}(i,j) = 3\Phi_p \left(\frac{R_{HEX}}{R_p}\right)^2 Nu_p(\theta^{n+1}_{p_{r^*=1}} - \theta^{n+1}) \tag{3.26}$$

Filling in Equation (3.21), Equation (3.22) and Equation (3.23) into Equation (3.9) results in Equation (3.27). Next all n+1 terms have been moved to the left side of the equation while the n terms and constants have been to the right side of the equation, resulting in Equation (3.28).

$$\begin{gathered}\frac{\theta^{n+1}(i,j) - \theta^{n}(i,j)}{\Delta Fo} + (1-\eta^2)\frac{\theta^{n}(i,j) - \theta^{n}(i,j-1)}{\Delta Z} + S^{n+1}(i,j) = \\ \frac{1}{\eta}\frac{1}{\Delta\eta}\left(\Gamma\eta\left(\frac{\theta^{n+1}(i+1,j) - \theta^{n+1}(i,j)}{\Delta\eta} - \frac{\theta^{n+1}(i,j) - \theta^{n+1}(i-1,j)}{\Delta\eta}\right)\right)\end{gathered} \tag{3.27}$$

$$\begin{gathered}\theta^{n+1}(i,j) + \frac{\Gamma\Delta Fo}{\Delta\eta^2}(\theta^{n+1}(i+1,j) - 2\theta^{n+1}(i,j) + \theta^{n+1}(i-1,j)) + \Delta Fo S(\theta)^{n+1}(i,j) = \\ \theta^{n}(i,j) - \Delta Fo(1-\eta^2)\frac{\theta^{n}(i,j) - \theta^{n}(i,j-1)}{\Delta Z} - \Delta Fo S(\theta_p)^{n+1}(i,j)\end{gathered} \tag{3.28}$$

To solve Equation (3.28) for θ a TDMA has been used. This method creates a diagonal matrix with terms a_i, b_i and c_i on the diagonal to incorporate the terms on the left hand side in Equation (3.28). This method solves the matrix Aθ = b allowing for fast computation of the n+1 terms as it removes the need for an iterative process to solve the unknown terms for θ^{n+1} . For this method to be stable it is required to be diagonally dominant. To accommodate for the TDMA the θ terms have been split. All terms equal to (i+1,j) form the lower diagonal, the terms for (i-1,j) form the upper diagonal and the (i,j) terms make up the diagonal of the tridiagonal matrix. The source term has been split up in two terms, one term that is a function of θ and one term that is a function of θ_p. The term that is a function of θ is transferred to the left side of the equation while the term that is a function of θ_p remains on the right hand side (RHS). This has been done to keep the diagonal of the TDMA more dominant, improving the stability of this method.

$$\begin{gathered}\left(1+\frac{2\Gamma\Delta Fo}{\Delta\eta^2}+3\Phi_p\left(\frac{R_{HEX}}{R_p}\right)^2 Nu_p\Delta Fo\right)\theta^{n+1}(i,j)+\\ \left(-\frac{\Gamma\Delta Fo}{\Delta\eta^2}\right)\theta^{n+1}(i+1,j)+\left(-\frac{\Gamma\Delta Fo}{\Delta\eta^2}\right)\theta^{n+1}(i-1,j)=RHS\end{gathered} \tag{3.29}$$

$$RHS=\theta^n(i,j)-\Delta Fo(1-\eta^2)\left(\frac{\theta^n(i,j)-\theta^n(i,j-1)}{\Delta Z}\right)+3\Phi_p\left(\frac{R_{HEX}}{R_p}\right)^2 Nu_p\theta_{p_{r^*=1}}^{n+1}\Delta Fo+BC \tag{3.30}$$

The value of Γ has been averaged between the values of the adjoined control volumes to represent the value at the boundary of the control volume at which the heat transfer takes place according to Equation (3.31). Γ is the only parameter in the heat transfer equation for the PCS that has been taken to vary over a control volume.

$$\Gamma(i+1/2,j)=\frac{\Gamma(i,j)+\Gamma(i+1,j)}{2} \tag{3.31a}$$

$$\Gamma(i-1/2,j)=\frac{\Gamma(i,j)+\Gamma(i-1,j)}{2} \tag{3.31b}$$

Equation (3.29) has then been solved implicitly using the tridiagonal matrix depicted in Figure 3.9. The matrix Aθ = b is constructed from the θ terms, the RHS and the applicable boundary conditions. The RHS contains all known terms as given by Equation (3.30), supplemented by the boundary conditions. The boundary condition as provided in Equation (3.10) is added to the RHS at the location (1,j), because the heat flux is added to the system at the out most control volume. The diagonal term for the first and last entry is smaller than the other diagonal terms due to the fact that there is no control volume present either above or below it and therefore the addition that these control volumes have in the other control volumes is discarded. The matrix has been solved to find the terms for θ. A more detailed version of this matrix is found in Appendix B.

$$\begin{bmatrix} 1+\Delta Fo\left(\frac{\Gamma}{\Delta\eta^2}+3\Phi_p\left(\frac{R_{HEX}}{R_p}\right)^2 Nu_p\right) & -\frac{\Gamma\Delta Fo}{\Delta\eta^2} & 0 & 0 & \cdots & 0 \\ -\frac{\Gamma\Delta Fo}{\Delta\eta^2} & 1+\Delta Fo\left(\frac{2\Gamma}{\Delta\eta^2}+3\Phi_p\left(\frac{R_{HEX}}{R_p}\right)^2 Nu_p\right) & -\frac{\Gamma\Delta Fo}{\Delta\eta^2} & 0 & \ddots & 0 \\ 0 & -\frac{\Gamma\Delta Fo}{\Delta\eta^2} & 1+\Delta Fo\left(\frac{2\Gamma}{\Delta\eta^2}+3\Phi_p\left(\frac{R_{HEX}}{R_p}\right)^2 Nu_p\right) & -\frac{\Gamma\Delta Fo}{\Delta\eta^2} & \ddots & 0 \\ \vdots & \ddots & \ddots & \ddots & \ddots & \vdots \\ 0 & 0 & 0 & 0 & \cdots & 1+\Delta Fo\left(\frac{\Gamma}{\Delta\eta^2}+3\Phi_p\left(\frac{R_{HEX}}{R_p}\right)^2 Nu_p\right) \end{bmatrix} \begin{bmatrix} \theta^{n+1}(1,j) \\ \theta^{n+1}(2,j) \\ \theta^{n+1}(3,j) \\ \vdots \\ \theta^{n+1}(i_{max},j) \end{bmatrix} = \text{RHS + BC}$$

Figure 3.9: A concise version of the TDMA that has been created to solve the governing heat transfer equation for the PCS.

Discretization of the particle starts at Equation (3.17). The discretized forms of the partial derivatives have been provided in Equation (3.32) and Equation (3.33). The Fourier number has been discretized explicitly to allow for a shorter computational duration as per Equation (3.34). Putting the discretized forms of the partial derivatives into Equation (3.17) results in Equation (3.35). A visualization of the energy balance of a control volume at a cell k for the presented discretization is given in Figure 3.10.

$$\frac{\partial\theta_p}{\partial Fo} = \frac{\theta_p(k)^{n+1} - \theta_p(k)^n}{\Delta Fo} \tag{3.32}$$

$$\frac{\partial\theta_p}{\partial r^*} = \frac{\theta_p^{n+1}(k+1) - \theta_p^{n+1}(k)}{\Delta r^*} - \frac{\theta_p^{n+1}(k) - \theta_p^{n+1}(k-1)}{\Delta r^*} \tag{3.33}$$

$$\Delta Fo_p = \frac{\alpha_p^n t^n}{R_p^2} - \frac{\alpha_p^{n-1} t^{n-1}}{R_p^2} \tag{3.34}$$

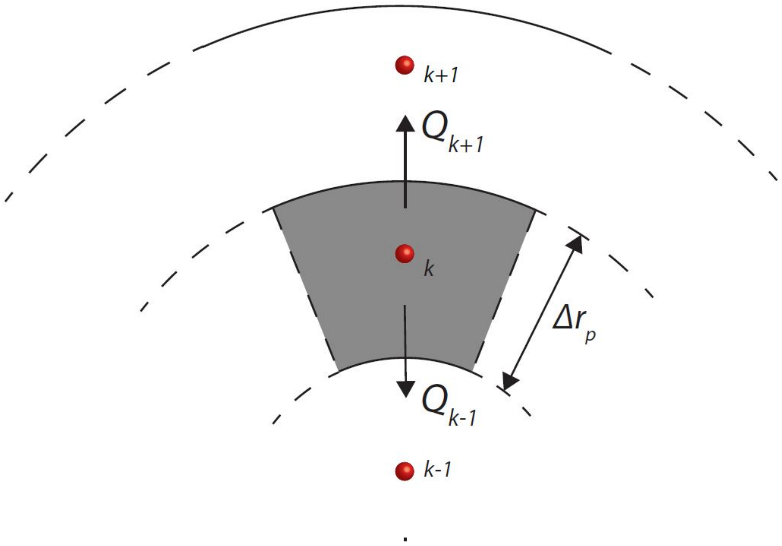

Figure 3.10: Energy balance of a control volume in the particle with size Δr_p.

$$cp^{*^{n+1}}(k)(\theta_p(k)^{n+1}-\theta_p(k)^n)=$$
$$\frac{\Delta Fo_p}{\Delta r^*}\left(\Lambda\left(\frac{\theta_p^{n+1}(k+1)-\theta_p^{n+1}(k)}{\Delta r^*}-\frac{\theta_p^{n+1}(k)-\theta_p^{n+1}(k-1)}{\Delta r^*}\right)\right) \tag{3.35}$$

Again all n+1 terms have been moved to the left side of the equation while the n terms make up the right hand side of Equation (3.36). The terms are split to enable the formation of the tridiagonal matrix. The (k) terms form the diagonal, the (k+1) terms form the lower diagonal and the (k-1) terms form the upper diagonal of this tridiagonal matrix.

$$\left(-\frac{\Delta Fo_p}{\Delta r^{*^2}}\Lambda\right)\theta(k+1)^{n+1}+\left(cp^{*^{n+1}}+\frac{2\Delta Fo_p}{\Delta r^{*^2}}\Lambda\right)\theta(k)^{n+1}+\left(-\frac{\Delta Fo_p}{\Delta r^{*^2}}\Lambda\right)\theta(k-1)^{n+1}=RHS \tag{3.36}$$

The right hand side of the equation is provided in Equation (3.37). A BC has been applied at the first term to account for the conductive heat transfer from the PCS to the particle as provided in Equation (3.18b), this term has been discretized implicitly.

$$RHS=\theta_p^n(k)cp^{*^{n+1}}+BC \tag{3.37}$$

Λ is the only variable in the PCM particle that has been varied over the control volume and therefore has been averaged according to Equation (3.38) to represent the value at the boundary of a control volume.

$$\Lambda(k+1/2)=\frac{\Lambda(k)+\Lambda(k+1)}{2} \tag{3.38a}$$
$$\Lambda(k-1/2)=\frac{\Lambda(k)+\Lambda(k-1)}{2} \tag{3.38b}$$

Based on Equation (3.36) and Equation (3.37) the tridiagonal matrix Aθ_p=b has been constructed and solved to find θ_p. A more detailed version of the tridiagonal matrix has been provided in Appendix B.

$$\begin{bmatrix} cp^{*^{n+1}} + \frac{\Delta Fo_p}{\Delta r^{*^2}}\Lambda & -\frac{\Delta Fo_p}{\Delta r^{*^2}}\Lambda & 0 & 0 & \cdots & 0 \\ -\frac{\Delta Fo_p}{\Delta r^{*^2}}\Lambda & cp^{*^{n+1}} + \frac{2\Delta Fo_p}{\Delta r^{*^2}}\Lambda & -\frac{\Delta Fo_p}{\Delta r^{*^2}}\Lambda & 0 & \ddots & 0 \\ 0 & -\frac{\Delta Fo_p}{\Delta r^{*^2}}\Lambda & cp^{*^{n+1}} + \frac{2\Delta Fo_p}{\Delta r^{*^2}}\Lambda & -\frac{\Delta Fo_p}{\Delta r^{*^2}}\Lambda & \ddots & 0 \\ \vdots & \ddots & \ddots & \ddots & \ddots & \vdots \\ 0 & 0 & 0 & 0 & \cdots & \begin{matrix} cp^{*^{n+1}} + \frac{\Delta Fo_p}{\Delta r^{*^2}}\Lambda + \\ \frac{\Delta Fo_p}{\Delta r^{*}} Nu_p \end{matrix} \end{bmatrix} \begin{bmatrix} \theta_p^{n+1}(1) \\ \theta_p^{n+1}(2) \\ \theta_p^{n+1}(3) \\ \vdots \\ \theta_p^{n+1}(k_{max}) \end{bmatrix} = \text{RHS} + \text{BC}$$

Figure 3.11: A concise version of the TDMA that has been constructed to solve the governing equation for the PCM particle.

3.5.3. Iterative process

The iterative process that is required to come to a steady state for a specified solar heat flux input into the pumpable PCS is provided in a process flow diagram in Figure 3.12. After the grid has been created for the discretization starting values for T_p and T_{pcs} are assumed and used as input for the iteration. Using these temperatures the material properties ρ_p, ρ_{pcs}, λ_p, λ_{pcs}, cp_p, cp_{pcs} and μ_{pcs} are determined. These material properties have been interpolated from the experimental data provided in Appendix A. A fit has been made from these data to allow for a fast computational process. These fits are provided in Appendix A.

Using these material properties the dimensionless numbers are worked out. The new temperature of the particle is determined next. With this particle temperature the new value of the apparent heat capacity is calculated and checked with the apparent heat capacity of the previous step. If the apparent heat capacity does not correspond to the particle temperature from the previous iteration it is calculated again using the new apparent heat capacity. This check has been applied to prevent oscillation between two phases due to an increment in apparent heat capacity.

Using the obtained particle temperature the source term has been determined and filling this into the heat transfer equation for the PCS the new temperature of the slurry is calculated. If the error between the old and the new slurry temperature is smaller than 1×10^{-6} steady-state is assumed in the system. Otherwise the updated particle and PCS temperatures are used to calculate the material properties and start a new iteration at the next time step. Once the time period during which the heat flux is constant ends the iterative process is initiated from the start again.

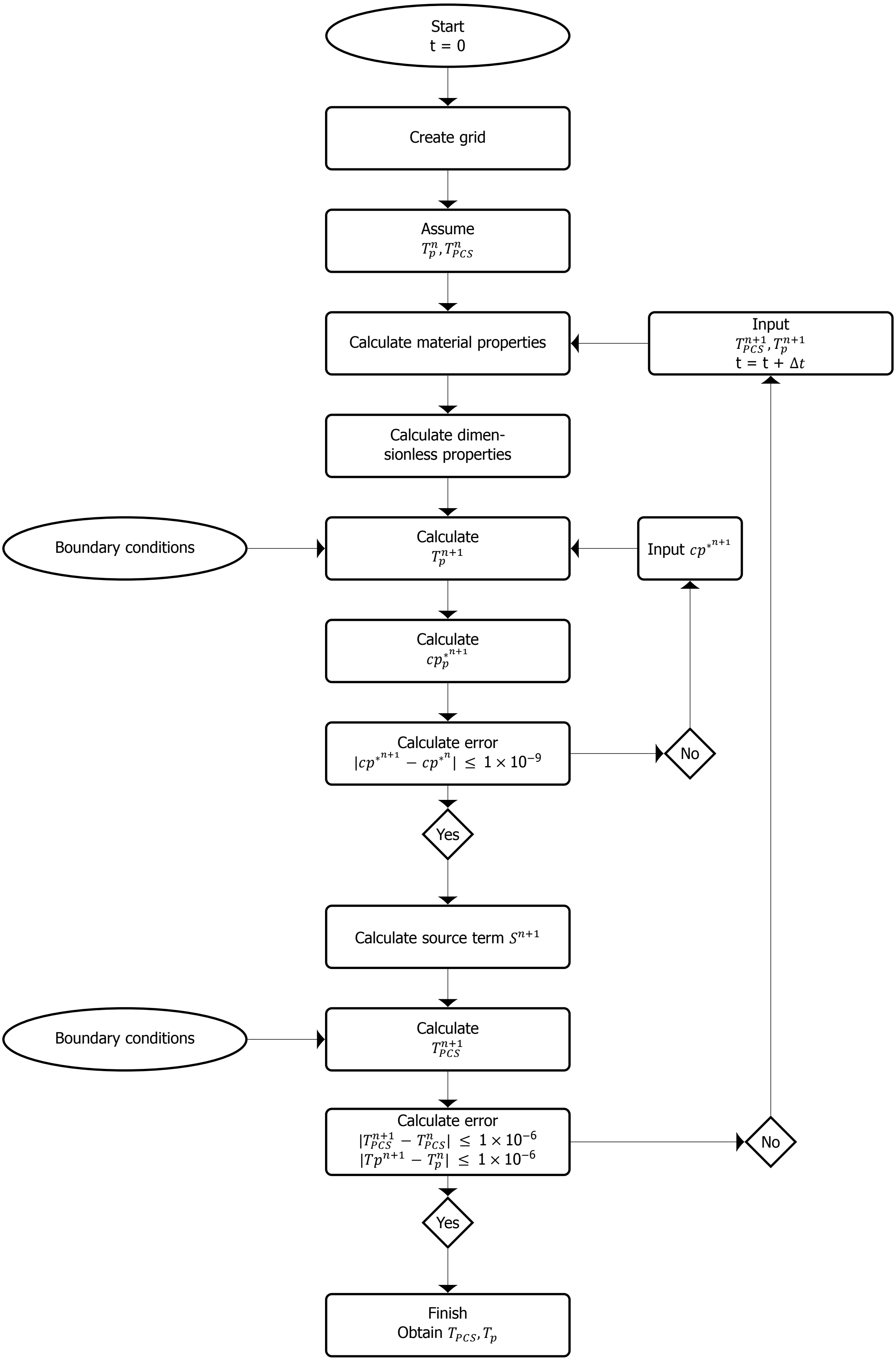

Figure 3.12: Process flow diagram of the iterative process for the numerical model of the pumpable PCS system.

3.6. Sensitivity analysis

The goal of the study is to compare the efficiency of the pumpable PCM system to the S&T system modeled by Fan. To be able to provide a meaningful comparison between these two models it is required that the pumpable PCM system is designed for optimal efficiency. Optimal efficiency in this case is defined as the ability to store and transport heat, a large ratio between the latent heat and the sensible heat stored, resulting in a low wall temperature and large energy density. A lower wall temperature shows both the ability for heat to penetrate better in the PCS and for better latent heat storage. Furthermore the thermal power loss of a PTC is dependent on the wall temperature as defined by Equation (3.39). Here U is a parameter that indicates the overall heat transfer coefficient, based on the type op equipment, T_w is the temperature at the maximum radial dimension, T_a is the ambient temperature and A is the surface area of the PTC. Another important property is the ability for heat to penetrate into the system, thus having an equal temperature distribution in the radial direction. Next to the performance the time until steady state has been calculated and compared when deemed useful.

$$Q_{loss} = UA(T_w - T_a) \tag{3.39}$$

A sensitivity analysis has been performed to obtain the optimal sizing of the system. For each sensitivity analysis one parameter has been assigned as variable while the remaining parameters have been kept constant to perform a fair analysis. To come to the optimal performance for the PTC a combination of these parameters will be taken to come to a system that has a large ratio between latent and sensible heat storage. The value that leads to the best performance for one parameter may not necessarily be selected if it is believed to clash with another parameter. The parameters that have been varied for the sensitivity analysis include:

- Pipe radius, R_{PTC}
- PCM particle concentration, Φ_p
- Particle radius to pipe radius ratio, $\frac{R_p}{R_{PTC}}$
- Mean flow velocity, u_{mean}
- Pipe axial length, z_{PTC}
- Volumetric PCM particle concentration, Φ_{PCM}

Next to these physical parameters the effects of the parameters present in the numerical analysis have been subject to a sensitivity analysis to determine the effect of these parameters on the outcome of the model to thereby assess the quality of the numerical analysis. The numerical parameters that have been subjected to investigation are:

- Phase change temperature range, ΔT
- Heat of fusion, H_f
- Time step, Δt
- Inlet temperature, T_{in}
- Number of control volumes in axial dimension, N_z
- Number of control volumes in radial dimension, N_r
- Number of control volumes in radial particle dimension, N_{r_p}

Based on the range that is physically possible, values have been assigned to test for each parameter. An overview of these values is found in Table 3.1. For the PCM particle an analysis has been performed over the previously assigned range of 0.4 μm to 400 μm in which a particle is considered to be in the micro-scale. The volumetric particle concentration has been analyzed over the range of a HTF without any PCM particles up to a volumetric particle concentration of 0.25 at which the PCS can still be considered a Newtonian fluid. The particle radius to pipe radius ratio, which influences the number of PCM particles present across the radial dimension of the pipe, has been varied for values between 0.01 and 0.2. Above a ratio of 2.0 the pipe experiences a large pressure drop due to clogging. The axial length has been varied over a wide range of 0.5 up till 50 m to find the influence of the axial length. The volumetric PCM concentration in the particle has been varied over the entire spectrum of having no encapsulation up to the part at which the particle is completely made up of encapsulation material. The inlet temperature has been varied to identify the influence of the amount of heat that is required before the melting phase of the PCM particles has been reached. The upper limit for the inlet temperature has been set at 251.5 °C to make sure the particles at the inlet are completely in solid phase.

The grid for the reference values is quite coarse. The number of control volumes for the axial length and radial dimension as well as the particle radius have been increased to test the influence of a finer grid. The same reasoning applies to running an analysis with a smaller time step. The incoming solar irradiance has been adjusted to represent the incoming flux in the morning, the peak incoming flux and the peak incoming flux concentrated by the PTC. Lastly the phase change temperature range and heat of fusion have been defined as a numerical parameter. These values are fixed for the chosen material and therefore these can not be sized, however it is interesting to find out how the system behaves when these parameters change.

The values that have been picked for the sensitivity analysis are provided in ascending order in Table 3.1. The third column represents the reference values that have been chosen to resemble the median of the tested range and have been kept constant throughout the sensitivity analysis. Only the reference value of the volumetric particle concentration has been kept at a maximum value as it is interesting to find out how the system behaves when PCM particles are present in the system. For every analysis one parameter has been taken to vary while the remaining parameters have been kept at their reference value.

Table 3.1: Parameters and the values that have been used for the performed sensitivity analysis. The values in the third column present the reference case. For each analysis one parameter has been varied while the other parameters have been kept at their reference value.

Physical Parameter	**Unit**	**Reference value**	**Value 1**	**Value 2**	**Value 3**	**Value 4**
R_p	m	400×10^{-7}	400×10^{-5}	400×10^{-6}	400×10^{-8}	400×10^{-9}
R_p/R_{PTC}	-	0.04	0.01	0.02	0.10	0.20
Φ_p	vol%	25	0	5.0	10	20
u_{mean}	m/s	0.10	0.01	0.05	0.50	1.0
z_{PTC}	m	2.0	1.0	5.0	10	50
Φ_{PCM}	vol%	70	0.0	25	50	100
T_{in}	$^{\circ}C$	250	245	251.5		
Numerical Parameter						
ΔT	$^{\circ}C$	2.5	0.0	1.0		
H_f	kJ/kg	360	0	180	540	
Δt	s	0.1	0.01			
q	W/m^2	1000	250	25000		
N_z	-	10	25	50		
N_r	-	10	25	50		
N_{r_p}	-	3	25	50		

In the sensitivity analysis not necessarily the best options as a whole have been tested. Because only one parameter is varied at a time, the other parameters can have a non optimal value. Therefore the best configuration is not present in the sensitivity analysis and will be decided upon later, based on the influence of the tested parameters.

The dimensionless outlet temperature has been chosen to assess the performance of the PTC. It is defined as Equation (3.8a), where T is taken to be the temperature at the outlet. From the dimensionless outlet temperature it is clear if the PCM particles have melted and the dimensionless outlet temperature scales with a change in incoming heat flux, allowing for a fair comparison when the heat flux varies. A low outlet temperature is preferable as this indicates that a larger fraction of the heat input is stored as latent heat, contrary to sensible heat. Next to that the difference between the outlet temperature at the wall of the PTC and the outlet temperature at the center of the PTC is preferred to be minimal because it indicates that the PCM is used most optimally for storing heat.

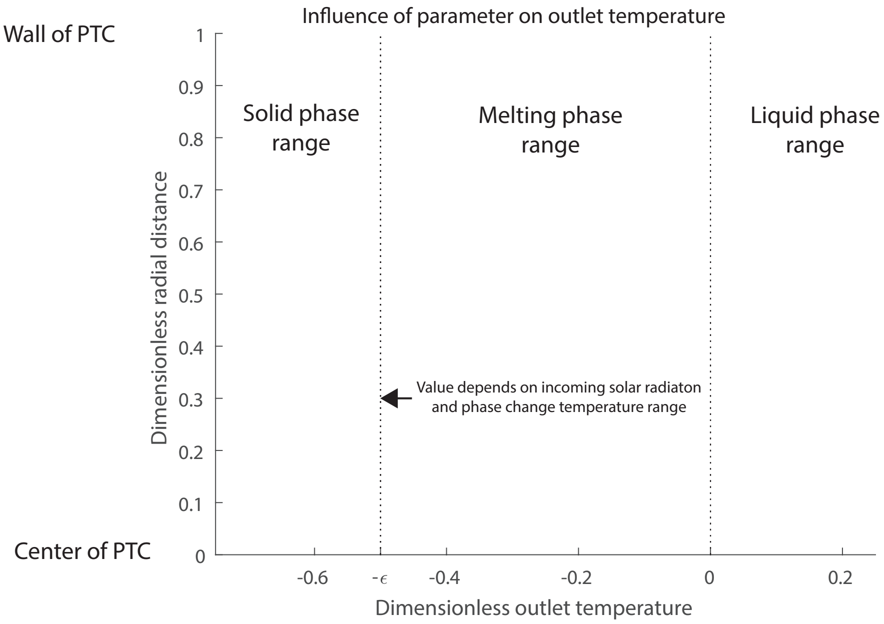

Figure 3.13: Explanation of the lay-out of the sensitivity plots.

In Figure 3.13 the lay-out of the plots used in the sensitivity analysis is explained. The vertical line at the zero point indicates the temperature at which the PCM has fully melted. ϵ, the value at which the PCM particles start to melt as defined by Equation (3.15d), has been added to the plots whenever this dimensionless parameter remains constant, when the incoming solar radiation and phase change temperature range are not variables.

Next to this the ratio in which the incoming energy has been stored between sensible and latent heat has been assessed and provided as well as the melt fraction at the outlet. Conditions that have a low temperature, have a small gradient in temperature between the center of the PTC and the wall of the PTC are favorable. When the outlet temperature for a condition is low it means that more heat is stored as latent heat as the same amount of total heat is present in the system.

Varying of particle radius has a direct influence on the radius of the pipe as the ratio between the particle and the pipe radius remains unchanged. This has an influence in the dimensionless radial grid size $\Delta\eta$ and the dimensionless time steps ΔFo and ΔFo_p. Next to that an increase in radius of the pipe results in a larger surface area of the PTC, therewith increasing the total incoming solar flux. However the increase in mass flow is proportionally larger than the increase in surface area, therefore a smaller pipe radius results in a better heat transfer. Also both the Peclet numbers of the PCS and the PCM particle increase.
A decrease of particle to pipe radius ratio results in more particles next to each other in the radial direction. This results in a larger number of PCM particles per control volume and therewith a larger source term for the PCS. Next to that the same parameters change as mentioned for the change in the particle radius. The influence on the dimensionless outlet temperature of the particle radius is depicted in Figure 3.14a and the influence of the particle to pipe radius ratio has been provided in Figure 3.14b.

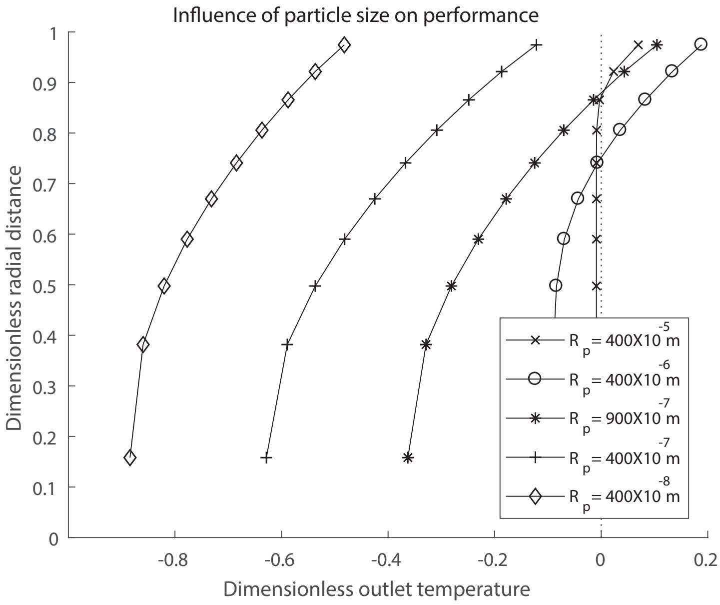

(a) Effect of varying the particle radius on the dimensionless outlet temperature.

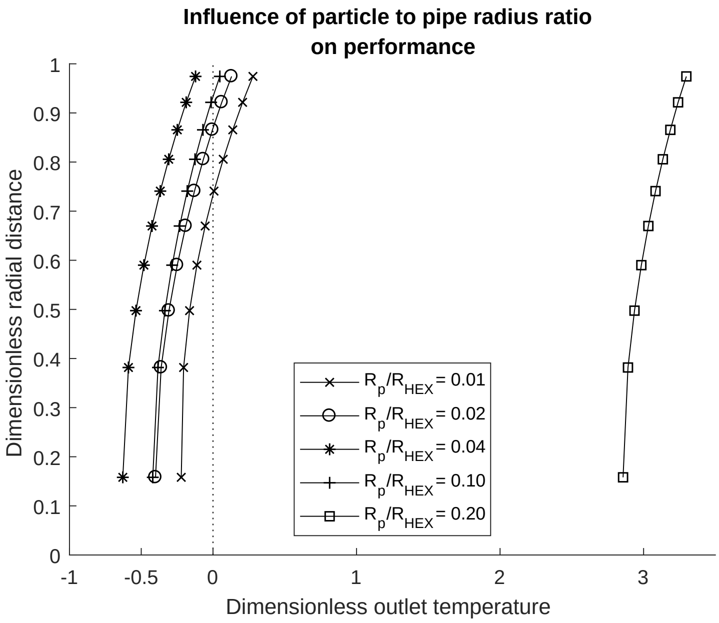

(b) Effect of varying the particle to pipe radius ratio on the dimensionless outlet temperature.

Figure 3.14: Effect of varying the radial dimension of the PTC on dimensionless outlet temperature. The remaining parameters have been kept constant at Φ_p = 0.25, u_{mean} = 0.1 m/s, z_{PTC} = 2.0 m and Φ_{PCM} = 0.70

From Figure 3.14a it is found that a smaller particle radius and with it a smaller pipe radius results in a lower dimensionless outlet temperature. Particle radii smaller than 400×10^{-8} have not been included as no convergence has been achieved in the model for these values. A small particle radius results in a lower dimensionless outlet temperature, mostly because the radius of the pipe changes as well, resulting in a lower surface area of the PTC. This is due to the fact that a smaller particle has a larger ratio of surface area to volume and can therefore easier take up heat. For the particle to pipe radius ratio it is seen that the optimal ratio lies between 0.02 and 0.10 as a ratio of 0.04 results in the lowest dimensionless outlet temperature. This is due to the change in the particle Peclet number and the source term. The particle Peclet number increases when the particle over pipe radius increases however the source term decreases, causing an optimum between a ratio of 0.02 and 0.10.

It is expected that a large volumetric particle concentration is beneficial for the performance of the PCS due to the fact that the possibility to store heat as latent heat is increased with an increase in the volumetric particle concentration, resulting in a smaller Stefan number as defined in Equation (3.15e). Next to that the thermophysical properties of the PCS change with the volumetric particle concentration as provided in Table 2.5. The only downside to an increase in volumetric particle concentration is the increase in viscosity of the PCS as found in Figure 2.5, resulting in a larger required pumping power to maintain the mean flow velocity in the system. In Figure 3.15 it is clearly seen that the dimensionless outlet temperature decreases for a larger volumetric particle concentration.

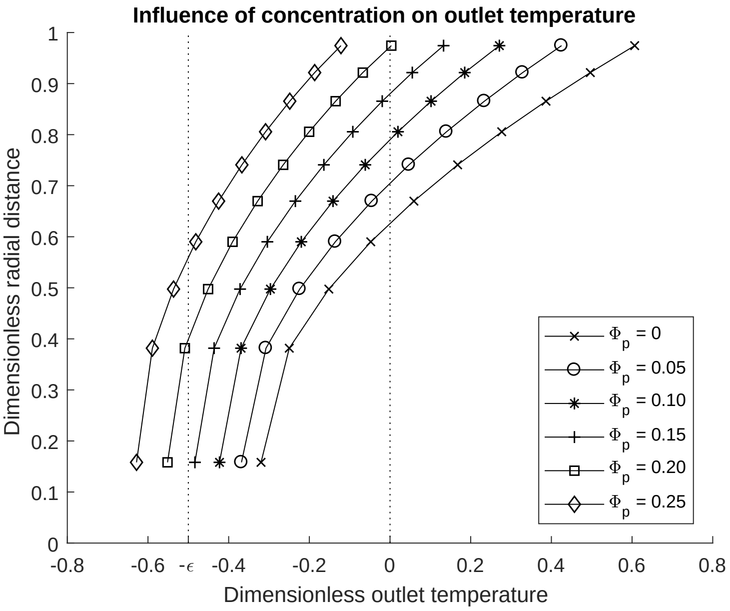

Figure 3.15: Effect of varying the volumetric particle concentration on the dimensionless outlet temperature. The remaining parameters have been kept constant at R_p = 400 × 10^{-7} m, R_p/R_{PTC} = 0.04, u_{mean} = 0.1 m/s, z_{PTC} = 2.0 m and Φ_{PCM} = 0.70

The mean flow velocity has influence on the size of ΔZ through the Peclet number and the Reynolds number increases proportionally with an increase in mean velocity. A larger Peclet number also influences the effective thermal conductivity in a positive way. Next to that the size of ΔZ changes and the effective thermal conductivity increases with an increase in u_{mean}. ΔZ also alters when the axial length of the PTC is altered. Furthermore, varying of axial length results in a change in incoming solar irradiance as the surface area of the PTC is altered. A higher dimensionless outlet temperature is expected for a low u_{mean} and a large z_{PTC} due to an increase in residence time of the PCS in the PTC.

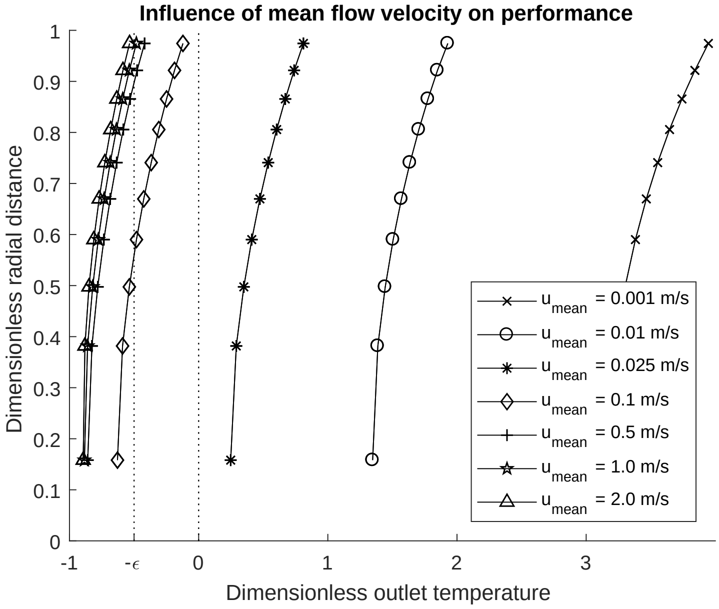

(a) Effect of varying mean flow velocity on the dimensionless outlet temperature.

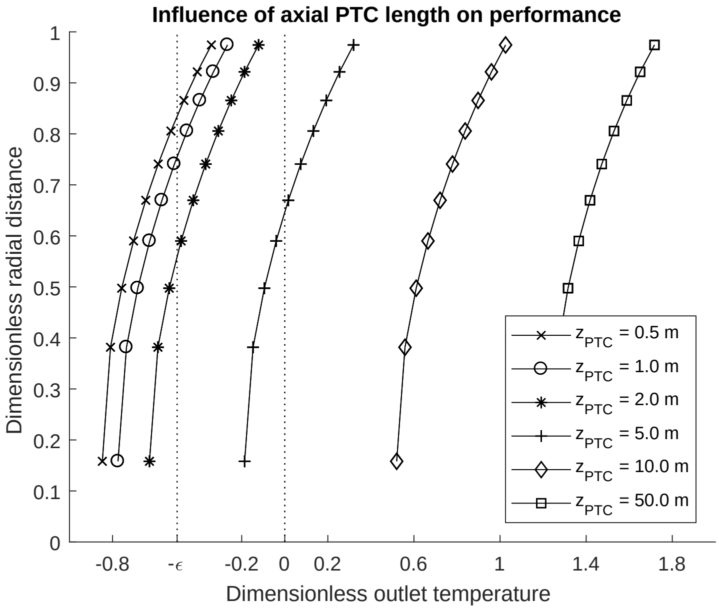

(b) Effect of varying the axial length of the PTC on the dimensionless outlet temperature.

Figure 3.16: Effect of varying the residence time of the PCS on the dimensionless outlet temperature. The remaining parameters have been kept constant at Φ_p = 0.25, R_p = 400 × 10^{-7} m, R_p/R_{PTC} = 0.04 and Φ_{PCM} = 0.70. The sensitivity analysis of u_{mean} = 1.0 m/s and u_{mean} = 2.0 m/s has been performed at Δt = 0.01 s to allow for a stable simulation.

From Figure 3.16b it has been found that a longer pipe results in a higher dimensionless outlet temperature due to the increase in received solar irradiance. At a lower mean flow velocity the PCS spends more time in the PTC and therefore receives more heat flux before it leaves the PTC. The residence time of the PCS in the PTC is equal to the axial length divided by the mean flow velocity. Thus decreasing the axial length from 2.0 m to 1.0 m has the same influence on the residence time as decreasing the mean flow velocity from 0.1 m/s to 0.05 m/s. Above mean flow velocities of 0.5 m/s there is almost no difference in the dimensionless outlet temperature. To test for consistency also a sensitivity analysis for 2.0 m/s has been performed. This analysis proved that above a mean flow velocity of 0.5 m/s there is almost no change in dimensionless outlet temperature.

An increase in encapsulation volumetric fraction decreases the ability of a PCM particle to store latent heat as the effective heat of fusion of a PCM particle decreases with an increase in encapsulation volumetric fraction. There however is an increase in thermal conductivity present in the PCM particle resulting in better penetration of heat in radial direction. In Figure 3.17 it is seen that a larger volumetric PCM concentration results in a lower dimensionless outlet temperature. The decrease in thermal conductivity in the PCS with an increase in the volumetric PCM concentration is also clearly visible. At low volumetric PCM concentrations the gradient of the dimensionless outlet temperature is slightly steeper, showing a better penetration of the heat into the pipe.

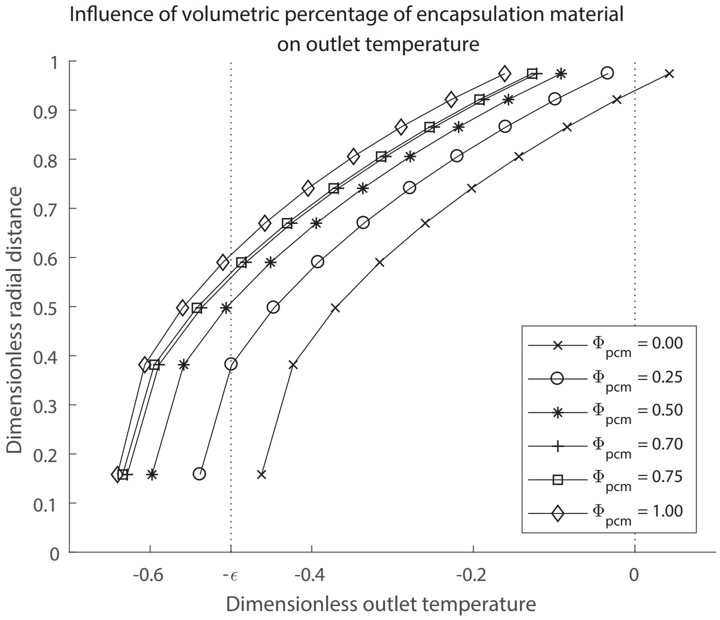

Figure 3.17: Effect of varying the volumetric PCM concentration on the dimensionless outlet temperature. The remaining parameters have been kept constant at Φ_p = 0.25, R_p = 400 × 10^{-7} m, R_p/R_{PTC} = 0.04 u_{mean} = 0.1 m/s and z_{PTC} = 2.0 m.

A change in the amount of heat of fusion per kilogram results in a change of the amount of latent heat that can be stored in the system, changing the value of the Stefan number. Varying of phase change temperature range only has influence on the temperature at which the PCM particles start to melt. Changing the incoming solar irradiance has influence on the amount of energy that enters the system.

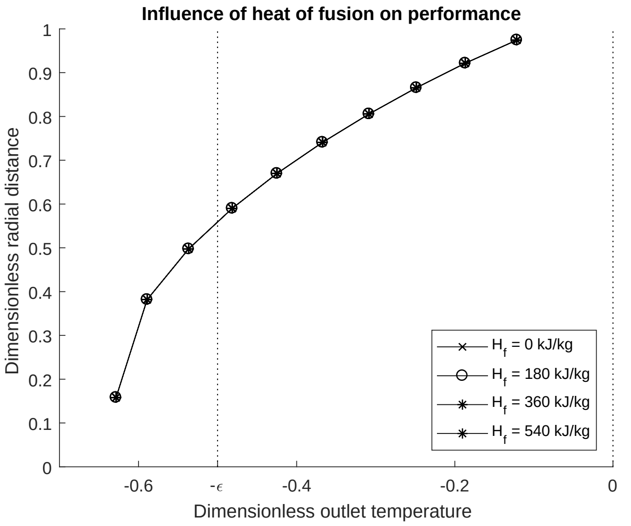

(a) Effect of varying the heat of fusion on the dimensionless outlet temperature. The data points of all the data sets are superimposed.

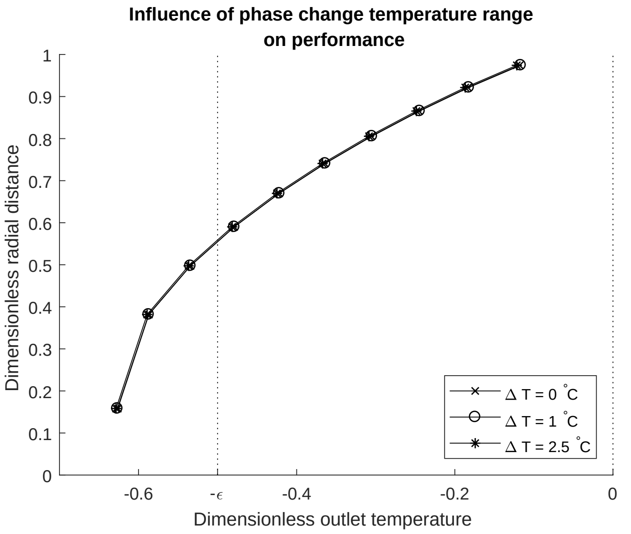

(b) Effect of varying the phase change temperature range on the dimensionless outlet temperature. The data points of all the data sets are superimposed.

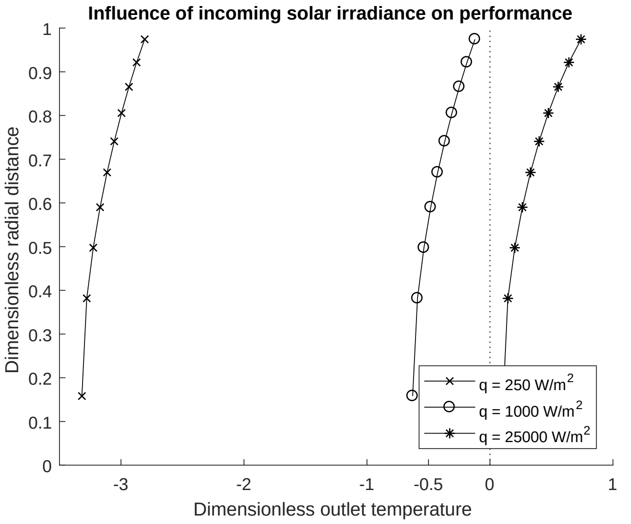

(c) Effect of varying the incoming solar irradiance on the dimensionless outlet temperature.

Figure 3.18: Effect of varying the properties of the PCM on the dimensionless outlet temperature. The remaining parameters have been kept constant at Φ_p = 0.25, R_p = 400 × 10^{-7} m, R_p/R_{PTC} = 0.04 u_{mean} = 0.1 m/s, z_{PTC} = 2.0 m and Φ_{pcm} = 0.70 .

Both a change in heat of fusion and change in phase change temperature range have no influence on the steady state as is found in Figure 3.18a and Figure 3.18b. The lines in these plots overlap perfectly. A lower heat of fusion does result in less time required for the system to reach steady state as less energy is required to reach the temperature at steady state due to the lack of potential latent heat storage. However the extra time required to reach steady state is smaller than expected due to the increase in the heat transfer coefficient because of the implementation of apparent heat capacity.
For a change in ΔT steady state is achieved after the same time duration. The same potential latent heat storage is present in the system but it is utilized at a later time step for a smaller phase change temperature range. From this analysis it is stated that supercooling has little effect on the thermal performance of the system as the temperature at which the phase change starts and ends has no influence on the performance of the system. Less incoming solar irradiance results in a lower dimensionless outlet temperature as depicted in Figure 3.18c. No sizing has been performed regarding the incoming heat flux as this parameter can not be controlled.

The numerical parameters, grid size and time step, influence the time that is required to reach steady state in the system. A finer grid or a smaller time step should result in less time required to reach steady state in the system. The temperature at the wall at the outlet of the PTC has been analyzed over time to check the influence of these parameters. This control volume has been chosen as the temperature in this cell has the largest increment in temperature. The influence of a finer grid is found in Figure 3.19a and Figure 3.19b. A finer grid in the axial length only influences the time required to come to a steady state while a finer grid in radial direction results in a steady state at a lower outlet temperature. A finer time step results in a faster steady state of the system. Decreasing the time step from 0.1 s to 0.01 s results in achieving steady state 25% faster, in 15 s instead of 20 s.

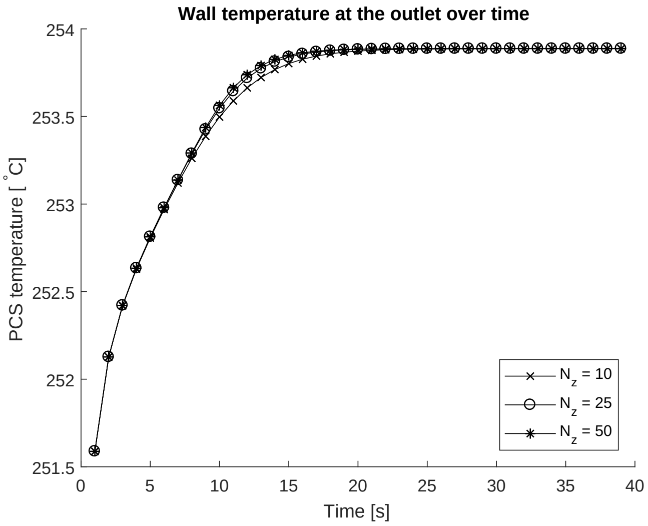

(a) Effect of a finer grid in axial length on the time it takes to reach steady state in the system.

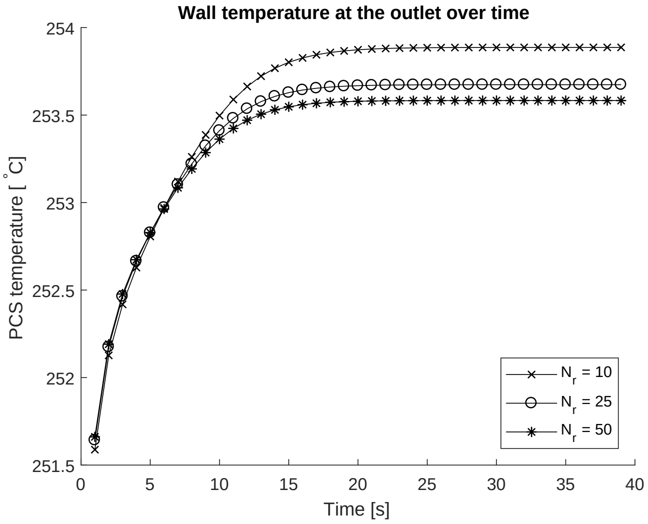

(b) Effect of a finer grid in radial dimension on the time it takes to reach steady state in the system.

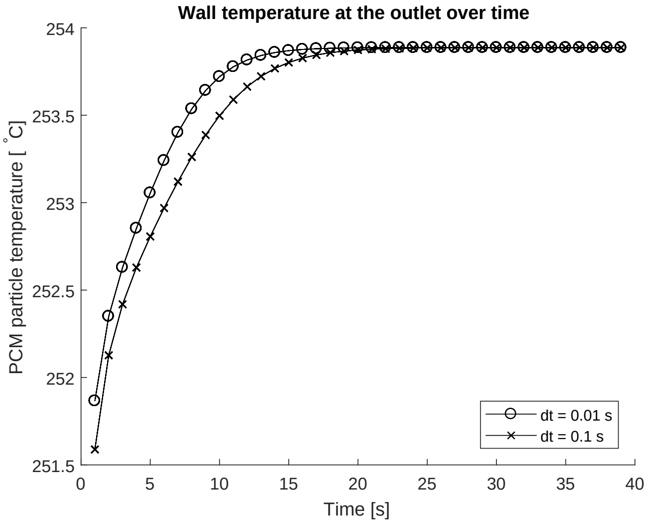

(c) Effect of a finer time step on the time it takes to reach steady state in the system.

Figure 3.19: Effect of the fineness of the grid and the time step on the time it takes to reach steady state in the system. The remaining parameters have been kept constant at Φ_p = 0.25, R_p = 400 × 10^{-7} m, R_p/R_{PTC} = 0.04 u_{mean} = 0.1 m/s, z_{PTC} = 2.0 m and Φ_{pcm} = 0.70.

Last the inlet temperature has been varied. The inlet temperature is also equal to the starting temperature in the PTC. A higher starting temperature results in a higher outlet temperature at steady state as less heat is required to raise the temperature to the melting temperature as seen in Figure 3.20. The sensible heat required for the system to be able to store latent heat is decreased for a higher inlet temperature. Although a lower inlet temperature results in a lower dimensionless outlet temperature a too low inlet temperature results in the latent heat storage capability to not be used at all, which is undesirable.

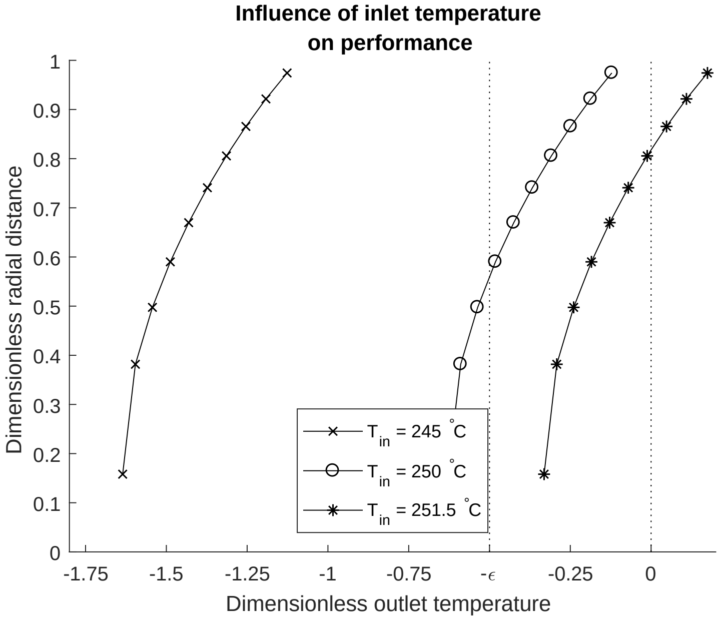

Figure 3.20: Effect of varying the inlet temperature on the dimensionless outlet temperature. The parameters have been kept constant at Φ_p = 0.25, R_p = 400 × 10^{-7}, R_p/R_{PTC} = 0.04 u_{mean} = 0.1 m/s, z_{PTC} = 2.0 m and Φ_{pcm} = 0.70.

A quantitative analysis has been performed to analyze the change in latent and sensible heat at steady state between the inlet of the PTC and the outlet of the PTC. The results of this analysis are present in Table 3.2. For every parameter that has been varied the fraction of the change in heat that is present as latent heat is given. A large fraction means that most of the energy is stored as latent heat, which results in a preferable performance. If this ratio is low it means that either the temperature does not reach the melting temperature of the PCM or overheating takes place, all PCM is already melted but more heat is present which is stored as sensible heat.

The average melt fraction displays which of these two cases is present. An average melt fraction of 1 means that all the PCM at the outlet has melted. A low average melt fraction indicates that there is a possibility to store more latent heat in the system. A combination of a large latent heat to total heat ratio and a small average melt fraction indicates a good latent heat storage capability of a system. This is because there is already a lot of latent heat present with respect to sensible heat and this ratio will increase when all of the PCM melts, increasing the average melt fraction.

Table 3.2: The latent heat to total heat storage ratio and average melt fraction at the outlet of the PTC for the parameters tested in the sensitivity analysis. A large latent to total heat ratio in combination with a low average melt fraction indicates a preferable system because the capability to store latent heat is large in such a system.

Parameter	Unit	Value	Latent heat to total heat ratio at outlet	Average melt fraction at outlet
R_p	m	400×10^{-5}	0.665	0.227
		400×10^{-6}	0.873	0.500
		400×10^{-7}	0.859	0.269
		400×10^{-8}	0.944	0.003
		400×10^{-9}	-	-
R_p/R_{PTC}	-	0.01	0.906	0.566
		0.02	0.919	0.443
		0.04	0.859	0.269
		0.10	0.957	0.835
		0.20	0.913	1
Φ_p	vol%	0	0	0
		5.0	0.590	0.660
		10	0.776	0.583
		20	0.861	0.381
		25	0.859	0.269
u_{mean}	m/s	0.01	0.827	1
		0.10	0.859	0.269
		0.50	0.437	0.020
		1.0	0.126	0.003
z_{PTC}	m	1.0	0.753	0.109
		2.0	0.859	0.227
		5.0	0.954	0.905
		10	0.899	1
		50	0.839	1
Φ_{PCM}	vol%	0	0	0
		25	0.787	0.406
		50	0.844	0.313
		70	0.859	0.269
		100	0.837	0.166
T_{in}	$^{\circ}C$	245	0	0
		250	0.859	0.269
		251.5	0.990	0.746
ΔT	$^{\circ}C$	0.0	0.860	0.273
		1.0	0.861	0.274
		2.5	0.859	0.269
H_f	kJ/kg	0.0	0	0
		180	0.752	0.269
		360	0.859	0.269
		540	0.901	0.269
q	W/m^2	250	0	0
		1000	0.859	0.269
		25000	0.446	1

Various trends are found from Table 3.2. It has been found that a small particle radius allows for better latent heat storage. This is due to the fact that the radius of the PTC scales down as well and it allows the particles at the center of the pipe to melt. Next to that small particles are fully molten while large particles might show a solid core while the wall is completely in liquid phase.

The particle to pipe radius ratio shows a minimum between a ratio of 0.02 and 0.10. At a small ratio the pipe radius is increased, resulting in more incoming heat flux and the particles at the wall are completely molten while the particles at the center of the PTC remain completely solid. When the ratio is large the heat penetration is better, resulting in particles starting to melt at the center. However the particles at the wall are not completely in liquid phase due to a lower incoming heat flux. A ratio of 0.04 shows an optimum between these extremes.

A larger volumetric PCM concentration, larger volumetric particle concentration and larger heat of fusion all show a positive trend for the amount of heat that is stored as latent heat due to the larger potential for latent heat storage. A larger inlet temperature also is beneficial as the sensible heat that is required before the melting temperature and therewith the possibility to store heat as latent heat is reached is lowered.

The trend that is displayed for the potential of latent heat storage by the mean flow velocity, incoming heat flux and the axial distance shows that the influence of these parameters is largely dependent on the other parameters in the system as these determine whether the residence time is too short, resulting in the PCM particles not melting sufficiently, or too long, resulting in overheating, therewith decreasing the ratio between the latent and sensible heat, of the PCS. When the other parameters have been picked these parameters should be varied to find the optimal performance of the PTC.

The phase change temperature difference exhibits no influence on the potential latent heat storage in the system, the small deviation is attributed to uncertainty in the calculation.

Concluding the sensitivity analysis a final sizing has been made which is believed to provide the optimal performance. The grid size and time step have been chosen to take on the finest option, resulting in a 50x50x50 grid and a time step of 0.1 s. While a finer grid and smaller time step might be beneficial these have not been considered due to the limit of computational power available.

The inlet temperature has been set to 251.5 °C so no initial sensible heating is required to reach the melting phase. The volumetric particle concentration is desirable to be large as the possible latent heat storage is large as well. As a PCS with more than 0.25 volumetric particle concentration start to behave non-Newtonian this is considered to be the largest possible volumetric particle concentration. The volumetric PCM concentration can be viewed in a similar matter. A large volumetric concentration for PCM in the particle is desirable but from experimental data it has been found that a concentration above 0.7 may result in an unstable particle as no case of shape-stabilized phase change particle is known with a lower volumetric concentration of encapsulation [10]. Therefore the volumetric PCM concentration in a particle is kept at 0.7. The mean flow velocity is set at 0.5 m/s. A larger mean flow velocity does not improve the performance of the PTC significantly while the pump power required to attain this mean flow velocity will increase considerably.

To accommodate for better latent heat storage the axial length of the PTC has been increased to 5.0 m for an increase in residence time. The particle size has been established to equal 400×10^{-8} m and the particle to pipe radius ratio is fixed at 0.04. These values have been summarized in Table 3.3.

Table 3.3: Parameters and the values that are considered to deliver the optimal performance for the modeled system.

Parameter	**Final value**
R_p	400×10^{-8} m
R_{HEX}	1×10^{-4} m
R_p/R_{PTC}	0.04
Φ_p	25 vol%
u_{mean}	0.50 m/s
z_{PTC}	5.0 m
Φ_{PCM}	70 vol%
Δt	0.01 s
T_{in}	251.5 °C
N_z	50
N_r	50
N_{r_p}	50

3.7. Verification and validation

Verification is provided on four of the provided assumptions as stated in Section 3.4.1. It has been checked if the assumptions that have been made are justified. If these assumptions are not justified, alterations that have to be made to the numerical PCS model are provided. To check if the PCS model is a realistic representation a validation has been performed. In this validation the results from the PCS model have been compared to experimental data of an experimental set-up with similar purpose.

For the governing equation of the PCS the assumption has been made that conduction in axial direction is a lot smaller than the forced convection term and therefore can not be neglected. This assumption is satisfied when the Peclet numbers are large. Peclet numbers in the range of 25 to 2500 are present in the system, this is large enough to justify the neglection of conduction in axial direction [7].

The volumetric particle concentration and particle radius have been kept at a constant value throughout the experiment, while the density changes with phase. In the operating range between the starting value of 251.5 °C and 260 °C the density of the particle varies between 1776 kg/m^3 in solid phase to 1618 kg/m^3 in liquid phase at 260 °C. The change in particle density is smaller than the change in density of the PCM as the density of the encapsulation, making up 30 vol% of the particle, hardly changes. When the mass of a particle is considered to remain equal the change in volume and radius of the particle can be determined. The volume of a particle changes from 8.53×10^{-17} m^3 to 9.36×10^{-17} m^3, an increase of roughly 9 percent. At a volumetric concentration of 0.25 it would result in an increase to a volumetric particle concentration of 0.27 as the density of the HTF remains almost constant. Even though this increase seems negligible, the PCS now has properties in the range at which it is considered to exhibit non-Newtonian behaviour. Therefore the volumetric particle concentration is limited to 0.23 at start conditions to be on the safe side and ensure that the region in which non-Newtonian behaviour occurs is not reached at the upper range of the operating temperature. The particle radius increases from 4.0 μm to 4.1 μm and therefore the assumption that the particle radius is kept constant is valid.

It has been stated that the particles are considered to be isotropic, having equal thermodynamic properties throughout an entire particle. This can be verified by checking the discrepancy between the inner and outer cell of the particle. It is found that the temperature change within a particle is minimal and therefore this assumption is true. Figure 3.21 depicts the temperature distribution at steady state in a particle modeled with a radius of 40 µm consisting of 50 control volumes. The difference between the temperature in the particle core and at the particle wall is minimal.

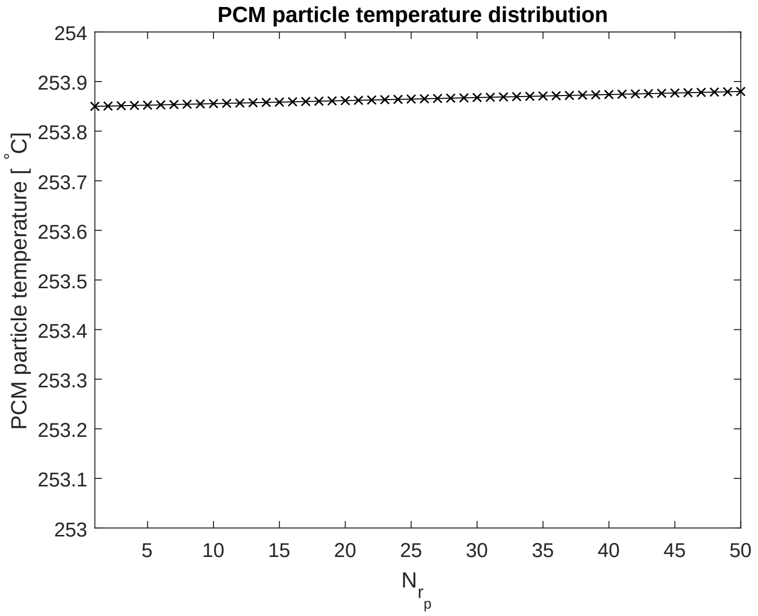

Figure 3.21: Temperature distribution in a PCM particle of 40 µm at steady state modeled with 50 control volumes.

In the assumption it has been stated that all the particles in a control volume have the same properties attributed to them. To see if this assumption is justified the temperature increment between control volumes has been checked. A particle that is present at the boundary between two control volumes has in reality the average properties of these two control volumes. From the model it has been found that the largest increment in temperature is equal to 0.01 °C. This increment is negligible and therefore the assumption is justified. With a less fine grid this assumption needs to be re-evaluated.

The model has been validated using the experimental data from Goel et al. [22]. The range at which this experiment has taken place lies outside of the scope of the tested PCS model as the mean flow velocity is a factor 10 larger than the values tested in the sensitivity analysis. However since it is the only experiment with similar dimensions for the set-up an attempt to validate the PCS model has been made. Goel et al. worked with a PCS based on water, urea-formaldehyde and n-eicosane and have tested the influence of adding PCM particles to a HTF on the wall temperature. To be able to validate the PCS model the materials have been adjusted to the materials used by Goel et al. and the dimensions of the PTC have been altered to represent the experimental set-up. The thermophysical properties of the materials used in the experiment have been provided in Table 3.4. Data for the encapsulation material could not be obtained from the referenced source and is taken to be constant at the values provided by Goel et al. The thermophysicial properties for the PCM have been taken to be constant while in solid or liquid phase, with a linear variation between these values for the melting phase. The properties as a function of temperature of water have been evaluated using the thermophysical properties provided in Table A.5 and their respective fits. Experimental data have been obtained by Goel for volumetric particle concentrations from 0.05 to 0.1, particle diameters of both 100 µm, 250 µm and a mix of these two sizes and Reynolds numbers of 200 and 1000.

Table 3.4: Thermophysical properties of n-eicosane, urea deformaldehyde and water at an operating temperature of 37 °C as used by Goel et al.

Material	T_m **[**$^{\circ}C$**]**	H_f **[**kJ/kg**]**	ρ_s **[**kg/m^3**]**	ρ_l **[**kg/m^3**]**	cp_s **[**$kJ/kg^{\circ}C$**]**	cp_l **[**$kJ/kg^{\circ}C$**]**	λ_s **[**$W/m^{\circ}C$**]**	λ_l **[**$W/m^{\circ}C$**]**	μ **[**$mPas$**]**
n-eicosane ($C_{20}H_{42}$) [26]	37	247	856	778	2.21	2.01	-	0.15	5.25×10^{-8}
Urea-formaldehyde ($[(O)CNCH_2]_n$)			1500		1.67		0.42		
Water	100			997		4.18		0.606	9.07×10^{-7}

The heat flux that has been used in the experiment is a function of the Stefan number, which is defined as Equation (3.40) by Goel et al.. The Stefan number for each performed experiment has been provided. By rewriting Equation (3.40) the constant heat flux for the experiment has been calculated. The mean flow velocity has been deducted from the Reynolds number. The dimensions of the experimental set-up have been provided in Table 3.5. The validation has been performed using a coarse grid to limit the required computational power.

$$Ste = \frac{cp_{PCS}(qR_{HEX}/\lambda_{PCS})}{\Phi_p H_f(\rho_p/\rho_{PCS})} \tag{3.40}$$

Table 3.5: Dimensions of the experimental set-up as used by Goel et al. [22].

Parameter	**Value**
Inner diameter	3.14×10^{-3} m
Outer diameter	4.76×10^{-3} m
Axial length	0.3 m
Φ_{PCM}	0.803

Three cases that have been treated by Goel have been studied in the validation. These three cases have been selected to allow for a good spread in the range of values that have been assessed in the experiment. The parameters and the values that are subject to these cases have been provided in Table 3.6.

Table 3.6: Overview of variables and their value for the three cases that have been used to try to validate the PCS model.

Case number	R_p **[**μm**]**	Re	Ste	Φ_p
1	50	200	1	0.1
2	125	200	1	0.05
3	125	1000	1	0.05

The dimensionless temperature and dimensionless axial distance for the validation have been defined according to Equation (3.41a) and Equation (3.41b). In the experiment the temperature has been measured for one minute and then the wall temperature has been averaged over the measured values during that time span. This has also been applied to the temperature values obtained by the PCS model. The comparison of the experimental data and the results obtained by the PCS model for the three cases is found in Figure 3.22, Figure 3.23 and Figure 3.24.

$$\theta_w - \theta_{in} = \frac{T_w - T_{in}}{(qR_{HEX}/\lambda_{PCS})} \qquad (3.41a) \qquad\qquad X = \frac{x}{R_{HEX}RePr} \qquad (3.41b)$$

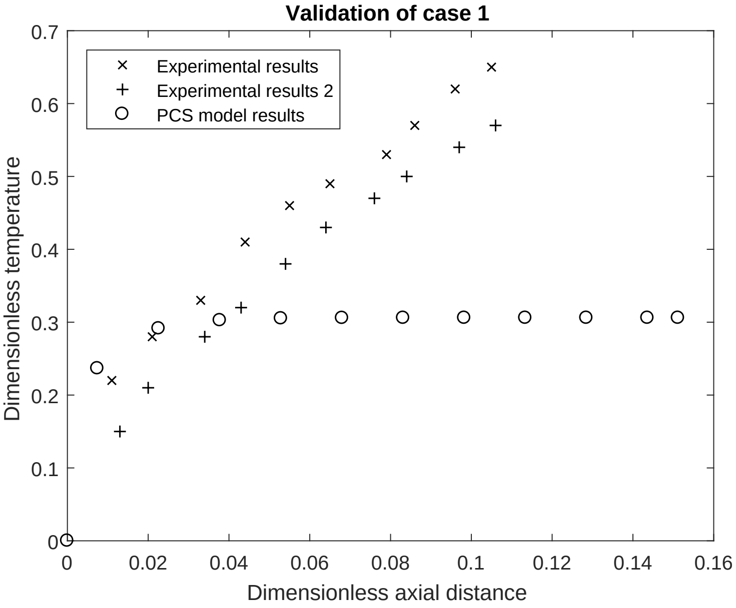

Figure 3.22: Comparison of the experimental data and the results obtained for the PCS model for case 1.

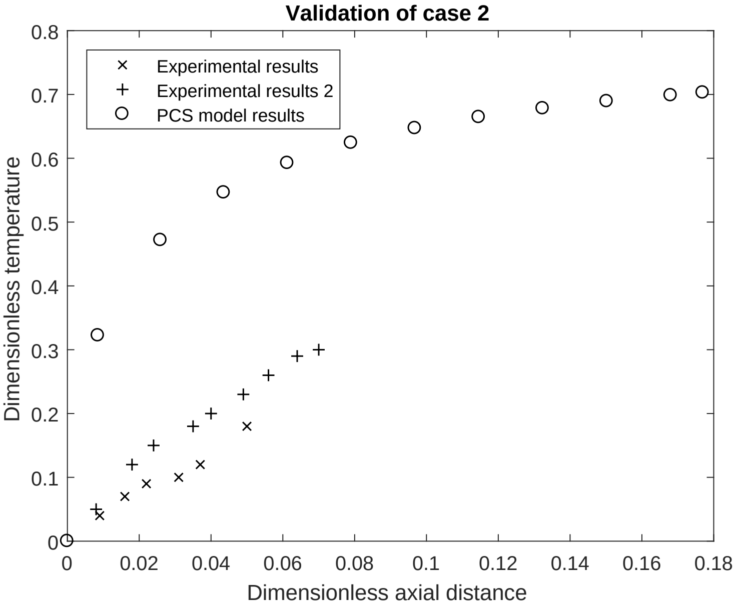

Figure 3.23: Comparison of the experimental data and the results obtained for the PCS model for case 2.

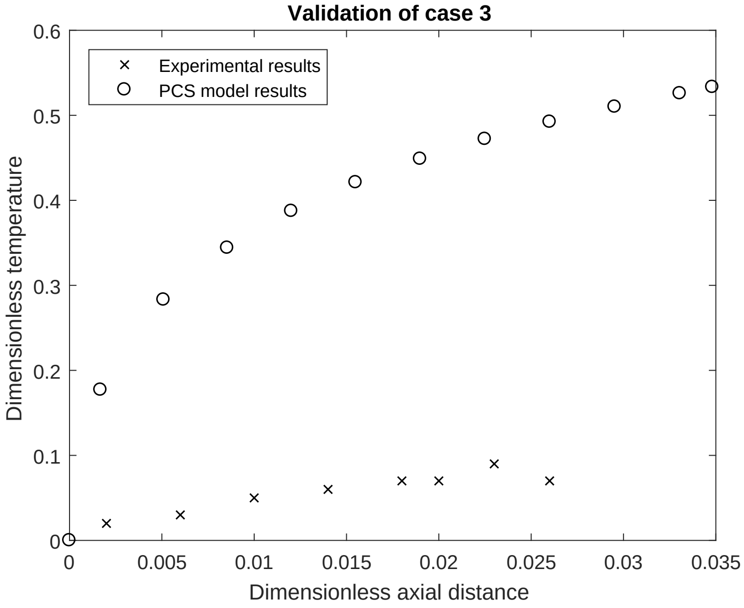

Figure 3.24: Comparison of the experimental data and the results obtained for the PCS model for case 3.

Some difference in values between the experimental data and the results obtained by the PCS model have been found. The results of the experiment also show variance among different tests at the same conditions. In the first case it is seen that the results from the PCS model show a lower outlet temperature. A difference of 86% and 123 % is present between the experimental data and the data obtained with the PCS model. Next to that there is no indication of a steady state in the experimental set-up, which is present in the numerical data, thus when the pipe in the experiment would have been larger an even greater difference could be present. For case 2 and case 3 there are signs that steady state has been achieved in the experiment but the outlet temperature for the PCS model is higher. For case 2 the experimental data is 75% and 56% lower. In case 3 the experimental data is even 87% lower. Five reasons have been suggested for these discrepancies.

First of all the thermophysical properties that have been used for the PCS model are not complete. Next to that the PCS model assumes an ideal version of supercooling in which all PCM particles melt over the same range, this range varies for each PCM particle in reality. They are however expected to have a very small influence on the results. Another small influence is the method used to collect the experimental data. As the experimental results have not been tabulated the data had to be read from plots, which is not an accurate method for obtaining data.

Next to that in the PCS model it has been assumed that the PCS enters the PTC at the melting temperature. For the experimental data is has been found that this was aimed for, but not achieved for most of the experimental tests, resulting in a lower wall temperature as some of the heat is required for raising the temperature of the PCS to the melting temperature. Another reason why the outlet temperature in case 2 and 3 might be higher is due to the fact that no pipe has been modeled in the PCS model while in the experiment heat is also required to heat up the pipe.

Lastly the most important reason why the experimental data and the results from the PCS model do not show a good match is due to the assumption that the PCM particles are evenly distributed in the PCS. Charunyakorn et al. [5] have made a numerical model of a PCS with this same assumption and his numerical data has been compared to the experimental results of Goel et al., which show discrepancies of up to 45%. In the experiment it has been stated that due to buoyancy effects the particles do not have an even distribution. What has been stated as buoyancy effect might be defined as the tubular pinch effect that is present in dilute suspensions, an effect that causes the particles to concentrate themselves just outside of the center of the cross section of the pipe. It has been shown that in particle suspensions a stable radial position is not obtained at the center of a pipe, but rather at about 0.6 of the tube radius [51]. However, the same performance for a non-buoyant suspension was found and thereby stated that the homogeneity of the particle distribution does not influence the performance of a PCS as stated by Goel et al.. Amani et al. contradict this claim and found that a heterogeneous distribution of particles caused better heat transfer at the edge, resulting in a lower wall temperature [1].

3.8. Conclusion

In the sensitivity analysis executed as provided in Section 3.6 the influence of physical and numerical parameters on the performance of the system have been examined. A good performance has been defined as a large ratio of latent heat to sensible heat in the outlet of the PTC. The effects these parameters have on the performance of the PTC when they increase in value have been summarized in Table 3.7. Each effect has been defined as either a positive or a negative effect on the performance of the PTC.

Table 3.7: Parameters that influence the performance of the PTC and their effect on the performance. The positive and negative effects on the performance of a PCS that occur when a parameter increases have been provided.

Parameter	**Positive effect**	**Negative effect**
R_p	Higher heat transfer coefficient Smaller dimensionless time step	Slower melting of particles
R_{HEX}	Larger surface area Larger PCS Peclet number and smaller dimensionless time step	Less heat transferred to center of pipe
R_p/R_{PTC}	Larger particle Peclet number resulting in larger effective conductivity	Lower surface area for heat flux
Φ_p	Increase in latent heat in the system Better heat transfer between PCS and PCM particles	Higher dynamic viscosity
u_{mean}	Increase in effective thermal conductivity	Shorter residence time to take up heat
z_{PTC}	Longer residence time to take up heat	Increase in sensible heat in the system
Φ_{PCM}	Increase in latent heat in the system	Decrease in thermal conductivity of PCS
H_f	Better heat transfer inside the PTC	Increase in latent heat in the system

Following the sensitivity analysis and the verification and validation the final dimensions have been determined. With respect to Table 3.3 only the volumetric particle concentration has been altered to 0.23, according to the result of the verification. In Figure 3.25a to Figure 3.25e the temperature distribution of the PCS in the PTC has been described. Due to the small radial dimension of the PTC steady state was achieved in 10 s. The wall heats up due to the incoming heat flux and the heat is then transported to the center of the PTC. The outlet temperature at the center of the PTC is 256.0 °C, so the melting temperature has been reached in the entire radial dimension. Due to the small time step that has been implemented the difference in temperature between the PCS and the PCM particles is negligible. Next to that it is visible from Figure 3.25e that the melting temperature is attained at an axial length of approximately 3 m. The PTC could thus have been shorter for a better performance. The solar radiation used for the sensitivity analysis is however larger than the average solar radiation in the Netherlands thus in reality less heat will be added to the system and the outlet temperature will be lower. Next to that no other axial lengths have been considered in the sensitivity analysis and their performance can not be predicted, thus the axial length that has been used for the comparison remains at 5.0 m. Unfortunately no experimental data have been found that resemble the range in which the numerical model has been tested. Experimental data outside of the tested range has been found and used to try to validate the numerical model but large discrepancies between the experimental data and data from the numerical model have been identified.

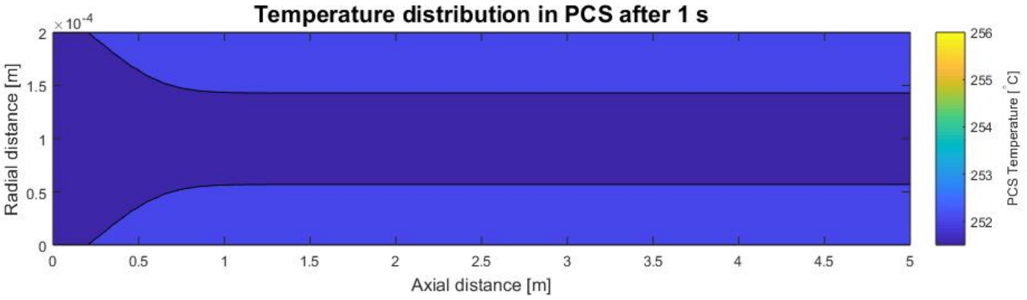

(a) Temperature distribution of the PCS in the PTC at 1 s.

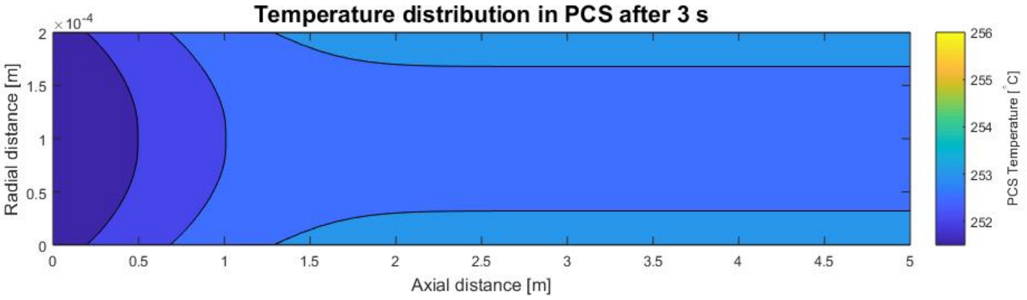

(b) Temperature distribution of the PCS in the PTC at 3 s.

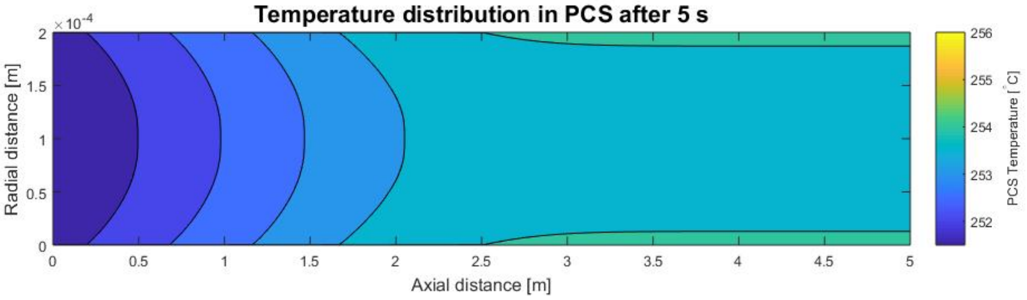

(c) Temperature distribution of the PCS in the PTC at 5 s.

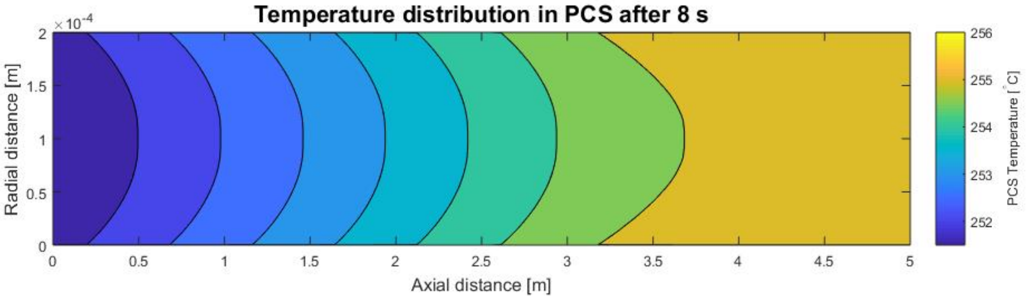

(d) Temperature distribution of the PCS in the PTC at 8 s.

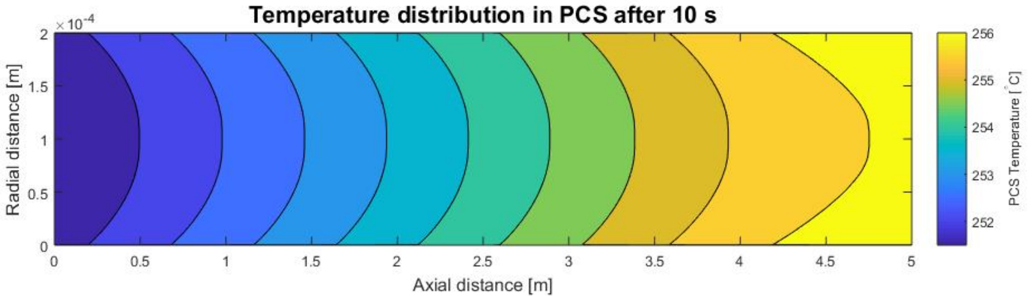

(e) Temperature distribution of the PCS in the PTC at 10 s. Steady state has been achieved at this time.

Figure 3.25: Temperature distribution of a PCS in a PTC with R_{HEX} = 1×10^{-4} m, R_p = 400×10^{-8} m, Φ_p=0.23, u_{mean} = 0.5 m/s, z_{PTC} = 5.0 m/s and Φ_{PCM} = 0.70 over time.

4

Comparison to shell and tube model

The goal of this study is to develop a model for a PCS and make a meaningful comparison to a system where the LHTES is incorporated in a S&T HEX. Fan has developed a numerical model that predicts the transient behaviour of such a system. The numerical model that Fan has built has been used together with the previously build PCS model to make a comparison between a LHTES system with a S&T HEX and a PCS system. This chapter provides the purpose of the comparison in Section 4.1, a brief description of the packed bed model as it has been designed by Fan in Section 4.2, alterations that have been made to the S&T packed bed model to come to a meaningful comparison in Section 4.3 and the case to make the comparison in Section 4.4. Finally the performance of the S&T packed bed model has been outlined in Section 4.5 and the conclusion of the comparison has been reported in Section 4.6. A more detailed description of the packed bed model is found in the thesis provided by Fan [17].

4.1. Purpose

The purpose of comparing the PCS model as described in Chapter 3 and the S&T model is to determine which type of system shows better heat storage and transportation performance under similar conditions. The system that shows the best performance can be expanded upon and more research regarding this system can be performed. To find out the best performing system performs the numerical models of the two systems have been compared.

4.2. Description of shell & tube of packed bed model

The objective of the original S&T packed bed model was to predict the transient performance of a S&T solid-liquid LHTES system which has been linked to a solar driven $\mathrm{H_2O/LiBr}$ double-effect absorption system for the cooling of office space and was utilized when excess solar flux was present in the system. The absorption system that has been designed to cool office space is not discussed because this part of the system is irrelevant for the comparison of the LHTES systems.

DowTherm A has been applied as a HTF in this model as it is a widely used HTF for solar applications. Hydroquinone has been favored for the S&T packed bed system as this material undergoes a small degree of supercooling compared to other considered PCMs. It is an organic PCM and has a melting point of 172 °C and a heat of fusion of 230 kJ/kg to 258 kJ/kg. To model the phase change region of the material the enthalpy formulation method has been applied. Section 2.5 offers a more detailed description on this type of phase change modeling.

The LHTES system of the S&T packed bed model is composed of S&Ts as depicted in Figure 4.1a. The HTF flows through the pipe while the PCM is located in a sequential pipe that envelops the pipe through which the HTF flows as illustrated in Figure 4.1b. A scaled down overview of the concentric tubes that contain the HTF and the PCM is presented in Figure 4.1c. The model that has been constructed by Fan is based on this scaled down system. One unit, defined as a S&T packed bed with multiple tubes, contains approximately 383 kg of PCM.

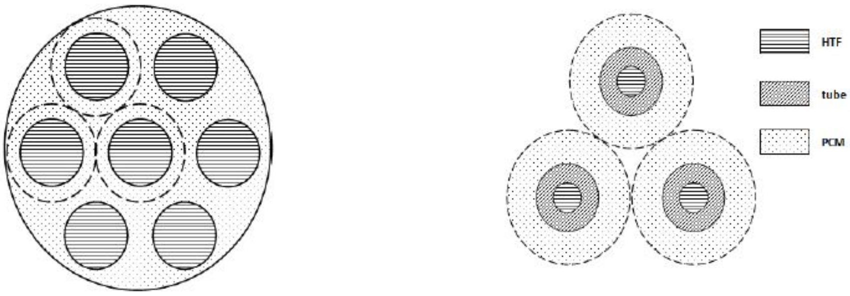

(a) LHTES unit including multiple pipes **(b)** A detail of a pipe

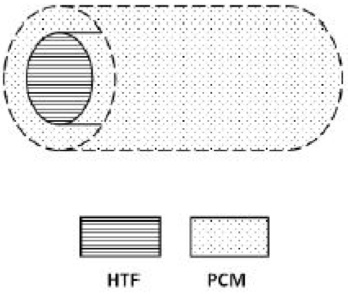

(c) Two concentric tubes system

Figure 4.1: A simplified representation of the LHTES system of the packed bed model as designed by Fan [17].

The following assumptions have been applied to the model:

- The PCM is homogeneous and isotropic. The properties are identical in all directions.
- Both temperature variations of the tube and the PCM in the angular direction are neglected.
- The thermophysical properties of the PCM are constant with temperature, but not with phase.
- The thermophysical properties of the tube are constant with temperature.
- The thermophysical properties of the HTF vary with temperature.
- The effect of natural convection of the PCM in the liquid phase is neglected.
- The system is well insulated, therefore it has no heat losses to the environment.

The governing equations of the model for the HTF and PCM have been given in Equation (4.1) and Equation (4.2) respectively. V is the inner volume of the tube, A is the inner surface of the tube, $\dot{m}$ is the mass flow of HTF through the tube and h is the convective heat transfer coefficient as provided in Equation (4.3). The tube wall has been neglected in the model for computational simplicity.

$$\rho_{HTF} cp_{HTF} V_{LHTES} \frac{\partial T_{HTF}}{\partial t} = \dot{m} cp_{HTF} \partial T_{HTF} - hA_{PTC}(T_{HTF} - T_{PTC}) \tag{4.1}$$

$$\frac{\partial H_{PCM}}{\partial t} = \frac{\partial}{\partial z}\left(\alpha_{PCM}\frac{\partial H_{PCM}}{\partial z}\right) + \frac{1}{r}\left(r\alpha_{PCM}\frac{\partial H_{PCM}}{\partial r}\right) \tag{4.2}$$

$$h = \frac{\lambda Nu}{2R_{PTC}} \tag{4.3}$$

The model is a quasi steady model as the thermophysical properties of the PCM are not a function of temperature and therefore only change when a phase change takes place. The phase of the PCM and its corresponding thermophysical properties are determined by the quantity of the enthalpy of the PCM. The PCM is in solid phase when the enthalpy satisfies the condition specified in Equation (4.4). When the prerequisite stated in Equation (4.5) is true then PCM is transitioning from a solid to a liquid phase or vice versa. When the condition specified in Equation (4.6) is met the PCM is completely in a liquid phase.

$$H_{PCM} < \rho_{s_{PCM}} cp_{s_{PCM}} T_{PCM} \tag{4.4}$$

$$\rho_{sPCM} cp_{s_{PCM}} (T_m - \Delta T) \leq H_{PCM} \leq \rho_{s_{PCM}} (cp_{s_{PCM}} (T_m - \Delta T) + H_f) \tag{4.5}$$

$$H_{PCM} > \rho_{s_{PCM}} (cp_{s_{PCM}} (T_m - \Delta T) + H_f) \tag{4.6}$$

An equidistant grid as described in Section 2.4.2 has been used in the model, dividing the tube into j cylindrical control volumes and i axial control volumes. The size of the control volumes has been chosen such that a control volume either contains only PCM or HTF but never both.

The LHTES system is attached to the high pressure generator of the absorption cycle in this model. The mass flow that goes into the high pressure generator is depending on the amount of cooling that is required in the office space. A part of the or the total HTF mass flow that flows through the PTC is rerouted to the LHTES system when excess solar flux is present, based on the amount of excess heat.

4.3. Alterations made to shell & tube packed bed model

To be able to make a fair comparison between the two models, parameters in the S&T model have been adjusted. The materials of the packed bed model have been changed to represent the materials as used in the PCS model. The HTF has been changed to represent MarloTherm SH and the PCM has been altered to display the properties of $\mathrm{LiNO_3}$. The S&T does not have the same limitations as the PCS therefore encapsulation is not required and has been omitted to allow for a larger energy density of the PCM. The thermophysical properties of the PCM have been altered to be a function of temperature and the starting temperatures of the model have been readjusted accordingly.

The size of the S&T packed bed model is reduced to the size of the PCS model. The number of units is reduced to one, as all units are expected to have the same performance, and the outer diameter of the pipes through which the HTF flows has been reduced to equal the outer diameter of the PTC in the numerical PCS model so that both systems receive the same amount of heat flux. The dimensions of the shell have been chosen such that the mass of the PCM is equal to the mass of the PCM present in PCS system. Any up scaling that has been done later in the comparison is performed by coupling parallel systems unless stated otherwise. Furthermore the grid size and the time step have been altered to be equal across both models.

The S&T model is integrated into a system including an absorption cooling system, therefore an analysis has been made to find which part of the model can be kept intact. The objective of the new system is to represent the melting of the PCM as in a S&T packed bed and replace the absorption cooling system in the original model by a HEX connected to the ORC. This has been done to ensure that the system used in the comparison is as close as possible to the original system.

The original system integration consists of five operations called ”switches” which permit the system to operate in a certain way. The operation of switch 3, as pictured in Figure 4.2, represents the operation that resembles the operation of the PCS system. When this switch is operated excess solar energy available in the system is used to melt the PCM in the LHTES. To ensure that all incoming solar energy is used for melting the PCM the mass flow to the high pressure generator is set to equal 0 kg/s. Instead a mass flow towards the HEX has been implemented that is based on the required load of the ORC. Next to that the mass flow through the collector has been determined according to the flow velocity as given in Equation (4.7). The mass flow is the driving factor in determining the PTC outlet temperature of the HTF, which has been assumed to be uniform across the radial dimension, as provided in Equation (4.8).

$$\dot{m}_{PTC} = \rho_{HTF} u_{mean} \pi R_{PTC}^2 \tag{4.7}$$

$$T_{PTC_{out}} = T_{PTC_{in}} + \frac{\dot{Q}_{PTC}}{\dot{m}_{PTC} cp_{HTF}} \tag{4.8}$$

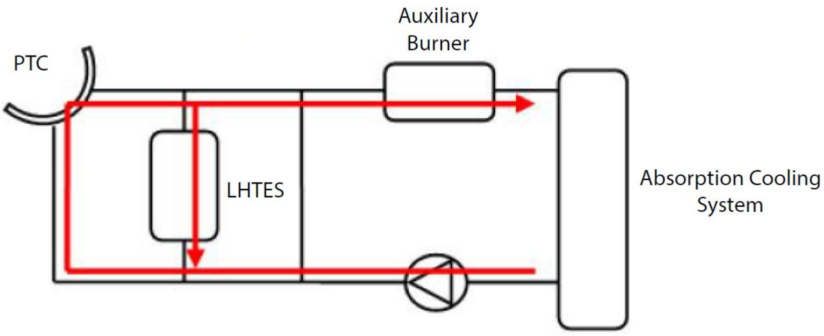

Figure 4.2: The operation mode when ”switch 3” is active. HTF is pumped through the solar collector and the excess heat is pumped through the S&T packed PCM bed.

The method to derive in which phase the PCM is present, as given in Equation (4.4) to Equation (4.6) has been adjusted to allow for temperature dependent thermophysical properties. Equation (4.5) has been altered to also represent the sensible heat required to account for the supercooling per Equation (4.9) and therefore Equation (4.6) has been adjusted to represent Equation (4.10) to account for the higher boundary at which the PCM is considered to be liquid. Once the enthalpy and its corresponding phase in a control volume has been determined a dummy value for the temperature is implemented. For this dummy value the thermophysical properties are determined and using these properties a new value for the temperature is iterated. This temperature is then checked for convergence. If convergence is not accomplished these steps are repeated until convergence has been achieved.

The PCM is melting if:

$$\rho_{PCM}(T_m-\Delta T)cp_{PCM}(T_m-\Delta T)(T_m-\Delta T) \leq H_{PCM} \leq \rho_{PCM}(T_m)(cp_{PCM}(T_m)T_m+H_f) \quad (4.9)$$

The PCM is in liquid phase if:

$$H_{PCM} \geq \rho_{PCM}(T_m)(cp_{PCM}(T_m)T_m+H_f) \quad (4.10)$$

The mass flow through the LHTES flows counter when the energy is depleted from the LHTES to maximize the heat that the HTF can take up from the LHTES.

Lastly the thermal efficiencies and the mechanical efficiencies of the used equipment have been omitted from both models to allow for faster computing. As these efficiencies are largely dependent on the equipment these cancel out in the comparison, assuming that similar equipment is used in both systems. An overview of the adjusted system of the S&T packed bed model is presented in Figure 4.3, the main difference with the PCS system is the location of the PCM. In the S&T packed bed system the PCM is only present in the storage vessel, while the PCM is present in the PCS in entire system for the PCS system.

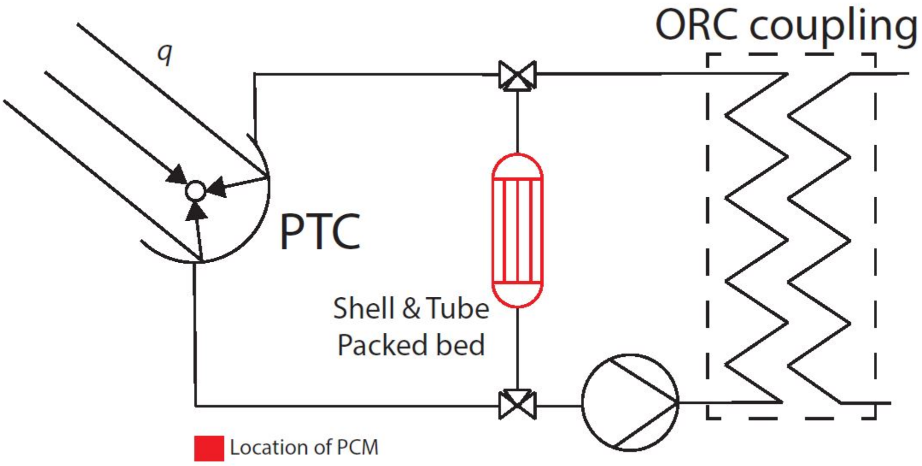

Figure 4.3: Process flow diagram of the updated S&T packed bed system with the location of the PCM indicated in red.

4.4. Test case for comparison

With the alterations made to the S&T model as described in Section 4.3 the comparison between the performances of the two models has been made. To make a comparison between these two systems it has to be acknowledged that the strength of these two systems is different. The PCS model is a system that excels in heat transportation. It takes up the heat produced by the incoming solar heat flux at the PTC and transports it in an efficient way to the HEX where the heat is released.

The PCM in the S&T model excels for storage. A HTF collects the incoming solar flux and transports it to the PCM packed bed where the heat is taken up by the PCM to be released at a later time when heat is required to supplement the stored heat from the incoming solar flux. The difference lies in the number of cycles that the PCM undergoes to melt and solidify again. In the PCS model the PCM undergoes many cycles at a small ΔT while the PCM in the S&T model experiences few cycles at a much larger ΔT.

To be able to make a comparison between these two systems a case has to be implemented in which the strong points of both systems is tested in a comparable set-up. For this set-up the analysis of the transient behaviour throughout a day has been selected for which the incoming solar irradiance varies on an hourly basis. This fluctuating input has an influence on the energy output that a system can deliver. Using a test case like this results in a known energy in- and output and the systems are designed to meet the heat demand of the ORC knowing these parameters. This case allows for testing both the performance of storage and transportation of heat.

Koninklijk Nederlands Meteorologisch Instituut (KNMI) only collects data regarding the global solar radiation, while a PTC is used to focus the direct radiation onto the PCS. To compensate for this the Photovoltaic Geographical Information System model[1] has been used to determine the direct solar radiation, based on averaged data from April at de Bilt. The direct solar radiation has been calculated on a 35° inclination plane and the hourly direct

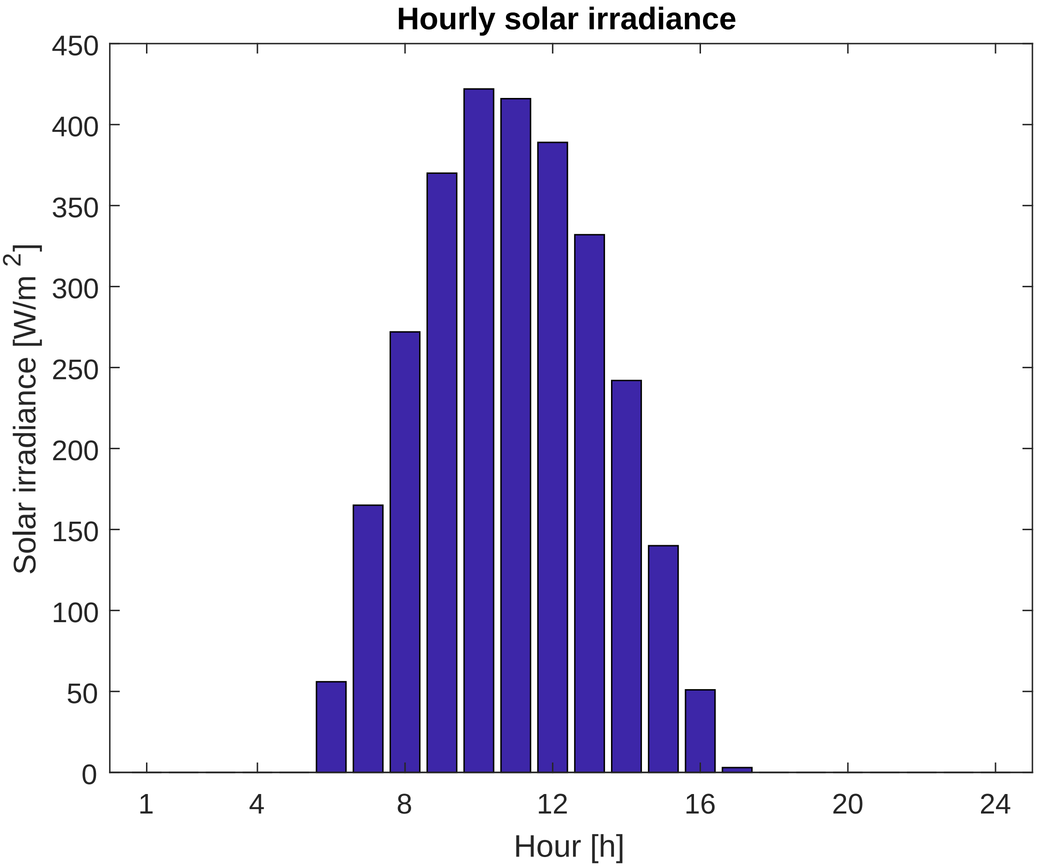

Figure 4.4: Hourly distribution of direct solar irradiance on a day in April as received by the PTC with an inclination plane of 35°.

A daily load case has been used to assess the performance of both systems. Statistics from Centraal Bureau voor de Statistiek (CBS) have been used to determine the base load of the district of de Bilt, which is the location where the solar irradiance has been measured. A household in de Bilt used on average 3320 kW h per year in 2015 according to CBS[2]. As the

---

[1] `http://re.jrc.ec.europa.eu/pvg_tools/en/tools.html`

[2] `https://staatvanutrecht.databank.nl/`

hourly variation of electricity demand is unknown it has been assumed that it is spread evenly across the day. This results in a base load of 0.379 kW per household. The system has been modeled for a block of 25 households, resulting in a requirement of a total base load of 9.5 kW.

If the simulation starts at midnight an infinite amount of units is required as there is no solar flux to meet the demand of the ORC. Therefore the simulation has been chosen arbitrarily to start at 11.00. This allows the system to collect excess heat and store it for the time when no incoming solar heat flux is present. This shifts the hourly solar irradiance curve as present in Figure 4.5.

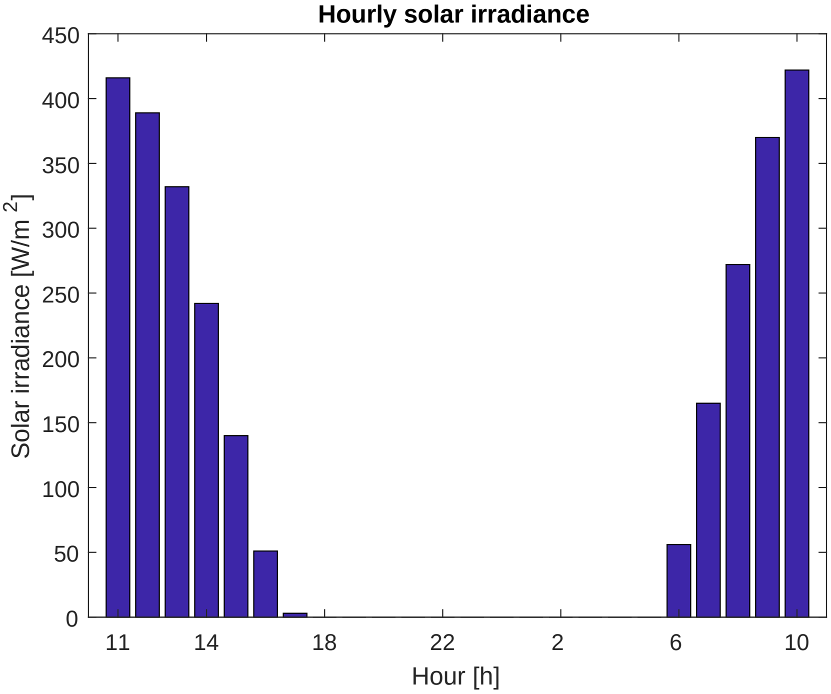

Figure 4.5: Chronological hourly solar irradiance that is received by the PTC as used in the test case.

It has to be taken into account that the efficiency of a modern ORC is relatively low at 20% [46]. Therefore the delivered heat to the ORC has to be a five fold of the specified demand, leading to a demand of 47.4 kW.

4.5. Performance and sizing based on test case

The number of units, the combination of a PTC and HEX to the ORC, that is required for each of the two systems has been determined based on this test case. The main difference in the heat transfer between the PTC and the HEX is that the S&T packed bed system takes up the heat flux with pure HTF, resulting in a higher outlet temperature in the PTC, while the PCS model has a lower average temperature due to the presence of PCM particles in the HTF. Next to that the HTF is pumped through the PCM bed which causes a non-uniform temperature distribution between the HTF and the PCM, contrary to the PCS model which does have a uniform temperature distribution between the HTF and the PCM. First the number of parallel units required for the PCS model to meet the demands of the test case has been calculated. Based on the sizing of the PCS model the total PCM mass in the S&T packed bed system and the total number of required parallel units for the S&T packed bed system has been determined.

4.5.1. PCS model

No sensitivity analysis has been performed on the performance of the HEX and no sizing has been acted out due to time constraints. Therefore the sizing of the PTC has been applied to the HEX as well. This ensures that all pipes have the same dimension. An overview of the system with parallel units is provided in Figure 4.6. A unit consists of a combination of a PTC and a HEX that is connected to the ORC. All units are connected to a storage vessel in which PCS is stored when excess solar radiation is present in the system. All excess heat is put into the storage to keep the inlet temperature of the PTC constant. The number of units is chosen such that no shortage of energy is present at any time in the system.

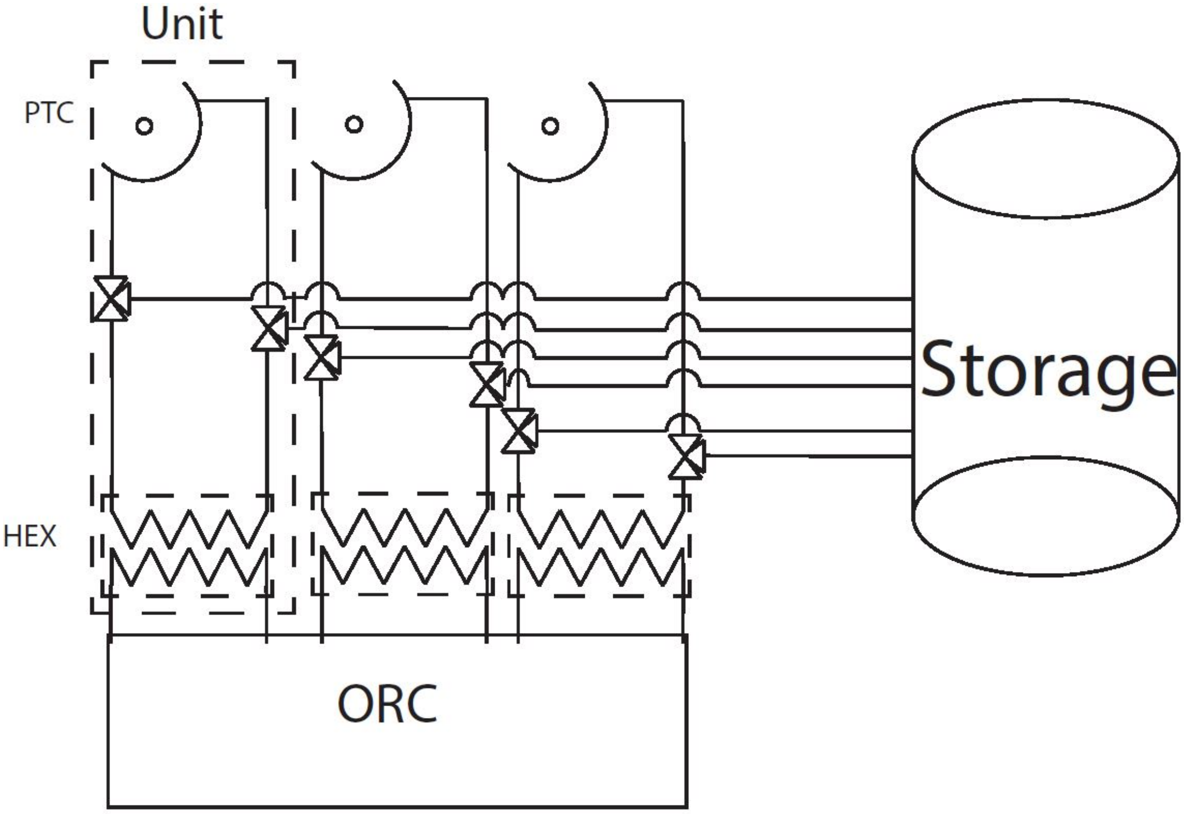

Figure 4.6: Overview of the PCS system with three parallel units. A unit consists of a PTC and a HEX that is connected to the ORC. All units are linked to the storage.

The outlet temperature of the HEX should not become lower than 251.5 °C, equal to the inlet temperature of the PTC. If the outlet temperature of the HEX drops below this temperature auxiliary heat is required to heat up the PCS before it enters the PTC, which lowers the efficiency of the system. To make sure that the outlet temperature does not drop below 251.5 °C the wall temperature has been set to equal 251.5 °C. When no radiation is present no PCS will be pumped to the PTC. If the outlet temperature of the HEX is higher than the inlet temperature of the PTC this heat is also stored to not waste it.

The heat that is transferred in the HEX to the ORC has been calculated by determining the change in total enthalpy between the inlet of the HEX and the outlet according to an enthalpy balance. The enthalpy has been determined by calculating the volumetric enthalpy of both the PCS as the PCM particles at the inlet and the outlet of the HEX. The calculation for the internal heat in the HTF is straight forward; the volumetric enthalpy at the inlet and outlet

have been calculated and have been subtracted to find the volumetric enthalpy change in the system according to Equation (4.11). The calculation for the change in volumetric enthalpy of the PCM particles is more complex. The change in volumetric enthalpy and heat of fusion for every particle control volume with volume V_{p_i} has been determined. The heat of fusion change in a particle is calculated by multiplying the possible volumetric heat of fusion with the melt fraction as given in Equation (4.12a) and Equation (4.12b). Based on the volumetric fraction of the control volumes the total change in enthalpy of a PCM particle has been determined as in Equation (4.13).
To find the total heat transfer rate to the ORC, $\dot{Q}$, the change in enthalpy of the PCM particle and the HTF have been added in proportion to their volumetric fraction and multiplied with the volumetric flow rate in the HEX as specified in Equation (4.14).

$$\Delta H_{HTF_i} = cp_{HTF_{in}i} T_{HTF_{in}i} - cp_{HTF_{out}i} T_{HTF_{out}i} \tag{4.11}$$

$$H_{f_{in_i}} = H_{f_{p_{in_i}}}(1 - x_{in_i}) \quad (4.12a) \qquad H_{f_{out_i}} = H_{f_{p_{out_i}}}(1 - x_{out_i}) \quad (4.12b)$$

$$\Delta H_{p_i} = \left(cp_{p_{in}i} T_{p_{in}i} + H_{f_{in}i} - cp_{p_{out}i} T_{p_{out}i} + H_{f_{out}i}\right) \frac{V_{p_i}}{V_p} \tag{4.13}$$

$$\dot{Q} = \sum (\Phi_p \Delta H_{p_i} + (1 - \Phi_p) \Delta H_{HTF_i}) u_i A_i \tag{4.14}$$

The heat transfer rate per hour per unit is provided in Table 4.1. During hours at which the hourly solar irradiance is large the heat transfer rate is also large as more heat is available in the system. As the time until steady state is small in comparison to the time at which the system is in steady state (a few seconds compared to one hour) the effect of the time up to steady state on the heat transfer rate has been neglected. The average energy that is transferred to the ORC per unit is 0.798 W. The ratio of outgoing energy per incoming solar flux is larger when the solar heat flux is large due to the contribution of the heat of fusion. For a higher solar flux the temperature at which steady state is achieved is high enough to allow for melting of the PCM particles, which results in an increase in volumetric energy density in the PCS. The equivalent number of units of PCS flow that go to the storage, the change in energy in the storage and the total energy that has been stored have also been provided.

Table 4.1: Hourly heat transfer rate per unit from the HEX to the ORC and the change in energy in the LHTES in the PCS system.

Time [h]	$\dot{Q}$ **[W]**	**Number of equivalent units of flow directly to storage**	**Change in energy in storage [kWh]**	**Total energy in storage at the end of hour [kWh]**
11	2.630	73 618	193.6	193.6
12	2.582	73 287	189.2	382.8
13	2.404	71 927	172.9	555.8
14	1.846	65 959	121.7	677.5
15	0.728	0	19.0	696.8
16	0.086	0	-39.5	657.3
17	0.004	0	-47.0	610.3
18	0	0	-47.4	562.9
19	0	0	-47.4	515.5
20	0	0	-47.4	468.1
21	0	0	-47.4	420.7
22	0	0	-47.4	373.3
23	0	0	-47.4	325.9
24	0	0	-47.4	278.5
1	0	0	-47.4	231.1
2	0	0	-47.4	183.7
3	0	0	-47.4	136.3
4	0	0	-47.4	88.9
5	0	0	-47.4	41.5
6	0.064	0	-41.5	0
7	1.307	55 368	72.4	72.4
8	2.203	70 122	154.4	226.8
9	2.617	73 533	192.5	419.3
10	2.680	73 958	198.2	617.5
Average	0.798	24 347		

The dimensions of the PTC have also been used for the HEX. The temperature distribution of the PCS in a HEX with $R_{HEX} = 1 \times 10^{-4}$ m and $z_{HEX} = 5.0$ m between 10.00 and 11.00 has been provided in Figure 4.7. This is the time slot at which the incoming solar irradiance is at its peak. For the peak incoming solar irradiance the heat that is taken up in the PTC and transported to the HEX is dissipated to the ORC over a short axial distance, no excess heat is present. Thus sizing is not beneficial for the thermal performance in this case, only for the costs of the system. As no excess heat is present at the outlet of the HEX any storage that is required has to come from an additional amount of units in the PCS system that are used to collect heat and store it in a storage vessel.

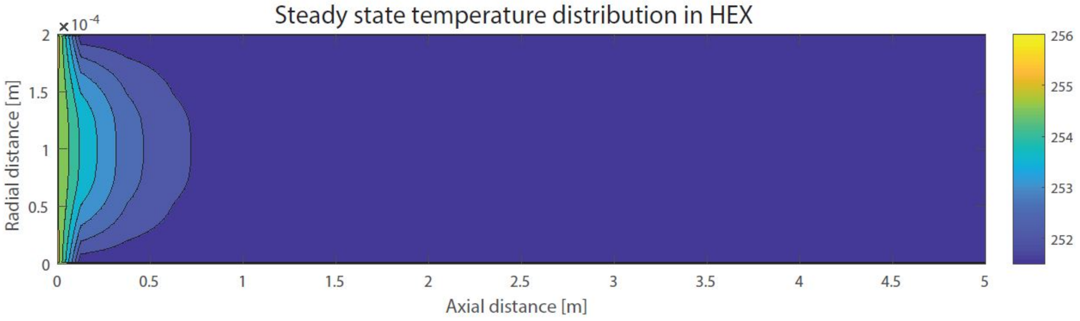

Figure 4.7: Temperature distribution of the PCS in the HEX with a wall temperature of 251.5 °C between 10.00 and 11.00.

Based on the demand of the test case and the available heat transfer rate, dependent on the available solar irradiance as presented in Table 4.1, the required number of parallel units has been calculated. The number of units have to allow for storage during the hours at which no solar irradiance is received by the PTC. A total number of 91 643 units are required to cover the demand of the ORC, including the required storage to meet the energy demand when no solar irradiance is present. The total heat present in the system is depicted in Figure 5.1. The heat stored is built up when excess heat is present in the PTC up to the maximum amount of heat that has to be stored that equals 697 kW h. At 07.00 the energy taken up in the PTC is supplemented by the energy that has been stored to fully deplete the storage.

The total mass of the PCM particles in the system has been calculated by calculating the mass of the PCM present in the total number of units and the total mass of the PCM that is required in the storage when the maximum amount of energy has been stored. Taking into account the dimension of one unit, the volumetric particle concentration and the volumetric PCM concentration of a particle it has been calculated that a total of 6.6×10^{-3} m^3 of PCM particles is present in the 91 643 units at all time using Equation (4.16). The encapsulation of the PCM contributes to the added mass of the particles and therefore has been counted in addition.

The mass of the PCM particles that is required for storage has been obtained by taking the amount of the PCM particles that is sent to the storage per hour up until the PCM is withdrawn from the storage to supplement the energy coming from the PTC. At 17.00 the maximum amount of PCM is present in the storage, with a volume flow equivalent to the flow through 311 431 units for one hour. The volume flow rate of a unit is multiplied with the number of units and the time to find the maximum volume of the PCM particles present in the storage, provided in Equation (4.17). This is equal to 4.05 m^3 of PCM particles present in the storage at the time when the maximum volume of PCM particles used for storage is achieved. The PCM particles mass that is required for storage is much larger than the mass of the PCM particles that are present in the flow in the system. The total volume of the PCM particles equals 4.06 m^3. The total volume of the PCM particles has been added and multiplied with the solid density of the particle, per Equation (4.15), to find the total mass of the PCM particles. The solid density of the PCM particle is 1621 kg/m^3. In the discussed PCS system the total mass of required PCM particles is 6575 kg.

$$m_p = \rho_{p_s}(V_{p_{PTC}} + V_{p_{HEX}} + V_{p_{LHTES}}) \tag{4.15}$$

$$V_{p_{PTC}} = V_{p_{HEX}} = N_{unit}\pi R_{HEX}^2 z_{HEX}\Phi_p \tag{4.16}$$

$$V_{p_{LHTES}} = N_{LHTES_{unit}} \pi R_{HEX}^2 u_{mean} t \Phi_p \tag{4.17}$$

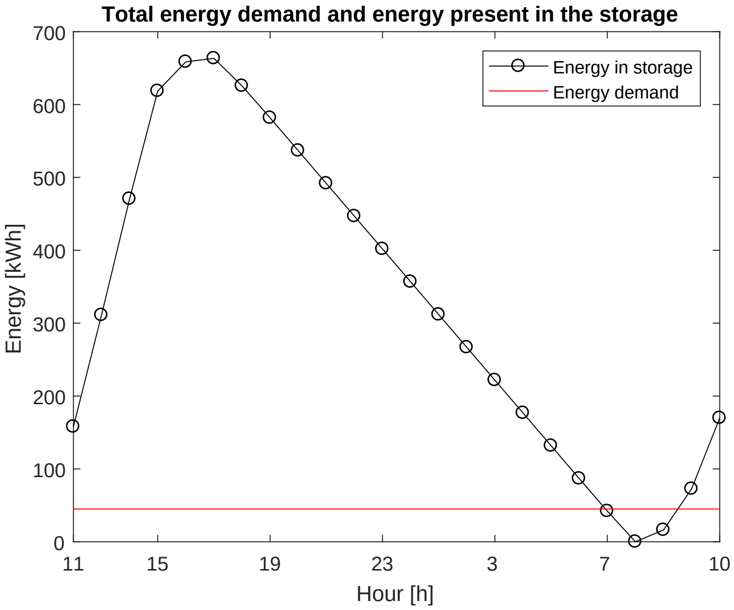

Figure 4.8: Total energy available in the storage of the pcs system compared to the energy demand throughout the day.

4.5.2. Shell and tube packed bed model

Using the dimensions as calculated for the PCS system and the PCM mass as calculated the performance of the S&T packed bed model has been determined. The dimensions of the shell have been indicated such that the mass of the PCM present in the system is equal to that of the PCM mass present in the PCS system. At the same time, the dimensions of the PTC and the inner pipes in the LHTES have been adjusted to match to the sizing of the PCS model.

The number of LHTES units has been set equal to 91 643 equal to the total number of units of the PCS system. The mass of the PCM has been divided equally over these units. The radius of the shell has been determined by calculating the total volume that is occupied by the PCM and distributing this volume equally among the LHTES units and calculating the required volume of a shell as per Equation (4.18). As no encapsulation is required for this system the mass of the PCM particles can be used solely for PCM. With the aforementioned mass of the PCM of 6575 kg divided over 91 643 units the outer shell diameter is 2.9×10^{-4} m.

$$R_{shell} = \sqrt{\frac{\frac{m_{PCM}}{\rho_s N_{unit}}}{z_{HEX}\pi} + R_{HEX}^2} \tag{4.18}$$

To determine the performance of the S&T packed bed system the state of the PTC, LHTES and the heat transfer to the ORC have to be analyzed over the time duration of the test case.

A process flow diagram of the process to determine the state in the S&T packed bed system is pictured in Figure 4.9. The outlet temperature of the HEX has been considered to equal the inlet temperature of the PTC at 251.5 °C. The energy demand that is required to be transferred to the ORC is known, the inlet temperature of the ORC has been calculated accordingly. Based on the required inlet temperature of the HEX, which is calculated from the known energy demand of the ORC and the outlet state of the HEX, and the outlet temperature of the

PTC the mass flow that flows through a LHTES unit has been calculated. If the temperature at the outlet of the PTC is larger than required then the mass flow that goes straight to the HEX is based on the maximum mass flow that is required to fulfill the energy demand. The remaining mass flow is led through the LHTES unit only if the outlet temperature of the PTC is higher than the average temperature of the PCM in the shell.

If the outlet of the PTC does not contain enough heat to supply the demand created by the ORC then the HTF mass flow that is redirected through the LHTES unit to take up heat from the PCM is calculated based on the shortcoming of heat that has to be complemented by the LHTES. This mass flow can not become larger than the maximum HTF flow in the PTC at any time. If the energy in the storage has been depleted and no heat is added by the PTC the mass flow through the HEX is cycled to ensure all possible heat is transferred to the ORC. In Figure 4.10 the process flow diagram is provided including the parameters and the locations at which these parameters are taken to make the decisions as proposed in Figure 4.9.

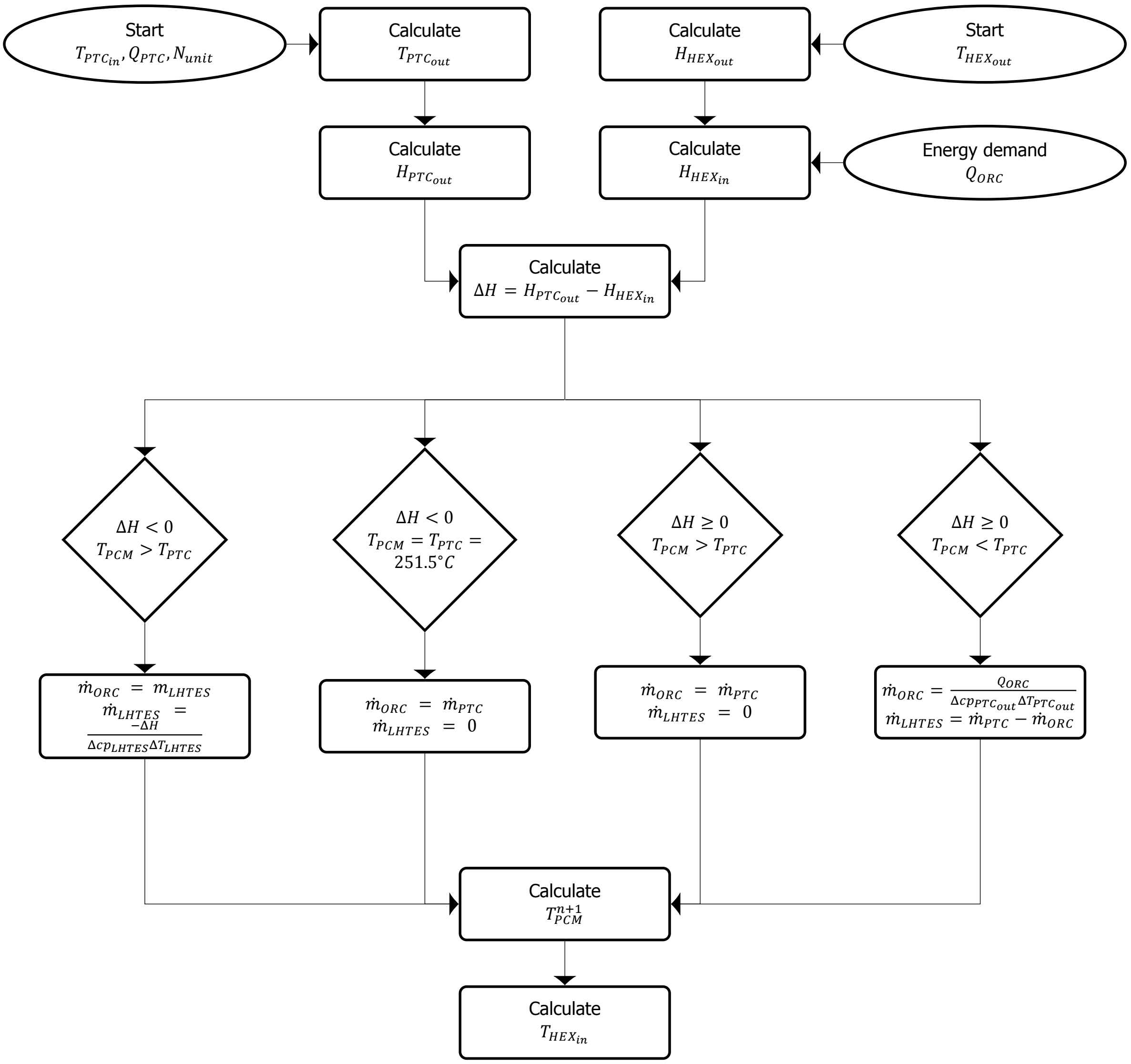

Figure 4.9: Process flow diagram of the iterative process for the numerical model of the S&T packed bed system to calculate the hourly state of the system.

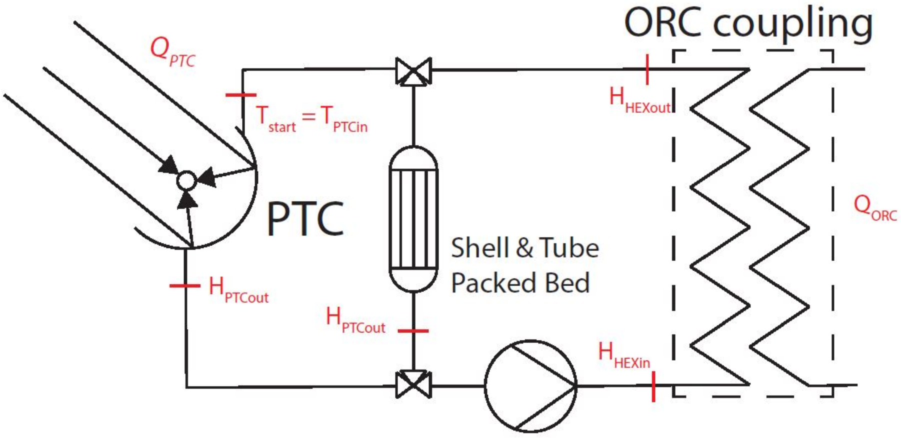

Figure 4.10: Process flow diagram of the updated S&T packed bed system including the parameters and their location that are required for calculating the mass flows.

The major difference between the two systems is found in the temperature of the HTF in the PTC. Whereas the majority of the heat that is received by the PTC in the PCS model is stored in the PCM particles this is not possible for the S&T packed bed model, resulting in a much higher outlet temperature at the PTC in this system. The steady-state outlet temperature of the PTC has been given in Table 4.2. This temperature is equal to the inlet temperature of the LHTES if excess heat is present and equal to the inlet temperature of the ORC if the energy demand can be met without supplementing heat from the storage. As expected a larger solar flux results in a higher outlet temperature per Equation (4.8). During the night no heat is received by the PTC and therefore the outlet temperature of the PTC is equal to the inlet temperature of the PTC.

Table 4.2: Hourly outlet temperature of the PTC in the S&T packed bed system.

Time [h]	$T_{PTC_{out}}$ [$^{\circ}C$]	**Time** [h]	$T_{PTC_{out}}$ [$^{\circ}C$]
11	290.8	23	251.5
12	287.7	24	251.5
13	282.4	1	251.5
14	274.1	2	251.5
15	264.6	3	251.5
16	256.3	4	251.5
17	251.8	5	251.5
18	25.5	6	256.8
19	251.5	7	267.0
20	251.5	8	277.1
21	251.5	9	286.1
22	251.5	10	290.9

The mass that flows through a PTC unit is almost constant when solar radiation is received by the PTC as the mean flow velocity and the PTC cross section area are fixed. The main deviation in the mass flow through the PTC resides in the change in density of the HTF that flows through the PTC. According to the process flow diagram that has been provided in Figure 4.9 the mass flow that leaves the PTC is split up into two flows, one going to the ORC to deliver the energy demand of the ORC and the remainder of the flow to the LHTES to heat up the PCM for storage. An overview of the value of these mass flows is given in Table 4.3.

From 11.00 to 17.00 the HTF is pumped through the LHTES as both excess heat is present from the outlet of the PTC and the outlet temperature of the PTC is higher than the temperature in the LHTES. Between 17.00 and 6.00 the LHTES is used to heat up the HTF flow to the ORC. At 17.00 the HTF mass flow going through the LHTES is low relative to the other hours as the HTF takes up most of the sensible heat present in the system, resulting in a high outlet temperature. It is found that some time before 18.00 the LHTES is no longer able to supply enough heat to the HTF to supply the ORC as the outlet temperature of the HTF flowing through the LHTES system does can not become higher than the temperature in the PCM. Once the sensible heat of the LHTES is removed the temperature of the PCM remains almost constant, due to the fact that the specific heat is much larger in the phase change temperature range.

Table 4.3: Hourly distribution of the HTF mass flow in the PTC, LHTES and PTC of the S&T packed bed model. The mass flow through one unit has been provided.

Time [h]	$\dot{m}_{PTC}$ [kg/s]	$\dot{m}_{LHTES}$ [kg/s]	$\dot{m}_{HEX}$ [kg/s]	**Time** [h]	$\dot{m}_{PTC}$ [kg/s]	$\dot{m}_{LHTES}$ [kg/s]	$\dot{m}_{HEX}$ [kg/s]
11	1.381×10^{-5}	1.004×10^{-5}	3.77×10^{-6}	23	0	1.381×10^{-5}	1.381×10^{-5}
12	1.358×10^{-5}	9.48×10^{-6}	4.10×10^{-6}	24	0	1.381×10^{-5}	1.381×10^{-5}
13	1.360×10^{-5}	8.77×10^{-6}	4.83×10^{-6}	1	0	1.381×10^{-5}	1.381×10^{-5}
14	1.363×10^{-5}	6.96×10^{-6}	6.67×10^{-6}	2	0	1.381×10^{-5}	1.381×10^{-5}
15	1.368×10^{-5}	2.07×10^{-6}	1.16×10^{-5}	3	0	1.381×10^{-5}	1.381×10^{-5}
16	1.373×10^{-5}	4.08×10^{-6}	1.381×10^{-5}	4	0	1.381×10^{-5}	1.381×10^{-5}
17	1.378×10^{-5}	1.381×10^{-5}	1.381×10^{-5}	5	0	1.381×10^{-5}	1.381×10^{-5}
18	0	1.381×10^{-5}	1.381×10^{-5}	6	1.381×10^{-5}	0	1.381×10^{-5}
19	0	1.381×10^{-5}	1.381×10^{-5}	7	1.378×10^{-5}	4.01×10^{-6}	1.380×10^{-5}
20	0	1.381×10^{-5}	1.381×10^{-5}	8	1.372×10^{-5}	7.84×10^{-6}	5.88×10^{-6}
21	0	1.381×10^{-5}	1.381×10^{-5}	9	1.366×10^{-5}	9.37×10^{-6}	4.30×10^{-6}
22	0	1.381×10^{-5}	1.381×10^{-5}	10	1.361×10^{-5}	9.85×10^{-6}	3.76×10^{-6}

The average temperature of the PCM in the LHTES and the temperature of the HTF flowing out of the PTC is provided in Figure 4.11. It is seen that in the first hour the PCM slowly heats up due to being heated by the HTF. After some time the average temperature of the PCM drops. This is due to the fact that the heat is more equally divided over the PCM, resulting part of the sensible heat that was present at first to be converted to latent heat in the part of the LHTES that has not received much heat yet. At 17.00 the outlet temperature of the HTF in the PTC drops below the temperature of the LHTES and some heat is supplemented to the ORC. From 18.00 to 5.00 there is no solar radiation and the entire flow of HTF is fed through the LHTES to take up heat. The average temperature of the LHTES lowers slowly from 254.5 °C to 252.9 °C as the latent heat is taken up. At 7.00 excess heat from the PTC is again available to heat up the PCM in the LHTES. The average temperature in the LHTES at the end of the day is much higher because not all latent heat has been removed from the LHTES before additional heat is added at 7.00.

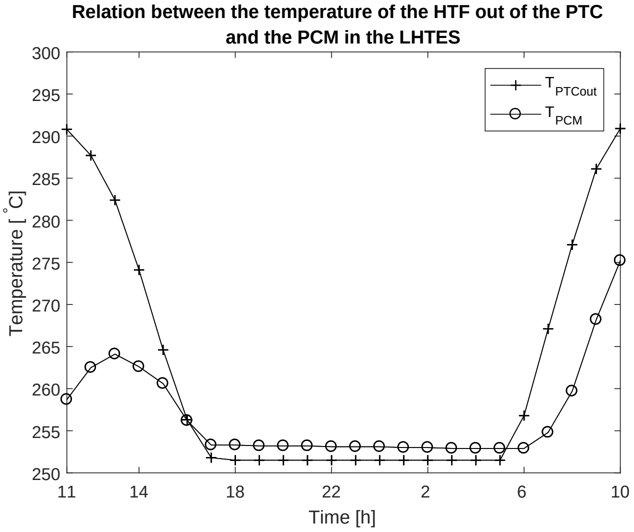

Figure 4.11: Temperature of the HTF coming out of the PTC and the PCM in the LHTES at the end of every hour throughout the test case.

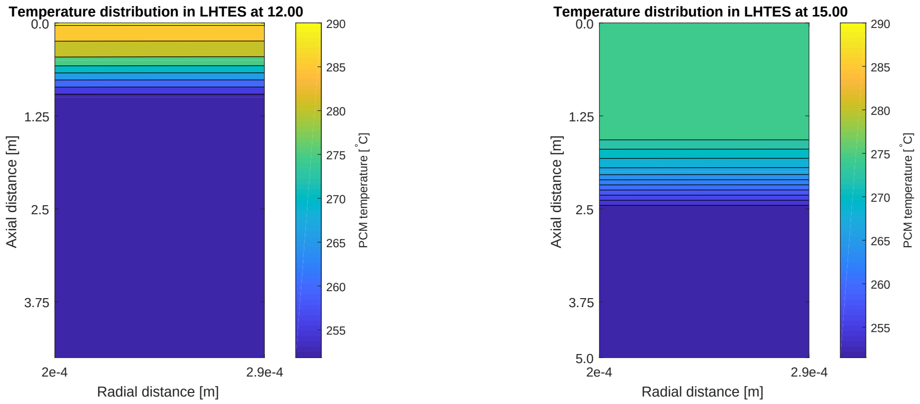

(a) Temperature distribution of the PCM in the LHTES at 12.00

(b) Temperature distribution of the PCM in the LHTES at 15.00

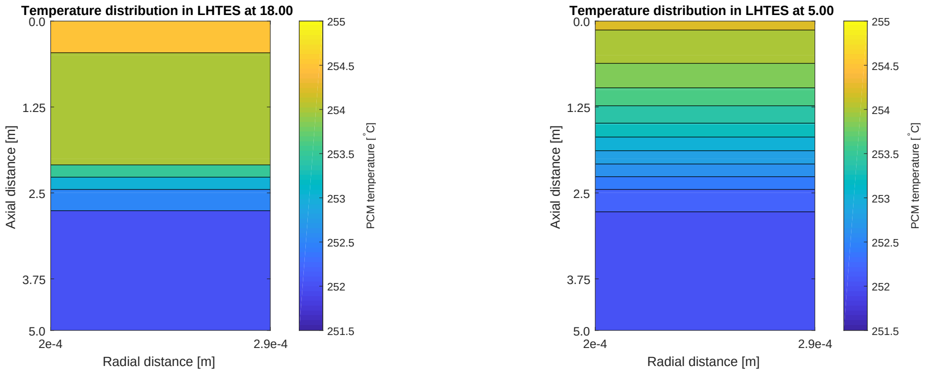

(c) Temperature distribution of the PCM in the LHTES at 18.00

(d) Temperature distribution of the PCM in the LHTES at 5.00

Figure 4.12: Temperature distribution of the PCM in the LHTES at four time points. At 12.00, when the system has run for one hour. At 15.00, when the heat storage in theLHTES is at a maximum. At 18.00, when the sensible heat has been withdrawn from the LHTES and at 5.00 when the amount of heat stored in the LHTES is at a minimum.

The temperature distribution of the PCM in the LHTES at four different times has been provided in Figure 4.12a up to Figure 4.12d. The highest temperature, 290.8 °C equal to the outlet temperature of the PTC, in the LHTES has been achieved during the first hour of operation, as pictured in Figure 4.12a. More heat is stored in the LHTES resulting in the temperature distribution depicted in Figure 4.12b. A lower temperature distribution is present because latent heat is better utilized. PCM at the end of the pipe has not melted, it can be stated that the PCM mass is oversized for the system.

Figure 4.12c shows the temperature distribution after the first hour at which heat is depleted from the system. Most of the sensible heat has been removed. Figure 4.12d provides the temperature distribution when the heat storage is at a minimum. It is noted that there is still heat present in the LHTES that has not been transferred to the HTF.

The inlet temperature of the HEX as well as the amount of heat transferred to the ORC has been given in Table 4.4. The heat transferred to the ORC has calculating the difference between the in and outgoing heat as presented in Equation (4.19). During the first six hours enough heat is delivered to the ORC. The first five hours the PTC heats up the HTF enough and from 16.00 up till 17.00 the LHTES makes up the deficit from the outlet of the PTC. Once the sensible heat is removed from the LHTES it can no longer heat up the HTF enough for it to deliver enough heat to the ORC. Not until 7.00, when the PTC once again heats up the HTF, can the energy demand of the ORC be met by the S&T packed bed model.

$$\dot{Q}_{ORC} = N_{unit}\dot{m}_{HEX}\left((T_{HEX_{in}}cp_{HEX_{in}}(T_{HEX_{in}}) - T_{HEX_{out}}cp_{HEX_{out}}(T_{HEX_{out}})\right) \tag{4.19}$$

Table 4.4: The hourly temperature at the inlet of the HEX and amount of heat that is transferred to the ORC. It is indicated whether the HTF receives heat from the PTC or the LHTES.

Time $[h]$	T_{HEX} $[^{\circ}C]$	$\dot{Q}_{ORC}$ $[kW]$	**HTF flow location**
11	290.8	47.4	PTC
12	287.7	47.4	PTC
13	282.4	47.4	PTC
14	274.1	47.4	PTC
15	264.6	47.4	PTC
16	256.3	47.4	PTC & LHTES
17	251.8	12.8	LHTES
18	251.5	12.7	LHTES
19	251.5	12.7	LHTES
20	251.5	12.6	LHTES
21	251.5	12.5	LHTES
22	251.5	12.4	LHTES
23	251.5	12.3	LHTES
24	251.5	12.2	LHTES
1	251.5	12.0	LHTES
2	251.5	11.9	LHTES
3	251.5	11.7	LHTES
4	251.5	11.5	LHTES
5	251.5	11.4	LHTES
6	256.8	22.5	PTC
7	267.1	47.4	PTC
8	277.1	47.4	PTC
9	286.1	47.4	PTC
10	290.9	47.4	PTC

4.6. Conclusion

A comparison has been made between two systems that make use of PCM to store heat that is collected from a PTC. Using a defined test case, for the duration of a day with hourly variable energy input and a fixed energy demand, the transient performance of both systems has been examined. To meet the requirements of the test case using the dimensions for optimal thermal performance as established in Section 3.6 it has been found that a total of 91 643 units are required and a total of 6575 kg PCM is required to deliver the heat to the ORC during the entire day. These dimensions have been carried over for use in the S&T packed bed model to allow for a fair comparison.

The storage is filled and depleted during the same hours of the day in both systems. The storage potential of the LHTES in the S&T packed bed system is however not fully utilized. The temperature in the LHTES storage can not reach a higher temperature than the HTF that enters the LHTES. To extract heat from the LHTES the same holds, the outlet temperature of the HTF can not become higher than the temperature of the PCM. From Table 4.2 it is seen that at 10.00 the maximum PTC outlet temperature has been achieved. At 16.00 the PTC can no longer deliver the energy as required by the ORC and the HTF is led through the LHTES system to supplement the required energy. After 17.00 the energy demand of the ORC is no longer met. At 8.00 the energy demand is met again and additional heat is present to be stored in the LHTES.

The major difference is present in the outlet temperature of the PTC of the PCS model and the S&T packed bed model and the number of cycles that the PCM experiences in both systems. Next to that there is a temperature difference between the HTF and the PCM in the S&T packed bed system, whereas there is no temperature difference in the PCS system. A comparison between the outlet temperatures of the PTC in both models has been given in Table 4.5.

Table 4.5: Comparison of the outlet temperature of the PTC of the two tested models.

Time $[h]$	**S&T packed bed** $T_{PTC_{out}}$ $[^{\circ}C]$	**PCS** $T_{PTC_{out}}$ $[^{\circ}C]$
11	290.8	254.0
12	287.7	253.9
13	282.4	253.7
14	274.1	253.0
15	264.6	252.4
16	256.3	251.8
17	251.8	251.5
18	251.5	251.5
19	251.5	251.5
20	251.5	251.5
21	251.5	251.5
22	251.5	251.5
23	251.5	251.5
24	251.5	251.5
1	251.5	251.5
2	251.5	251.5
3	251.5	251.5
4	251.5	251.5
5	251.5	251.5
6	256.8	251.8
7	267.1	252.8
8	277.1	253.2
9	286.1	253.9
10	290.9	254.0

Because the heat transferred to the ORC in the S&T packed bed model is only done via sensible heat a larger temperature increment between the inlet and outlet of the HEX is required to meet the energy demand compared to the PCS model. However it has to be taken into account that the configuration is based on the optimal sizing of the PCS model. Because the heat that is present is not fully utilized, increasing the mass flow through the LHTES might result in this heat to be withdrawn from the PCM to meet the energy demand of the ORC. Furthermore the temperature of the HTF passing through the LHTES system can not attain a higher temperature than the temperature of the PCM at the outlet of the system. As the S&T packed bed system can only transfer sensible heat to the ORC the heat that is available in the HEX is limited.

The PCM that is present in the PCS model in the pipes, required to bridge the distance between the components in the system, has not been taken into account. It has been assumed that a unit consists only of the pipes in the PTC and the HEX but in reality there are a lot more pipes. The presence of these pipes contribute to the total amount of PCM that is present in the system as the volumetric particle concentration has to be equal at all locations in the pipe. Thus in reality the total mass of the PCM in the units is larger than has been stated. The influence on the total PCM mass when taking into account these pipes is discussed in Section 5.3.

With the configuration as proposed in Section 3.6 and the test case as given in Section 4.4 it is stated that the transient performance of the PCS model is better than the transient performance of the S&T packed bed model. This is due to the fact that with the same PCM mass and number of units present the PCS system can meet the energy demand for the test case throughout the day, while the S&T packed bed system can not.

To optimize the use of the LHTES in the S&T packed bed system a different working fluid in the ORC is required such that the operating temperature can be lowered. An operating temperature range at which the melting temperature of the PCM is the upper limit would allow for fully utilizing the heat stored in the LHTES. Increasing the mass flow through a unit when heat is taken up from the LHTES might be another solution to fully utilize the heat stored in the LHTES.

5

Upscaling of systems

The systems that have been compared in Chapter 4 may be optimal for thermal behaviour but are not practical. The size of these systems is not cost effective as the required number of units is large. Upscaling of these systems has been analyzed to make a comparison of the practical systems. Section 5.1 presents the purpose of the scaling that is proposed in Section 5.2. Section 5.3 provides the performance of the scaled systems and in Section 5.4 the thermal performance of the uspcaled systems is compared to the systems proposed in Chapter 4. The conclusions are presented in Section 5.5.

5.1. Purpose

The design of the original system , made in Chapter 4, is not feasible in terms of cost. Therefore a new analysis has been made for both systems for which the dimensions of the systems have been scaled up to represent a more practical size. The behaviour of the systems alters with sizing and therefore a second analysis has been made to investigate the performance of these scaled up systems.

5.2. Scaling of dimensions

To create a system that has technically feasible and cost effective dimensions the system as discussed in Chapter 4 has been scaled up. The scaling has been aimed to results in 100 units. Thus the scaling of the system has to be done in such a way that the energy demand is met using only 100 units instead of the 91 643 units as determined in Section 4.5. Next to that 100 m of piping per unit is taken into account to find out what the effect of piping is on the total required mass of PCM in the system.

The energy that has to be stored at the time when maximum storage is required is equal to 691 kW h as has been calculated before and a total of 1138 kW h has to be delivered to the ORC. The average power output of the system with 91 643 units has been calculated to be 0.798 W. Scaling this number to represent 100 units results in an average power production per unit of 767 W. This power production can be achieved by scaling the radius of the PTC to increase the surface area of the PTC and with that the incoming heat flux. The most effective way to obtain a larger surface area is to increase the radius of the PTC because the surface area, and therefore the incoming solar radiation, scales linearly with the PTC radius. Two tests have been performed, one in which the particle to pipe radius has been kept constant at 0.04 and one in which the particle radius was kept at 400×10^{-8} m. It was found that in the test where the particle to pipe radius retained its original value the PCM particles did not show good thermal performance, the particles could not take up much heat from the HTF resulting in a temperature difference between the HTF and the PCM particles. Therefore it has been decided to keep the particle radius at 400×10^{-8} m as proposed in Section 4.6.

The radius of the PTC is expected to increase more than linearly with the change in the number of units because a larger incoming solar radiation results in a higher steady-state temperature because it allows for better latent heat storage as was found in the sensitivity analysis. Next to that an increase in the radius results in a quadratic increase in the surface area and consequently the incoming solar radiation. However, as the thermal behaviour of the PTC is worse with a larger pipe radius, it is expected that an increase of PCM mass is required to realize the same energy output. The radius of the PTC and the HEX has been increased from 1×10^{-4} m to 1×10^{-2} m. The other parameters have been kept at their original values.

To come to the mass of the PCM the volume of the PCM in the system has been calculated. The volume that is present in the units at all times has been determined by calculating the volume of the PTC, HEX and the piping according to Equation (4.15), Equation (4.16) and Equation (4.17). The intersection area has been calculated with the new tube radius and equals 3.14×10^{-4} m^2. This area has been multiplied with the axial length to come to the volume. The axial length of the PTC and the HEX have been kept at 5 m, while the piping has been taken to account for 100 m per unit.

The dimensions of the S&T packed bed model have been based on the dimensions of the PCS system to make a fair comparison. The radius of the pipes has been increased with the same factor such that the same solar irradiance is received. According to the sensitivity analysis as performed by Fan the performance of the S&T packed bed model decreases with an increase in pipe radius and PCM mass [17]. Therefore it is expected that the scaled up version has worse thermal performance than the version discussed in chapter 4. The outer radius of the shell containing the PCM is once again determined by Equation (4.18).

5.3. Performance of scaled systems

The change in enthalpy in both the PTC and the HEX has been evaluated using the method as described in Section 4.5. With Equation (4.11) to Equation (4.14) the performance has been assessed and tabulated in Table 5.1. During the time period when the solar radiation is high the energy output of the system is high as well. When no solar radiation is available there is no energy added in the PTC and the excess heat that has been stored is used to deliver the energy demand to the ORC. The average energy that is transferred to the ORC is 509.9 W. In the original system the average energy transferred is 0.798 W.

The storage required to meet the energy demand of the ORC when no solar irradiance is present has been addressed to obtain the total number of units. Based on the delivered energy to the ORC as found and given in Table 5.1 it has been found that 145 units are required to meet the energy demand with this configuration. This is a slightly higher number than the 100 units that were aimed for.

The total mass of the PCM particles in the system has been calculated by finding the total volume of the PCM present in the system, including the PTC, the HEX and the pipes, and present in the storage. Multiplying this total volume with the solid density of the particle as indicated in Equation (4.15) to Equation (4.17) results in the total PCM mass in the system. Taking into account that the volumetric particle concentration is equal to 0.23, the volume of the PCM particles in the 145 units is equal to 0.105 m^3. The total volume of the PCM particles in the pipes equals 1.05 m^3.

In Table 5.1 the equivalent volume flow to the storage has been given, as well as the total energy that is stored. At 16.00 the maximum amount of energy stored has been achieved at 699.9 kW h. The maximum volume of storage is required, equal to the equivalent hourly flow of 461 units. This has been multiplied with the cross section area, mean flow velocity and seconds per hour to come to a total PCM particle volume of 60.0 m^3. The total volume that the PCM particles occupy in the system is 61.1 m^3. This is multiplied with the solid particle density of 1621 kg/m^3 to find the total mass of the PCM particles in the scaled up system to equal 99 061 kg. The PCM mass increases 151 times with respect to the original configuration, while the pipe radius increases by a factor 1001. The distribution of the PCM volume in both the original and the scaled up PCS system is found in Figure 5.2. It is seen that the PCM volume in the pipes is negligible compared to the PCM volume present in the storage in both cases.

Table 5.1: Hourly heat transfer rate per unit from the HEX to the ORC for the scaled up PCS system. Also the amount of energy in storage and the change in energy in the storage on an hourly basis are given.

Time [h]	**$\dot{Q}$ [W]**	**Number of equivalent units of flow directly to storage**	**Change in energy in storage [kWh]**	**Total energy in storage at the end of hour [kWh]**
11	2180	124	268.7	268.7
12	1966	121	235.7	506.4
13	1072	101	107.0	614.4
14	842.2	89	73.9	689.1
15	401.3	27	10.4	699.9
16	53.6	0	-39.7	660.3
17	1.2	0	-47.2	613.1
18	0	0	-47.4	565.7
19	0	0	-47.4	518.3
20	0	0	-47.4	470.9
21	0	0	-47.4	423.5
22	0	0	-47.4	376.1
23	0	0	-47.4	328.7
24	0	0	-47.4	281.3
1	0	0	-47.4	233.9
2	0	0	-47.4	186.5
3	0	0	-47.4	139.1
4	0	0	-47.4	91.7
5	0	0	-47.4	44.3
6	63.6	0	-38.2	6.1
7	522.8	54	27.9	34.5
8	950.4	95	89.5	124.9
9	1959	121	234.7	361.6
10	2225	124	273.0	636.8
Average	509.9	35.2		

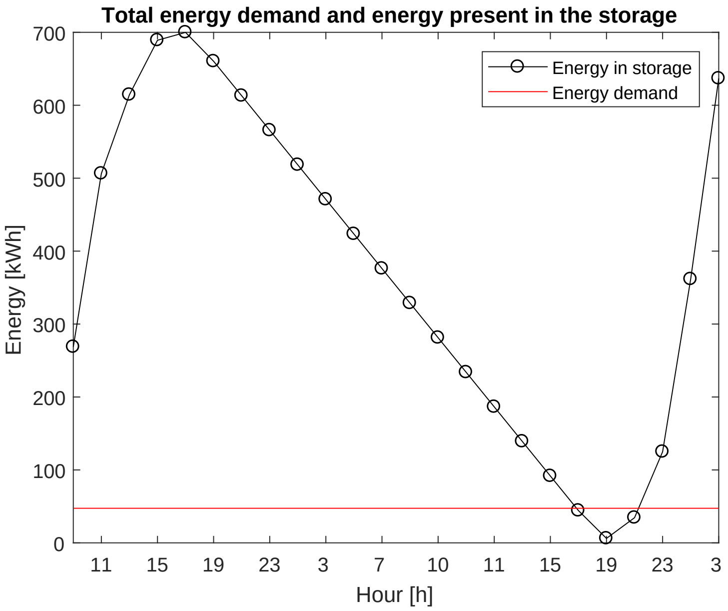

Figure 5.1: Total energy available in storage of the scaled up PCS system compared to the energy demand throughout the day.

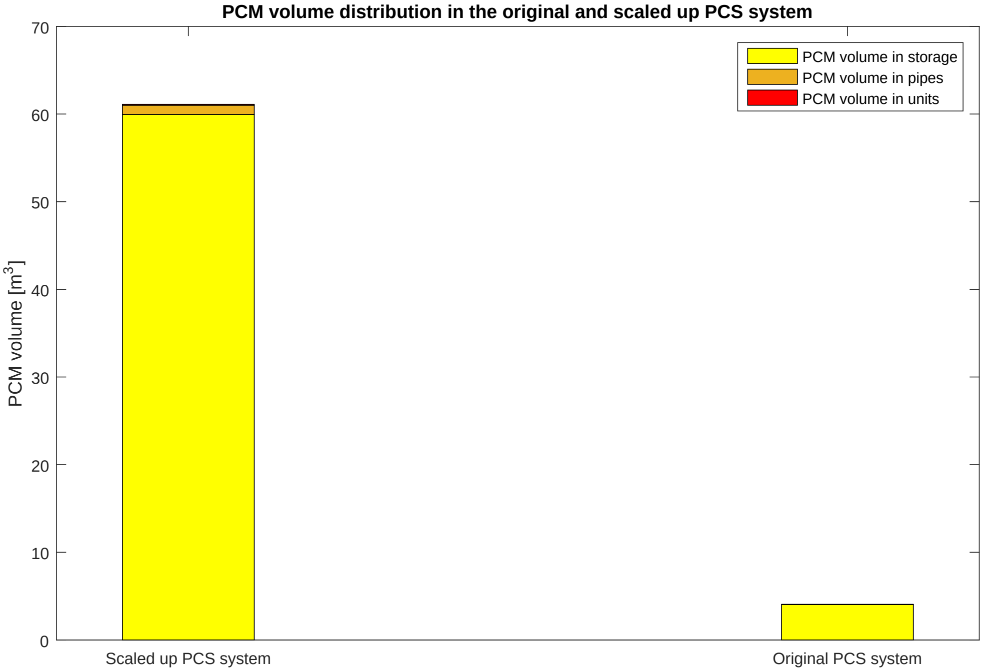

Figure 5.2: Comparison between the distribution of PCM volume in the scaled up and original PCS system. The majority of the PCM mass is found in the storage vessel.

The S&T packed bed model has been sized according to the configuration that has been specified in Section 5.2. The outer diameter of the shell that contains the PCM is 0.288 m. Compared to the outer diameter of the pipe, which has a diameter of 0.02 m, it is very large. The outlet temperature of the PTC has been calculated on an hourly basis and is presented in Table 5.2. It is seen that the outlet temperature is significantly lower for the scaled up version of the system compared to the original system. The reason for this is that the cross section area of the pipe has a larger increase than the surface area when the radius of the pipe increases. Because the pipe radius of the PTC is larger than the pipe radius in the original system the mass flow flowing through the PTC increases from 1.381×10^{-5} kg/s to 0.138 kg/s. Because the surface area is larger the received solar radiation increases from 1.3×10^{-3} kW to 0.133 kW for one pipe in the PTC. The mass flow increases with a larger factor than the received solar radiation, resulting in a lower outlet temperature at the PTC.

Table 5.2: Hourly outlet temperature of the PTC in the scaled up S&T packed bed system.

Time $[h]$	$T_{PTC_{out}}$ $[^\circ C]$	**Time** $[h]$	$T_{PTC_{out}}$ $[^\circ C]$
11	251.9	23	251.5
12	251.9	24	251.5
13	251.8	1	251.5
14	251.7	2	251.5
15	251.6	3	251.5
16	251.5	4	251.5
17	251.5	5	251.5
18	251.5	6	251.6
19	251.5	7	251.7
20	251.5	8	251.8
21	251.5	9	251.8
22	251.5	10	251.9

Due to the lower outlet temperature of the PTC not enough heat is present to heat up the PCM in the LHTES system. Even at the peak heat influx the temperature increase generated in the PTC is not enough to deliver the energy demand to the ORC as calculated with Equation (4.19). At 10.00, when the outlet temperature of the PTC is at a maximum, the heat that is transferred to the ORC is 26.7 kW, 56% of the total energy demand of the ORC.

5.4. Comparison of thermal performance

An increase in time until steady state is coherent with an increase in pipe radius. With a larger pipe radius more solar radiation is added to the system which results in a higher steady-state temperature. A unit with the dimensions as outlined in Section 3.8 takes 10 s to reach steady state but a scaled up version can take up to 320 s to reach it, equal to 9% of an hour. During this time the temperature of the PCS is not constant. However the increment of the temperature during the first few seconds is large compared to the rest of the time required to reach steady state. Hence the assumption that the performance of the model is only in steady state is still considered to be valid.

The total PCM particle mass in the system increases from 6575 kg to 99 061 kg in the scaled up system, an increase of 1500%. This increase is mostly due to the fact that the PCM is hardly utilized in the scaled up system. The temperature distribution at peak heat influx is provided in Figure 5.3. Here it is seen that the PCM particles at the wall obtain a high temperature but the PCM particles at the center of the pipe receive almost no heat. PCM particles that are present at the center of the pipe do not contribute to the storage of heat but are required to be present in the PCS to ensure an uniform distribution of particles. Therefore the PCM mass is required to be much larger in the scaled up system to meet the same energy demand.

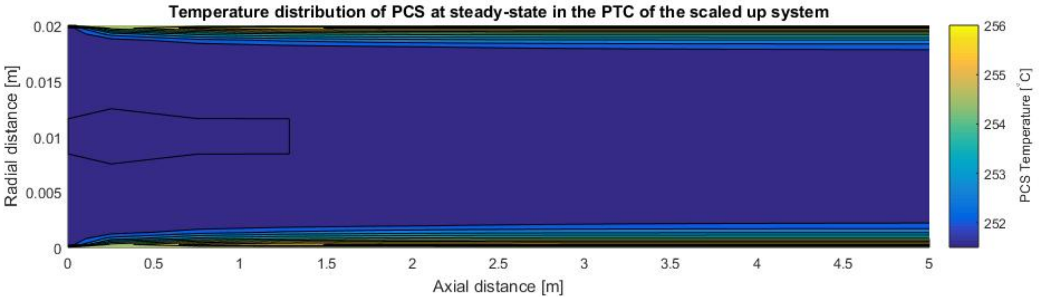

Figure 5.3: Temperature distribution of the PCS in the scaled up version of the PTC at steady state.

Because the particle radius is kept at 400×10^{-8} m the particles can transfer heat good and have a uniform temperature distribution. Therefore temperature distribution of the particles in the PTC is identical to the temperature distribution of the HTF. The same is true for the PCM particles in the HEX. The temperature distribution in the HEX is provided in Figure 5.4. The temperature at the outlet of the HEX does not fully equal the inlet temperature of the PTC. The difference between the heat added in the PTC and the heat removed in the PTC is provided in Table 5.3. It is found that for small solar irradiance input the heat in the HEX is transferred completely to the ORC, but for solar radiation above 350 W losses become apparent. Only a slight difference between in and outgoing energy is noted, a maximum of 153.5 W is not utilized due to the non-optimal design of the HEX. It is not considered beneficial to redesign the HEX for this small difference. Because the temperature of the HTF in the PTC is higher in the scaled up PCS system than the original PCS system it is expected that losses due to radiation increase.

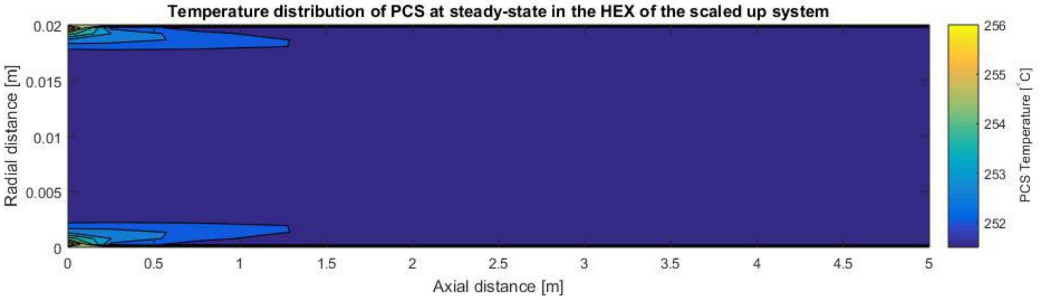

Figure 5.4: Temperature distribution of the PCS in the scaled up version of the HEX at steady state.

Table 5.3: Hourly heat transfer rate per unit from the PTC to the HEX and theHEX to ORC for the scaled up PCS system. A discrepancy indicates that heat transfer in the HEX is not optimal.

Time $[h]$	$\dot{Q}_{PTC}$ $[W]$	$\dot{Q}_{HEX}$ $[W]$
11	2192	2180
12	1977	1966
13	1078	1072
14	846.3	842.2
15	404.3	401.3
16	53.7	53.6
17	1.2	1.2
18	0	0
19	0	0
20	0	0
21	0	0
22	0	0
23	0	0
24	0	0
1	0	0
2	0	0
3	0	0
4	0	0
5	0	0
6	63.6	63.6
7	525.0	522.8
8	954.7	950.4
9	1964	1959
10	2330	2225
Average	516.2	509.9
Total difference	153.5	

A problem may arise in the storage vessel of the PCS. As is seen from Figure 5.3 the PCM particles have a huge variation in temperature. When these are mixed in the storage vessel a uniform temperature is obtained over time, PCM particles that were present at the wall of the PTC will transfer heat to the PCM particles that were present at the center of the PTC. This reduces the useful heat in the system because the overall temperature becomes lower.

A comparison has been made for the S&T packed bed model as well. Due to a larger increase in volumetric flow rate than surface area in the PTC the outlet temperature of the PTC is lower. The maximum outlet temperature that has been achieved is 251.9 °C during peak heat influx. This outlet temperature is equal to the the temperature obtained at 17.00 in the original S&T packed bed system. A different configuration for the S&T packed bed system is required for it to be a suitable system for the test case.

5.5. Conclusion

A scaled up version of the PCS model and the S&T packed bed model has been created to determine the performance of these systems at workable levels. It has been found that a pipe radius of 1×10^{-2} m results in a requirement of 145 units to meet the energy demand of the ORC for the test case. The mass of the PCM that is required to have an even distribution in the system is equal to 99 061 kg. This is a large increase from the 6575 kg of PCM that is required for the original system. This increase of PCM mass is explained with help of the temperature distribution in the system of the scaled up system. The PCM particles at the center of the PTC do not receive any heat and therefore do not contribute to the thermal performance of the system but have to be included to obtain a uniform particle distribution in the PCS.

A scaled up version of the S&T packed bed model has also been tested. At no point it is able to take up enough heat to deliver to the ORC. This is due to the increase in volume flow rate in the PTC which results in a lower output temperature. Not enough sensible heat is present in the HTF that enters the HEX to meet the energy demand of the ORC.

6

Conclusions

A study concerning a phase change material slurry to transport and store heat for a medium operating temperature range has been conducted. This operating temperature range has been specified to lie between 200 °C and 300 °C. A numerical model has been designed to model the transient behaviour of such a system and has been sized for an optimal performance. This model has then been compared to a numerical model of a S&T packed bed model to investigate and compare the transient behaviour of such systems.

PCMs have been studied to determine a suitable material for the process under investigation. It has been found that inorganic materials are most suitable for this process due to the fact that their melting temperature lies in the operating range. Next to that they display a larger heat storage capacity per volume and better thermal conductivity than other studied materials. $LiNO_3$ has been found to match the proposed requirements for the process and has been selected based on its large heat of fusion. MarloTherm SH has been picked as a HTF for this process for having a good thermal conductivity and specific heat capacity and has been proven in previous studies to be compatible with multiple encapsulation materials. Microencapsulation has been added to the PCM particles to provide better thermal conductivity and increase their stability. ENG has been found to be the most suitable candidate and has been used as encapsulation material successfully before. This encapsulation increases the thermal conductivity but also increases the Stefan number of the particles with an increase in volumetric concentration, resulting in a lower capability to store heat.

Supercooling is a phenomenon that causes the PCM to solidify at a lower temperature than the actual crystallization temperature and is present in inorganic PCMs. This has been incorporated in the numerical model by applying a phase change temperature range instead of a sharp melting temperature. From the numerical model it has been found that the size of this phase change temperature range does not influence the performance of the system. However, for sharp melting temperature ranges and systems with a small operating temperature range supercooling is a problem and should be averted by adding a nucleation agent to the phase change material.

To include the effect of heat transfer due to convection, the principle of effective conductivity has been applied. This effective conductivity is a function of the homogeneous thermal conductivity of the PCS, the volumetric particle concentration and the particle Peclet number. When these parameters increase the effective conductivity increases with them. A larger volumetric particle concentration causes an increase in the effective thermal conductivity as the additional effect of convection through the particle bed is beneficial. A better performance of the PCS system has been found when the effective thermal conductivity was included.

Parameters that have an influence on the performance of the PCS model have been analyzed and varied to come to the optimal sizing. A good performance has been stated to include a large ratio of latent heat over sensible heat in the outlet of the PTC. The influence of the particle size, particle to pipe radius, volumetric particle concentration, volumetric PCM concentration, mean flow velocity, axial length, as well as numerical parameters, on the performance of the PTC have been examined. It was found that an increase in volumetric particle concentration and volumetric PCM concentration have a positive influence on the performance, whereas a decrease in the particle radius as well as the mean flow velocity lead to an increase in performance. The particle to pipe radius ratio and the axial length of the PTC have an optimum that depends on the value of the other parameters. Based on the sensitivity analysis the sizing for optimal performance has been decided upon.

The transient behaviour of the PCS model has been compared to the behaviour of a S&T packed bed model. To be able to compare these two models a test case has been constructed which has the duration of one day with a variable hourly solar flux input and a fixed energy demand based on the load of 25 households. For the optimal performance of the PCS system a total of 91 643 units is required with a total PCM particle mass of 6575 kg. When these dimensions have been applied to the S&T packed bed model it was found that it can not deliver the required energy demand. The main reason for this is that only sensible heat is used to transfer heat to the ORC in the S&T packed bed model. When heat from the storage withdrawn the temperature of the HTF does not become higher than the melting temperature of the PCM. Therefore the amount of heat available to be transferred to the ORC is limited. Next to that the HTF and PCM have the same temperature whereas there exists a mismatch between these temperatures in the S&T packed bed model which results in not using the stored heat in an optimal way.

A scaled up version has been tested at more practical dimensions. It has been found that the performance does not have a linear relationship to the heat influx. When the surface area of a unit is increased due to a larger pipe radius the volumetric enthalpy increases because a higher wall temperature is present in the PTC. When the number of units is decreased from 91 643 to 145 the PCM mass increases from 6575 kg to 99 061 kg. The PCM particles present in the center of the pipe do not contribute to the heat storage due to limited heat penetration into the pipe. For a scaled up system less equipment is required, but more PCM mass.

The scaled up version was also compared, using the same method, to a scaled up version of the S&T packed bed model. It was found that the S&T packed bed model could not even deliver the energy demand during peak heat influx, due to a lower outlet temperature in the PTC.

7

Recommendations

Based on the obtained results from the research that has been performed recommendations for further research are proposed.

The numerical method present in the PCS model is not numerically stable for large velocities and/or small particles. Particle radii below 400×10^{-8} m and a mean flow velocity larger than 10 m/s could not be simulated without making adaptations to the model. The introduction of nanoparticles has made this range interesting for several applications. Therefore the PCS model could be expanded to allow for simulation in this range.

An even particle distribution has been assumed in the numerical model. This is highly unlikely in reality and therefore it could be interesting to implement different types of distributions and the interparticle forces that are implemented with these distributions and what effects it has on the heat transfer in the PCS.

Regarding the system that has been designed a more thorough design of the HEX could be made to optimize the heat transfer to the ORC. As the number of cycles that the PCM particles experience is large, the stability of PCM particles as proposed in this thesis has to be researched. More research is required on the stresses that the PCM particles can withstand, as well as the lifetime up till fatigue failure. A cost and life cycle analysis of such a system should be included. Also the encapsulation method for the PCM particles could be tested experimentally.

Different test cases may be implemented to find other uses for the the compared systems. The performance of the systems might be better for cases that have not been considered in this study. A configuration for the scaled up S&T packed bed model may be looked for that is able to supply the energy demand of the ORC.

Last the viability of this PCS model could be tested. Although PCM particles have been produced with the selected materials, these have not been implemented into a suspension. Next to that it would be beneficial for the heat transfer ability of the PCS to allow for the PCM particles to be suspended without requiring encapsulation for stability. Therefore it is interesting to find out how the selected PCM behaves in the selected HTF.

A

Appendix

Data Tables

Table A.1: Thermodynamic properties of Marlotherm SH as a function of temperature [50].

T [°C]	ρ_l [kg/m^3]	cp_l [$kJ/kg°C$]	λ_l [$W/m°C$]	ν [mm^2/s]
0	1058	1.48	0.133	321
20	1044	1.55	0.131	47
40	1030	1.62	0.128	16.5
60	1016	1.7	0.125	8.1
80	1001	1.77	0.123	4.7
100	987	1.85	0.12	3.1
120	973	1.92	0.117	2.3
140	958	1.99	0.115	1.8
160	944	2.07	0.112	1.4
180	930	2.15	0.11	1.2
200	915	2.22	0.107	0.95
220	901	2.29	0.104	0.77
240	887	2.37	0.102	0.65
260	873	2.44	0.099	0.57
280	858	2.52	0.096	0.5
300	844	2.59	0.094	0.45
320	830	2.67	0.091	0.4
340	815	2.74	0.088	0.36
360	801	2.82	0.086	0.32

$$cp_{htf_{fit}}[J/kg°C] = 3.73T + 1475 \tag{A.1}$$

$$\rho_{htf_{fit}}[kg/m^3] = -0.715T + 1058 \tag{A.2}$$

$$\lambda_{htf_{fit}}[W/m°C] = -1.32 \times 10^{-4}T + 0.133 \tag{A.3}$$

$$\mu_{htf_{fit}}[Pas] = -0.018 \times 10^{-3}T + 5.36 \times 10^{-3} \qquad for \qquad T \geq 60°C \tag{A.4}$$

Table A.2: Thermodynamic properties of $LiNO_3$ as a function of temperature [28, 62].

$T\ [^\circ C]$	$\rho\ [kg/m^3]$	$\mu\ [mPas]$	$cp\ [kJ/kg^\circ C]$	$\lambda\ [W/m^\circ C]$	$\gamma\ [cm^{-1}]$
20	2380			0.51	
61.85			1.33		
126.85			1.45		
176.85			1.59		
206.85			1.63		
231.85			1.69		
241.85			1.78		
251.85				1.3502	
253.85	2120			1.3682	
256.85			2.04	0.6104	
266.85		5.222	2.04	0.6125	
276.85	1767	4.835	2.04	0.6146	
286.85	1762	4.479	2.03	0.6167	
296.85	1757	4.152	2.06	0.6188	113.6
306.85	1751	3.856	2.05	0.6209	113
316.85	1745	3.589	2.06	0.6230	112.5
326.85	1740	3.352	2.08	0.6251	111.9
336.85	1735	3.146	2.06	0.6272	111.4
346.85	1729	2.969	2.07	0.6293	110.8
356.85	1724	2.822	2.11	0.6314	110.3
366.85	1718	2.705	2.1	0.6335	109.7
376.85	1713	2.619	2.09	0.6355	109.2
386.85	1707			0.6376	108.6
396.85	1702			0.6397	108.1
406.85	1696			0.6418	107.5
416.85	1691			0.6439	107
426.85				0.6460	106.4
436.85				0.6481	105.9
446.85				0.6502	105.3
456.85				0.6523	104.8
466.85					104.2
476.85					103.7
486.85					103.1
496.85					102
506.85					102

$$cp_{pcm_{fit}}[J/kg^\circ C] = \begin{cases} 2.39T + 1165 & \text{if } T \leq T_m - \Delta T \\ 134T - 3203 & \text{if } T_m \geq T > T_m - \Delta T \\ 0.0023T^2 - 0.922T + 2117 & \text{if } T > T_m \end{cases} \tag{A.5}$$

$$\rho_{pcm_{fit}}[kg/m^3] = \begin{cases} -1.145T + 2403 & \text{if } T \leq T_m - \Delta T \\ -83.38T + 22958 & \text{if } T_m \geq T > T_m - \Delta T \\ -0.5424T + 1917 & \text{if } T > T_m \end{cases} \tag{A.6}$$

$$\lambda_{pcm_{fit}}[W/m^{\circ}C] = \begin{cases} 0.0036T + 0.4375 & \text{if } T \leq T_m - \Delta T \\ -0.3795T + 97.00 & \text{if } T_m \geq T > T_m - \Delta T \\ 2.092 \times 10^{-4}T + 0.5567 & \text{if } T > T_m \end{cases} \tag{A.7}$$

$$\mu_{pcm_{fit}}[mPas] = -0.0282T + 15.13 \quad \text{if } T > T_m \tag{A.8}$$

Table A.3: Thermodynamic properties of ENG as function of temperature [60].

T	cp **[**$kJ/kg^{\circ}C$**]**	ρ **[**kg/m^3**]**	α_T **[**$^{\circ}C^{-1}$**]**
0			
10			
20		831	3.00E-06
30	0.73		
40			
50	0.78		
60			
70	0.84		
80			
90			
100			
110	0.91		
120			
130	0.96		
140			
150	1.01		

$$cp_{capsule_{fit}}[J/kg^{\circ}C] = -0.0014T + 2.52 \tag{A.9}$$

$$\rho_{capsule}[kg/m^3] = \frac{\rho_0}{(1 - \alpha(T_0 - T))^3} \tag{A.10}$$

Table A.4: Heat capacity of ENG as function of density [60].

ρ_s $[kg/m^3]$	λ_{par} $[W/m°C]$	λ_{perp} $[W/m°C]$
30	2.1	
40	3.2	3
50	3.3	5
60	3.5	
70	4	
80	4.5	
90	4.8	
100	5.7	
110	5.9	15
120	6	
150	6.1	
170	7.3	
190	8	23
220	8.4	
250		48
290	8.5	
350	8.4	54
420	8.3	
450	8.3	
480		98
540		122
600	8.2	
650	8.5	
679		197
700	7	
754		247
800	6.5	
831		337
850	6.4	
900	6	
1000	5.3	
1100	5.5	
1180	5.3	
1250	5.3	

$$\lambda_{par_{fit}}[W/m°C] = 1.0 \times 10^{-3}\rho + 5.6 \tag{A.11}$$

$$\lambda_{perp_{fit}}[W/m°C] = 0.37\rho - 39.7 \tag{A.12}$$

$$\lambda_{capsule}[W/m°C] = \frac{\lambda_{par_{fit}} + \lambda_{perp_{fit}}}{2} \tag{A.13}$$

Table A.5: Thermodynamic properties of water as a function of temperature.

T **[**$^\circ C$**]**	ρ **[**kg/m^3**]**	μ **[**$mPas$**]**	cp **[**$kJ/kg^\circ C$**]**	λ **[**$W/m^\circ C$**]**
20	999	10015	0.602	4.182
40	993.05	6513	0.63	4.179
60	983.28	4630	0.653	4.185
80	971.82	3510	0.669	4.197
100	958.77	2790	0.68	4.216

$$cp_{water_{fit}}[J/kg^\circ C] = 1.667T + 4090 \tag{A.14}$$

$$\rho_{water_{fit}}[kg/m^3] = -0.751T + 1026 \tag{A.15}$$

$$\lambda_{water_{fit}}[W/m^\circ C] = 3.32 \times 10^{-4}T + 0.627 \tag{A.16}$$

$$\begin{aligned}\mu_{water_{fit}}[Pas] = -3.33 \times 10^{-10}T^3 + 1.49 \times 10^{-7}T^2 \\ -2.27 \times 10^{-5}T + 1.4 \times 10^{-3}\end{aligned} \tag{A.17}$$

B

Appendix

Extended discretization

An extended example of the influence of the BCs and an extended version of the TDMA for the PCS and PCM particle has been provided in this Appendix.

Governing equation of the PCS:

$$\frac{\theta^{n+1}(i,j)-\theta^{n}(i,j)}{\Delta Fo}+(1-\eta^2)\frac{\theta^{n}(i,j)-\theta^{n}(i,j-1)}{\Delta Z}+S^{n+1}(i,j)=\frac{1}{\eta}\frac{1}{\Delta\eta}\left(\Gamma\eta\left(\frac{\theta^{n+1}(i+1,j)-\theta^{n+1}(i,j)}{\Delta\eta}-\frac{\theta^{n+1}(i,j)-\theta^{n+1}(i-1,j)}{\Delta\eta}\right)\right) \tag{B.1}$$

BC of no heat transfer at center pipe:

$$\frac{\theta^{n+1}(i,j)-\theta^{n+1}(i-1,j)}{\Delta\eta}=0 \tag{B.2}$$

When implemented into the governing equation it becomes:

$$\frac{\theta^{n+1}(i,j)-\theta^{n}(i,j)}{\Delta Fo}+(1-\eta^2)\frac{\theta^{n}(i,j)-\theta^{n}(i,j-1)}{\Delta Z}+S^{n+1}(i,j)=\frac{1}{\eta}\frac{1}{\Delta\eta}\left(\Gamma\eta\left(\frac{\theta^{n+1}(i+1,j)-\theta^{n+1}(i,j)}{\Delta\eta}\right)\right) \tag{B.3}$$

BC of constant heat flux at the wall:

$$\frac{\theta^{n+1}(i+1,j)-\theta^{n+1}(i,j)}{\Delta\eta}=\frac{1}{\Gamma} \tag{B.4}$$

When implemented into the governing equation it becomes:

$$\frac{\theta^{n+1}(i,j)-\theta^{n}(i,j)}{\Delta Fo}+(1-\eta^2)\frac{\theta^{n}(i,j)-\theta^{n}(i,j-1)}{\Delta Z}+S^{n+1}(i,j)=\frac{1}{\eta}\frac{1}{\Delta\eta}\left(\Gamma\eta\left(-\frac{\theta^{n+1}(i,j)-\theta^{n+1}(i-1,j)}{\Delta\eta}\right)\right)+\frac{1}{\Delta\eta} \tag{B.5}$$

Governing equation of the PCM particle:

$$cp^{*^{n+1}}(k)(\theta_p(k)^{n+1}-\theta_p(k)^n)=\frac{\Delta Fo_p}{\Delta r^*}\left(\Lambda\left(\frac{\theta_p^{n+1}(k+1)-\theta_p^{n+1}(k)}{\Delta r^*}-\frac{\theta_p^{n+1}(k)-\theta_p^{n+1}(k-1)}{\Delta r^*}\right)\right) \tag{B.6}$$

BC of no heat transfer at center particle:

$$\frac{\theta_p^{n+1}(k)-\theta_p^{n+1}(k-1)}{\Delta r^*}=0 \tag{B.7}$$

When implemented into the governing equation it becomes:

$$cp^{*^{n+1}}(k)(\theta_p(k)^{n+1}-\theta_p(k)^n)=\frac{\Delta Fo_p}{\Delta r^*}\left(\Lambda\left(\frac{\theta_p^{n+1}(k+1)-\theta_p^{n+1}(k)}{\Delta r^*}\right)\right) \tag{B.8}$$

BC of heat transfer at the wall of the particle:

$$-\Lambda\frac{\theta_p^{n+1}(k+1)-\theta_p^{n+1}(k)}{\Delta r^*}=Nu_p(\theta_p^{n+1}(k)-\theta) \tag{B.9}$$

When implemented into the governing equation it becomes:

$$cp^{*^{n+1}}(k)(\theta_p(k)^{n+1}-\theta_p(k)^n)=\frac{\Delta Fo_p}{\Delta r^*}\left(\Lambda\left(-\frac{\theta_p^{n+1}(k)-\theta_p^{n+1}(k-1)}{\Delta r^*}\right)-Nu_p(\theta_p^{n+1}(k)-\theta)\right) \tag{B.10}$$

Figure B.1: Extendend tridiagonal matrix for the discretization of the governing equation of the PCS for a column j of i_{max} control volumes.

$$
\begin{bmatrix}
1+\Delta Fo(1,j)\Big(\frac{\Gamma(3/2,j)}{\Delta\eta(1)^2}+ 3\Phi_p\left(\frac{R_{HEX}}{R_p}\right)^2 Nu_p(1,j)\Big) & -\frac{\Gamma(3/2,j)\Delta Fo(1,j)}{\Delta\eta(1)^2} & 0 & 0 & \cdots & 0 \\
-\frac{\Gamma(3/2,j)\Delta Fo(2,j)}{\Delta\eta(2)^2} & 1+\Delta Fo(2,j)\Big(\frac{(\Gamma(3/2,j)+\Gamma(5/2,j))}{\Delta\eta(2)^2}+ 3\Phi_p\left(\frac{R_{HEX}}{R_p}\right)^2 Nu_p(2,j)\Big) & -\frac{\Gamma(5/2,j)\Delta Fo(2,j)}{\Delta\eta(2)^2} & 0 & \ddots & 0 \\
0 & -\frac{\Gamma\Delta Fo(3,j)}{\Delta\eta(3)^2} & 1+\Delta Fo(3,j)\Big(\frac{(\Gamma(5/2,j)+\Gamma(7/2,j))}{\Delta\eta(3)^2}+ 3\Phi_p\left(\frac{R_{HEX}}{R_p}\right)^2 Nu_p(3,j)\Big) & -\frac{\Gamma(7/2,j)\Delta Fo(3,j)}{\Delta\eta(3)^2} & \ddots & 0 \\
\vdots & \ddots & \ddots & \ddots & \ddots & \vdots \\
0 & 0 & 0 & 0 & -\Delta Fo(i_{max},j)\frac{\Gamma(i_{max}-1/2,j)}{\Delta\eta(i_{max},j)^2} & 1+\Delta Fo(i_{max},j)\Big(\frac{\Gamma(i_{max}-1/2,j)}{\Delta\eta(i_{max},j)^2}+ 3\Phi_p\left(\frac{R_{HEX}}{R_p}\right)^2 Nu_p(i_{max},j)\Big)
\end{bmatrix}
\begin{bmatrix}
\theta^{n+1}(1,j) \\
\theta^{n+1}(2,j) \\
\theta^{n+1}(3,j) \\
\vdots \\
\theta^{n+1}(i_{max},j)
\end{bmatrix}
=
$$

$$
\begin{bmatrix}
\theta^n(1,j)-\Delta Fo(1,j)(1-\eta(1))\frac{\theta^n(1,j)-\theta^n(1,j-1)}{\Delta Z(1,j})+3\Phi_p\left(\frac{R_{HEX}}{R_p}\right)^2 Nu_p(1,j)\Delta Fo(1,j)+\frac{\Delta Fo(1,j)}{\Delta\eta(1)} \\
\theta^n(2,j)-\Delta Fo(2,j)(1-\eta(2))\frac{\theta^n(2,j)-\theta^n(2,j-1)}{\Delta Z(1,j)}+3\Phi_p\left(\frac{R_{HEX}}{R_p}\right)^2 Nu_p(2,j)\Delta Fo(2,j) \\
\theta^n(3,j)-\Delta Fo(3,j)(1-\eta(1))\frac{\theta^n(3,j)-\theta^n(3,j-1)}{\Delta Z(3,j)}+3\Phi_p\left(\frac{R_{HEX}}{R_p}\right)^2 Nu_p(3,j)\Delta Fo(3,j) \\
\vdots \\
\theta^n(i_{max},j)-\Delta Fo(i_{max},j)(1-\eta(i_{max}))\frac{\theta^n(i_{max},j)-\theta^n(i_{max},j-1)}{\Delta Z(i_{max},j)}+3\Phi_p\left(\frac{R_{HEX}}{R_p}\right)^2 Nu_p(i_{max},j)\Delta Fo(i_{max},j)
\end{bmatrix}
$$

Figure B.2: Extendend tridiagonal matrix for the discretization of the governing equation of a PCM particle with k_{max} control volumes.

$$\begin{bmatrix} {cp^*}^{n+1}(1) + \frac{\Delta Fo_p(1)}{\Delta r^*(1)^2}\Lambda(3/2) & -\frac{\Delta Fo_p(1)}{\Delta r^*(1)^2}\Lambda(3/2) & 0 & 0 & \cdots & 0 \\ -\frac{\Delta Fo_p(2)}{\Delta r^*(2)^2}\Lambda(3/2) & \begin{gathered} {cp^*}^{n+1}(2) + \\ \frac{\Delta Fo_p(2)}{\Delta r^*(2)^2}(\Lambda(3/2)+\Lambda(5/2)) \end{gathered} & -\frac{\Delta Fo_p(2)}{\Delta r^*(2)^2}\Lambda(5/2) & 0 & \ddots & 0 \\ 0 & -\frac{\Delta Fo_p(3)}{\Delta r^*(3)^2}\Lambda(5/2) & \begin{gathered} {cp^*}^{n+1}(3) + \\ \frac{\Delta Fo_p}{\Delta {r^*}^2}(\Lambda(5/2)+\Lambda(7/2)) \end{gathered} & -\frac{\Delta Fo_p(3)}{\Delta r^*(3)^2}\Lambda(7/2) & \ddots & 0 \\ \vdots & \ddots & \ddots & \ddots & \ddots & \vdots \\ 0 & 0 & 0 & 0 & \cdots & \begin{gathered} {cp^*}^{n+1}(k_{max}) + \frac{\Delta Fo_p(k_{max})}{\Delta r^*(k_{max})^2}\Lambda(k_{max}-1/2) + \\ \frac{\Delta Fo_p(k_{max})}{\Delta r^*(k_{max})}Nu_p(i,j) \end{gathered} \end{bmatrix} \begin{bmatrix} \theta_p^{n+1}(1) \\ \theta_p^{n+1}(2) \\ \theta_p^{n+1}(3) \\ \vdots \\ \theta_p^{n+1}(k_{max}) \end{bmatrix} =$$

$$\begin{bmatrix} {cp^*}^n(1)\theta_p^n(1) \\ {cp^*}^n(2)\theta_p^n(3) \\ {cp^*}^n(2)\theta_p^n(3) \\ \cdots \\ {cp^*}^n(k_{max})\theta_p^n(k_{max}) + \frac{\Delta Fo_p(k_{max})}{\Delta r^*(k_{max})}Nu_p(i,j)\theta^n(i,j) \end{bmatrix}$$

Bibliography

[1] Mohammad Amani, Pouria Amani, Alibakhsh Kasaeian, Omid Mahian, and Wei-Mon Yan. Two-phase mixture model for nanofluid turbulent flow and heat transfer: Effect of heterogeneous distribution of nanoparticles. *Chemical Engineering Science*, 167:135–144, 2017. ISSN 0009-2509. doi: https://doi.org/10.1016/j.ces.2017.03.065. URL `http://www.sciencedirect.com/science/article/pii/S0009250917302555`.

[2] H. Benoit, L. Spreafico, D. Gauthier, and G. Flamant. Review of heat transfer fluids in tube-receivers used in concentrating solar thermal systems: Properties and heat transfer coefficients. *Renewable and Sustainable Energy Reviews*, 55:298–315, 2016. ISSN 1364-0321. doi: http://dx.doi.org/10.1016/j.rser.2015.10.059. URL `http://www.sciencedirect.com/science/article/pii/S1364032115011387`.

[3] C. Ernest Birchenall and Alan F. Riechman. Heat storage in eutectic alloys. *Metallurgical Transactions A*, 11(8):1415–1420, 1980. ISSN 1543-1940. doi: 10.1007/BF02653497. URL `http://dx.doi.org/10.1007/BF02653497`.

[4] J. Blumm, A. Lindemann, M. Meyer, and C. Strasser. Characterization of ptfe using advanced thermal analysis techniques. *International Journal of Thermophysics*, 31 (10):1919–1927, 2010. ISSN 1572-9567. doi: 10.1007/s10765-008-0512-z. URL `http://dx.doi.org/10.1007/s10765-008-0512-z`.

[5] P. Charunyakorn, S. Sengupta, and S. K. Roy. Forced convection heat transfer in microencapsulated phase change material slurries: flow in circular ducts. *International Journal of Heat and Mass Transfer*, 34(3):819–833, 1991. ISSN 0017-9310. doi: https://doi.org/10.1016/0017-9310(91)90128-2. URL `http://www.sciencedirect.com/science/article/pii/0017931091901282`.

[6] Lin Chen, Ting Wang, Yan Zhao, and Xin-Rong Zhang. Characterization of thermal and hydrodynamic properties for microencapsulated phase change slurry (mpcs). *Energy Conversion and Management*, 79:317–333, 2014. ISSN 0196-8904. doi: http://dx.doi.org/10.1016/j.enconman.2013.12.026. URL `http://www.sciencedirect.com/science/article/pii/S0196890413008029`.

[7] Kevin D. Cole and Barbaros Çetin. The effect of axial conduction on heat transfer in a liquid microchannel flow. *International Journal of Heat and Mass Transfer*, 54(11):2542–2549, 2011. ISSN 0017-9310. doi: https://doi.org/10.1016/j.ijheatmasstransfer.2011.02.007. URL `http://www.sciencedirect.com/science/article/pii/S0017931011000627`.

[8] F. Cverna and A.S.M.I.M.P.D. Committee. *ASM Ready Reference: Thermal properties of metals*. ASM International, 2002. ISBN 9780871707680. URL `https://books.google.nl/books?id=qvrq96gJFxIC`.

[9] Mónica Delgado, Ana Lázaro, Javier Mazo, and Belén Zalba. Review on phase change material emulsions and microencapsulated phase change material slurries: Materials,

heat transfer studies and applications. *Renewable and Sustainable Energy Reviews*, 16(1):253–273, 2012. ISSN 1364-0321. doi: http://dx.doi.org/10.1016/j.rser.2011.07.152. URL `http://www.sciencedirect.com/science/article/pii/S1364032111003996`.

[10] Yong Deng, Jinhong Li, Hongen Nian, Yali Li, and Xiaoping Yin. Design and preparation of shape-stabilized composite phase change material with high thermal reliability via encapsulating polyethylene glycol into flower-like tio2 nanostructure for thermal energy storage. *Applied Thermal Engineering*, 114:328–336, 2017. ISSN 1359-4311. doi: https://doi.org/10.1016/j.applthermaleng.2016.11.082. URL `http://www.sciencedirect.com/science/article/pii/S135943111633215X`.

[11] J. Douglas Jr. On the numerical integration of a parabolic differential equation subject to a moving boundary condition. *Duke Mathematical Journal*, 22(4):557, 1955. ISSN 1547-7398 0012-7094.

[12] DuPont Company. Teflon ptfe properties handbook. `http://www.rjchase.com/ptfe_handbook.pdf`. Online: Accessed April 5th, 2017.

[13] G M Dusinberre. Numerical methods for transient heat flow. *TRANSACTIONS OF THE A.S.M.S*, 67(8):703–12, 1945.

[14] Mari-Ann Einarsrud, Siv Haereid, and Volker Wittwer. Some thermal and optical properties of a new transparent silica xerogel material with low density. *Solar Energy Materials and Solar Cells*, 31(3):341–347, 1993. ISSN 0927-0248. doi: http://dx.doi.org/10.1016/0927-0248(93)90128-P. URL `http://www.sciencedirect.com/science/article/pii/092702489390128P`.

[15] Mehmet Esen, Aydin Durmuş, and Ayla Durmuş. Geometric design of solar-aided latent heat store depending on various parameters and phase change materials. *Solar Energy*, 62(1):19–28, 1998. ISSN 0038-092X. doi: http://dx.doi.org/10.1016/S0038-092X(97)00104-7. URL `http://www.sciencedirect.com/science/article/pii/S0038092X97001047`.

[16] N. R. Eyres, D. R. Hartree, J. Ingham, R. J. Sarjant, and J. B; Wagstaff. The calculation of variable heat flow in solids. *Philosophical Transactions of the Royal Society of London. Series A, Mathematical and Physical Sciences*, 240(813):1–57, 1946. doi: 10.1098/rsta.1946.0002. URL `http://rsta.royalsocietypublishing.org/content/roypta/240/813/1.full.pdf`.

[17] Zhihong Fan. *Latent Heat Thermal Storage*. Msc thesis, 2014.

[18] Jaume Gasia, Laia Miró, and Luisa F. Cabeza. Review on system and materials requirements for high temperature thermal energy storage. part 1: General requirements. *Renewable and Sustainable Energy Reviews*, 2016. ISSN 1364-0321. doi: http://dx.doi.org/10.1016/j.rser.2016.11.119. URL `http://www.sciencedirect.com/science/article/pii/S1364032116308772`.

[19] Haoshan Ge, Haiyan Li, Shengfu Mei, and Jing Liu. Low melting point liquid metal as a new class of phase change material: An emerging frontier in energy area. *Renewable and Sustainable Energy Reviews*, 21:331–346, 2013. ISSN 1364-0321. doi: http://dx.doi.org/10.1016/j.rser.2013.01.008. URL `http://www.sciencedirect.com/science/article/pii/S1364032113000324`.

[20] Antoni Gil, Marc Medrano, Ingrid Martorell, Ana Lázaro, Pablo Dolado, Belén Zalba, and Luisa F. Cabeza. State of the art on high temperature thermal energy storage for power generation. part 1—concepts, materials and modellization. *Renewable and Sustainable Energy Reviews*, 14(1):31–55, 2010. ISSN 1364-0321. doi: http://dx.doi.org/10.1016/j.rser.2009.07.035. URL `http://www.sciencedirect.com/science/article/pii/S1364032109001774`.

[21] Jessica Giro-Paloma, Mònica Martínez, Luisa F. Cabeza, and A. Inés Fernández. Types, methods, techniques, and applications for microencapsulated phase change materials (mpcm): A review. *Renewable and Sustainable Energy Reviews*, 53:1059–1075, 2016. ISSN 1364-0321. doi: http://dx.doi.org/10.1016/j.rser.2015.09.040. URL `http://www.sciencedirect.com/science/article/pii/S1364032115010102`.

[22] Manish Goel, S. K. Roy, and S. Sengupta. Laminar forced convection heat transfer in microcapsulated phase change material suspensions. *International Journal of Heat and Mass Transfer*, 37(4):593–604, 1994. ISSN 0017-9310. doi: https://doi.org/10.1016/0017-9310(94)90131-7. URL `http://www.sciencedirect.com/science/article/pii/0017931094901317`.

[23] Xiangtao Gong, Fuqiang Wang, Haiyan Wang, Jianyu Tan, Qingzhi Lai, and Huaizhi Han. Heat transfer enhancement analysis of tube receiver for parabolic trough solar collector with pin fin arrays inserting. *Solar Energy*, 144:185–202, 2017. ISSN 0038-092X. doi: http://dx.doi.org/10.1016/j.solener.2017.01.020. URL `http://www.sciencedirect.com/science/article/pii/S0038092X17300397`.

[24] D. J. Gunn. Transfer of heat or mass to particles in fixed and fluidised beds. *International Journal of Heat and Mass Transfer*, 21(4):467–476, 1978. ISSN 0017-9310. doi: https://doi.org/10.1016/0017-9310(78)90080-7. URL `http://www.sciencedirect.com/science/article/pii/0017931078900807`.

[25] R. S. Gupta and Dhirendra Kumar. Variable time step methods for one-dimensional stefan problem with mixed boundary condition. *International Journal of Heat and Mass Transfer*, 24(2):251–259, 1981. ISSN 0017-9310. doi: https://doi.org/10.1016/0017-9310(81)90033-8. URL `http://www.sciencedirect.com/science/article/pii/0017931081900338`.

[26] D.V. Hale, M.J. Hoover, and M.J. O'Neill. Phase change materials handbook. Report, NASA, 1971.

[27] HT Hashemi and CM Sliepcevich. A numerical method for solving two-dimensional problems of heat conduction with change of phase. In *Chem. Eng. Prog. Symp. Series*, volume 63, pages 34–41, 1967.

[28] G.J. Janz. *Physical properties data compilations relevant to energy storage II*. U.S. Dept of Commerce, National Bureau of Standards, 1977. URL `https://books.google.nl/books?id=EuQ9AQAAIAAJ`.

[29] G.J. Janz. *Physical Properties Data Compilations Relevant to Energy Storage...: Data on Additional Single and Multi-componant Salt Systems. Molten salts*. National Bureau of standards, 1981. URL `https://books.google.nl/books?id=ivNyMwEACAAJ`.

[30] Murat M. Kenisarin. High-temperature phase change materials for thermal energy storage. *Renewable and Sustainable Energy Reviews*, 14(3):955–970, 2010. ISSN 1364-0321. doi: http://dx.doi.org/10.1016/j.rser.2009.11.011. URL `http://www.sciencedirect.com/science/article/pii/S1364032109002731`.

[31] G. Kopp. *Earth's Incoming Energy: The Total Solar Irradiance*, pages 3–4. Elsevier, 2016. ISBN 978-0-12-409548-9. doi: http://dx.doi.org/10.1016/B978-0-12-409548-9.10366-5. URL `http://www.sciencedirect.com/science/article/pii/B9780124095489103665`.

[32] Mohamed Lachheb, Ali Adili, Fethi Albouchi, Foued Mzali, and Sassi Ben Nasrallah. Thermal properties improvement of lithium nitrate/graphite composite phase change materials. *Applied Thermal Engineering*, 102:922–931, 2016. ISSN 1359-4311. doi: http://dx.doi.org/10.1016/j.applthermaleng.2016.03.167. URL `http://www.sciencedirect.com/science/article/pii/S1359431116304756`.

[33] Anastas Lazaridis. A numerical solution of the multidimensional solidification (or melting) problem. *International Journal of Heat and Mass Transfer*, 13(9):1459–1477, 1970. ISSN 0017-9310. doi: https://doi.org/10.1016/0017-9310(70)90180-8. URL `http://www.sciencedirect.com/science/article/pii/0017931070901808`.

[34] F. Ma, P. Zhang, and X. J. Shi. Flow and heat transfer characteristics of micro-encapsulated phase change material slurry and energy transport evaluation. *Energy Procedia*, 105(Supplement C):4607–4614, 2017. ISSN 1876-6102. doi: https://doi.org/10.1016/j.egypro.2017.03.997. URL `http://www.sciencedirect.com/science/article/pii/S1876610217311128`.

[35] M. J. Maeso and J. Largo. The heat capacities of lino3 and csno3 from 350 to 700 k. *Thermochimica Acta*, 222(2):195–201, 1993. ISSN 0040-6031. doi: https://doi.org/10.1016/0040-6031(93)80552-L. URL `http://www.sciencedirect.com/science/article/pii/004060319380552L`.

[36] H. Mehling and L.F. Cabeza. *Heat and cold storage with PCM: An up to date introduction into basics and applications*. Springer Berlin Heidelberg, 2008. ISBN 9783540685579. URL `https://books.google.nl/books?id=N8LGwUNYWX8C`.

[37] Carlos I. Mendoza and I. Santamaría-Holek. The rheology of hard sphere suspensions at arbitrary volume fractions: An improved differential viscosity model. *The Journal of Chemical Physics*, 130(4):044904, 2009. doi: 10.1063/1.3063120. URL `https://aip.scitation.org/doi/abs/10.1063/1.3063120`.

[38] Yanio E. Milián, Andrea Gutiérrez, Mario Grágeda, and Svetlana Ushak. A review on encapsulation techniques for inorganic phase change materials and the influence on their thermophysical properties. *Renewable and Sustainable Energy Reviews*, 73:983–999, 2017. ISSN 1364-0321. doi: http://dx.doi.org/10.1016/j.rser.2017.01.159. URL `http://www.sciencedirect.com/science/article/pii/S1364032117301880`.

[39] Shamseldin A. Mohamed, Fahad A. Al-Sulaiman, Nasiru I. Ibrahim, Md Hasan Zahir, Amir Al-Ahmed, R. Saidur, B. S. Yılbaş, and A. Z. Sahin. A review on current status and challenges of inorganic phase change materials for thermal energy storage systems. *Renewable and Sustainable Energy Reviews*, 70:1072–1089, 2017. ISSN 1364-0321. doi: http://dx.doi.org/10.1016/j.rser.2016.12.012. URL `http://www.sciencedirect.com/science/article/pii/S1364032116310632`.

[40] W. D. Murray. Numerical and machine solutions of transient heat-conduction problems involving melting or freezing. *Journal of Heat Transfer*, 81:106, 1959. ISSN 0022-1481.

[41] Bibhuti Bhusan Nayak and Dipankar Chatterjee. Numerical investigation of convective heat transfer in pipeline flow of multi-sized mono dispersed fly ash-water slurry. *International Journal of Heat and Mass Transfer*, 108(Part B):1802–1818, 2017. ISSN 0017-9310. doi: https://doi.org/10.1016/j.ijheatmasstransfer.2017.01.057. URL `http://www.sciencedirect.com/science/article/pii/S0017931016315290`.

[42] S. D. Odeh, G. L. Morrison, and M. Behnia. Modelling of parabolic trough direct steam generation solar collectors. *Solar Energy*, 62(6):395–406, 1998. ISSN 0038-092X. doi: http://dx.doi.org/10.1016/S0038-092X(98)00031-0. URL `http://www.sciencedirect.com/science/article/pii/S0038092X98000310`.

[43] Stewart Paterson. Propagation of a boundary of fusion. *Proceedings of the Glasgow Mathematical Association*, 1(1):42–47, 1952. ISSN 2040-6185. doi: 10.1017/S2040618500032937. URL `https://www.cambridge.org/core/article/propagation-of-a-boundary-of-fusion/EB39E74281C6311CF90EE7C51B0A7513`.

[44] S. Pincemin, R. Olives, X. Py, and M. Christ. Highly conductive composites made of phase change materials and graphite for thermal storage. *Solar Energy Materials and Solar Cells*, 92(6):603–613, 2008. ISSN 0927-0248. doi: http://dx.doi.org/10.1016/j.solmat.2007.11.010. URL `http://www.sciencedirect.com/science/article/pii/S0927024807004291`.

[45] D. Poirier and M. Salcudean. On numerical methods used in mathematical modeling of phase change in liquid metals. *Journal of Heat Transfer*, 110(3):562–570, 1988. ISSN 0022-1481. doi: 10.1115/1.3250529. URL `http://dx.doi.org/10.1115/1.3250529`.

[46] Sylvain Quoilin, Martijn Van Den Broek, Sébastien Declaye, Pierre Dewallef, and Vincent Lemort. Techno-economic survey of organic rankine cycle (orc) systems. *Renewable and Sustainable Energy Reviews*, 22:168–186, 2013. ISSN 1364-0321. doi: http://dx.doi.org/10.1016/j.rser.2013.01.028. URL `http://www.sciencedirect.com/science/article/pii/S1364032113000592`.

[47] Sanjay K. Roy and Branko L. Avanic. Laminar forced convection heat transfer with phase change material suspensions. *International Communications in Heat and Mass Transfer*, 28(7):895–904, 2001. ISSN 0735-1933. doi: https://doi.org/10.1016/S0735-1933(01)00293-7. URL `http://www.sciencedirect.com/science/article/pii/S0735193301002937`.

[48] Ir R. Rutgers. Relative viscosity of suspensions of rigid spheres in newtonian liquids. *Rheologica Acta*, 2(3):202–210, 1962. ISSN 1435-1528. doi: 10.1007/BF01983952. URL `https://doi.org/10.1007/BF01983952`.

[49] A. Safari, R. Saidur, F. A. Sulaiman, Yan Xu, and Joe Dong. A review on supercooling of phase change materials in thermal energy storage systems. *Renewable and Sustainable Energy Reviews*, 70:905–919, 2017. ISSN 1364-0321. doi: http://dx.doi.org/10.1016/j.rser.2016.11.272. URL `http://www.sciencedirect.com/science/article/pii/S136403211631053X`.

[50] SaSol Germany Gmbh. Marlotherm sh product information. http://www.sasolgermany.de/fileadmin/images/marlotherm/MARLOTHERM_SH_info_e_.pdf. Online: Accessed April 3rd, 2017.

[51] G. SegrÉ and A. Silberberg. Radial particle displacements in poiseuille flow of suspensions. *Nature*, 189:209, 1961. doi: 10.1038/189209a0. URL http://dx.doi.org/10.1038/189209a0.

[52] Gianluca Serale, Francesco Goia, and Marco Perino. Numerical model and simulation of a solar thermal collector with slurry phase change material (pcm) as the heat transfer fluid. *Solar Energy*, 134:429–444, 2016. ISSN 0038-092X. doi: http://dx.doi.org/10.1016/j.solener.2016.04.030. URL http://www.sciencedirect.com/science/article/pii/S0038092X16300639.

[53] Atul Sharma, V. V. Tyagi, C. R. Chen, and D. Buddhi. Review on thermal energy storage with phase change materials and applications. *Renewable and Sustainable Energy Reviews*, 13(2):318–345, 2009. ISSN 1364-0321. doi: http://dx.doi.org/10.1016/j.rser.2007.10.005. URL http://www.sciencedirect.com/science/article/pii/S1364032107001402.

[54] Weiguang Su, Jo Darkwa, and Georgios Kokogiannakis. Review of solid–liquid phase change materials and their encapsulation technologies. *Renewable and Sustainable Energy Reviews*, 48:373–391, 2015. ISSN 1364-0321. doi: http://dx.doi.org/10.1016/j.rser.2015.04.044. URL http://www.sciencedirect.com/science/article/pii/S1364032115003147.

[55] Jian Sun and Wenhua Li. Operation optimization of an organic rankine cycle (orc) heat recovery power plant. *Applied Thermal Engineering*, 31(11–12):2032–2041, 2011. ISSN 1359-4311. doi: http://dx.doi.org/10.1016/j.applthermaleng.2011.03.012. URL http://www.sciencedirect.com/science/article/pii/S135943111100144X.

[56] Domingo Tarzia. *Relationship between Neumann solutions for two-phase Lame-Clapeyron-Stefan problems with convective and temperature boundary conditions*, volume 2015. 2014. doi: 10.2298/TSCI140607003T.

[57] W. S. J. Uijttewaal and R. V. A. Oliemans. Particle dispersion and deposition in direct numerical and large eddy simulations of vertical pipe flows. *Physics of Fluids*, 8(10):2590–2604, 1996. doi: 10.1063/1.869046. URL http://aip.scitation.org/doi/abs/10.1063/1.869046.

[58] K. Vignarooban, Xinhai Xu, A. Arvay, K. Hsu, and A. M. Kannan. Heat transfer fluids for concentrating solar power systems – a review. *Applied Energy*, 146:383–396, 2015. ISSN 0306-2619. doi: http://dx.doi.org/10.1016/j.apenergy.2015.01.125. URL http://www.sciencedirect.com/science/article/pii/S0306261915001634.

[59] N. Vitorino, J. C. C. Abrantes, and J. R. Frade. Numerical solutions for mixed controlled solidification of phase change materials. *International Journal of Heat and Mass Transfer*, 53(23–24):5335–5342, 2010. ISSN 0017-9310. doi: http://dx.doi.org/10.1016/j.ijheatmasstransfer.2010.07.023. URL http://www.sciencedirect.com/science/article/pii/S0017931010003923.

[60] L. W. Wang, S. J. Metcalf, R. E. Critoph, R. Thorpe, and Z. Tamainot-Telto. Thermal conductivity and permeability of consolidated expanded natural graphite treated with sulphuric acid. *Carbon*, 49(14):4812–4819, 2011. ISSN 0008-6223. doi: http://dx.doi.org/10.1016/j.carbon.2011.06.093. URL `http://www.sciencedirect.com/science/article/pii/S0008622311005422`.

[61] Ben Xu, Peiwen Li, and Cholik Chan. Application of phase change materials for thermal energy storage in concentrated solar thermal power plants: A review to recent developments. *Applied Energy*, 160:286–307, 2015. ISSN 0306-2619. doi: http://dx.doi.org/10.1016/j.apenergy.2015.09.016. URL `http://www.sciencedirect.com/science/article/pii/S0306261915010867`.

[62] M. Kamimoto Y. Takahashi, R. Sakamoto. Heat capacities and latent heats of lino3, nano3, and kno3. *International Journal of Thermophysics*, 9(6):1081–1090, 1988.

[63] Rui Yang, Hui Xu, and Yingping Zhang. Preparation, physical property and thermal physical property of phase change microcapsule slurry and phase change emulsion. *Solar Energy Materials and Solar Cells*, 80(4):405–416, 2003. ISSN 0927-0248. doi: http://dx.doi.org/10.1016/j.solmat.2003.08.005. URL `http://www.sciencedirect.com/science/article/pii/S0927024803001727`.